COMPUTATION OF HOLOGRAPHIC PATTERNS BETWEEN TILTED PLANES

A THESIS

SUBMITTED TO THE DEPARTMENT OF ELECTRICAL AND

ELECTRONICS ENGINEERING

AND THE INSTITUTE OF ENGINEERING AND SCIENCES

OF BILKENT UNIVERSITY

IN PARTIAL FULFILLMENT OF THE REQUIREMENTS

FOR THE DEGREE OF

MASTER OF SCIENCE

By

Gökhan Bora Esmer

June 2004

I certify that I have read this thesis and that in my opinion it is fully adequate, in scope and in quality, as a thesis for the degree of Master of Science.

Prof. Dr. Levent Onural(Supervisor)

I certify that I have read this thesis and that in my opinion it is fully adequate, in scope and in quality, as a thesis for the degree of Master of Science.

Prof. Dr. Haldun Özaktaş

I certify that I have read this thesis and that in my opinion it is fully adequate, in scope and in quality, as a thesis for the degree of Master of Science.

Prof. Dr. Atilla Aydınlı

Approved for the Institute of Engineering and Sciences:

Prof. Dr. Mehmet Baray
Director of Institute of Engineering and Sciences

ABSTRACT

COMPUTATION OF HOLOGRAPHIC PATTERNS BETWEEN TILTED PLANES

Gökhan Bora Esmer
M.S. in Electrical and Electronics Engineering
Supervisor: Prof. Dr. Levent Onural
June 2004

Holography is a three-dimensional visualization method. This method depends on duplication of information-carrying optical waves which come from a three-dimensional environment in the absence of the original source. Computation of the diffraction pattern due to an object is the most important process in digital holography. The diffraction pattern due to an object can be calculated by using several methods. Two models are generated and they are based directly on Rayleigh-Sommerfeld diffraction integral; there is no need for Fresnel or Fraunhofer approximations. The generated models are used to calculate scalar optical diffraction between tilted planes for monochromatic light. First model we generate is called pointwise model. The model provides calculation of the diffraction pattern on an observation plane by superposition of the diffraction patterns of the point light sources that made up the object on a input plane. However, it is a time consuming process. Second model is named plane wave spectrum model and it is much more faster than the pointwise model. The performances of the presented models are examined under several scenarios.

Keywords: Digital Holography, Plane Wave Spectrum Diffraction, Scalar Optical Diffraction, Fresnel Diffraction, 3-D Objects.

ÖZET

EĞİMLİ DÜZLEMLER ARASINDA HOLOGRAFİK DESEN HESAPLANMASI

Gökhan Bora Esmer
Elektrik ve Elektronik Mühendisliği Bölümü Yüksek Lisans
Tez Yöneticisi: Prof. Dr. Levent Onural
Haziran 2004

Holografi üç boyutlu bir görüntüleme metodudur. Bu metod, üç boyutlu çevreden gelen bilgi taşıyan optik dalgaların bir kopyasının orijinal kaynağın yokluğunda üretilmesine dayanır. Sayısal holografide en önemli süreç kırınım deseninin hesaplanmasıdır. Bir nesnenin kırınım saçağı farklı metodlar kullanılarak hesaplanabilir. İki metod kullanılmıştır ve bunlar doğrudan Rayleigh-Sommerfeld kırınım tümlevine dayandırılmıştır. Üretilen metodlar tek renkli ışık için eğimli düzlemler arasındaki skalar optik kırınımın hesabı için kullanılmaktadır. Üretiğimiz ilk metoda noktasal metod denilmiştir. Bu metod girdi düzlemindeki cismi oluşturan noktasal ışık kaynaklarının gözlem düzleminde oluşturduğu kırınım saçaklarının üstdüşümüyle hesaplanan kırınım saçağını sağlamaktadır. Ancak bu işlem zaman alan bir süreçtir. İkinci metod, düzlem dalga spektrumu modeli olarak adlandırılmıştır ve bu metod noktasal metoda göre çok daha hızlıdır. Sunulan metodların performansları farklı senaryolar altında incelenmiştir.

Anahtar kelimeler: Sayısal Holografi, Düzlem Dalga Spektrumu Kırınımı, Skalar Optik Kırınım, Fresnel Kırınımı, 3-B cisimler.

ACKNOWLEDGEMENTS

I gratefully thank my supervisor Prof.Dr. Levent Onural for his supervision, guidance, and suggestions throughout the development of this thesis.

I also would like to thank Prof. Dr. Haldun Özaktaş and Prof. Dr. Atilla Aydınlı for reading and commenting on the thesis.

Contents

List of Figures

To My Family . . .

Chapter 1

Introduction

Visual media have been used to express and communicate ideas for thousands of years. Recently, people worked on three-dimensional displays [1], [2], [3], [4], [6], [7]. These displays are investigated under two categories and these are stereoscopic and auto-stereoscopic displays [8]. Stereoscopic displays are based on the psychology of perception. While using the stereoscopic displays, we have to use viewing aids such as spectacles, because, we have to separate the views for left and right eyes. These views are taken from two different locations with a proper angle [10]. Nowadays, commercial three-dimensional motion pictures, which are based on stereoscopic display technique, are available such as IMAX 3D theaters. However, stereoscopic displays are not true three-dimensional displays. On the other hand, auto-stereoscopic displays provide various senses of depth about a scene. Moreover, auto-stereoscopic displays do not require special viewing aids. Some of auto-stereoscopic display techniques are lenticular, parallax barrier, slice stacking and holography [8]. Each of them provides different senses of depth to the human visual system. The quality of a three-dimensional display is determined by the sense of depth and resolution of the system.

Scientific and artistic applications of holography have been growing exponentially. Some of these are high resolution imaging of aerosols, multiple imaging, computer generated holograms, information storage, character recognition, holographic interferometry [16], [17] and holovideo [4], [20].

Calculation of the diffraction pattern due to a three-dimensional object is time consuming when the diffraction pattern of the object is obtained by summing up the diffraction pattern of each point light source which construct the object. The method uses point light sources to calculate the diffraction pattern of an object is named pointwise model. Constructing an object by point sources brings flexibility in the modelling of the object. For instance, the curvatures of the object can be represented smoothly. However, computational burden makes us search other methods to calculate the diffraction pattern of an object. Therefore, we construct an object by using planar patches as it is used in the computer graphics [19]. The planar patches represent the light distribution over the object. The light distribution of the object is obtained by using the Lambertian cosine law [19]. We present a method that gives the scalar optical diffraction between arbitrarily oriented planes. Also, the presented method provides fast computation for the diffraction pattern on the observation plane. Therefore, the diffraction pattern of an object can be calculated faster than the pointwise model.

Scalar optical diffraction between tilted planes has been investigated by several researchers. Ganci dealt with a specific problem in which the Fraunhofer approximation was used to diffract a plane wave tilted with respect to a plane containing a slit [24]. The tilted plane wave was diffracted onto another plane that was parallel to the slit plane by use of the Fraunhofer approximation. Then Patorski calculated the Fraunhofer intensity pattern of the tilted slit plane when it was diffracted onto a plane that was perpendicular to the initial plane wave propagation direction [25]. Rabal showed that the Fourier transform could be used to calculate the intensity pattern from a tilted plane onto another plane perpendicular to the initial beam propagation direction [26]. Leseberg and Frére are the first researchers who used Fresnel approximation to find the diffraction pattern of a tilted plane [27]. After that Frére and Leseberg suggested another method to approximate diffraction patterns of off-axis tilted objects [28]. Then Tommasi and Bianco found a technique for calculate the relation between the plane wave spectrum of the rotated planes [29]. They also used the proposed technique to calculate the computer generated holograms of off-axis objects [30]. Moreover, they applied the technique to model a space-variant optical interconnect [31]. Then, a method which is based on Rayleigh-Sommerfeld scalar diffraction integral is presented by Delen and Hooker. The method presented by Delen and Hooker provides full-scalar diffraction [32]. Matsushima, Schimmel and Wyrowski uses the same scalar diffraction method as Delen and Hooker but Matsushima, Schimmel and Wyrowski use several interpolation algorithms in their method [33].

In this thesis, we generalize the method which was presented by Delen and Hooker to compute the diffraction pattern between the input plane and the observation plane. The method presented by Delen and Hooker provides only the observation plane has tilt angle around x-axis and/or y-axis. The generalized method provides to have a tilt around x-axis and/or y-axis in both input and observation plane. Moreover, the observation plane can be placed at further distances. The method is also used to obtain the diffraction pattern of a three-dimensional object.

In this thesis, we present a modified technique of calculating scalar optical diffraction between input and observation plane. The modified technique provides fast calculation of the diffraction pattern on the observation plane and does not need Fresnel or Fraunhofer approximations. Furthermore, the calculation time of a hologram of an object which is constructed by planar patches is significantly shortened compared to the pointwise model when the presented technique is used. Thus, the presented technique could be useful to achieve three-dimensional holographic video.

1.1 Holography

Holography is one of the three-dimensional viewing techniques and it is the only technique that can satisfy all the depth cues [8]. These depth cues are accommodation, binocular disparity, motion parallax and occlusion. Accommodation is a oculomotor depth cue about focusing. Binocular disparity provides different views for both eyes. Motion parallax allows the viewer to move around the object scene, as is the case when viewing real scenes. Occlusion is about overlap and it is a pictorial depth cue.

Holography is based on the physics of optical waves and not on the psychology of perception as in the stereoscopic techniques [11]. Hologram is obtained by storing the diffraction pattern of a scene and photographic films can be used as a storing media. Then the information-carrying optical waves which came from the scene can be duplicated in the absence of the original optical waves. An important difference between holography and photography is in the information recording. In holography, the interference of the diffraction pattern of the scene and the reference beam is stored on the photographic film. In other words, the modulated version of the diffraction pattern is recorded on the photographic film. Also, coherent light is used in recording process of holography. However, in photography, only the magnitude information of the scene is stored on the film and non-coherent light can also be used in the recording process. Although holograms and photographs are two-dimensional(2-D) images, holograms provide three-dimensional(3-D) images and photographs contain only 2-D information of the scene.

The holography can be easily understood by the diffraction principles of optical waves and mathematics of the interference. However, there are several problems in the recording of the optical holograms. For instance, stability of the positions of the hologram and the object is absolutely essential in optical holography because the movement of the hologram or the object as small as a quarter wave-length of light during the exposure time can completely spoil the hologram. By using the digital holography most of problems in recording can be overcome.

1.2 History of Holography

Holography was invented in 1948 by a British (native of Hungary) scientist Dennis Gabor. He introduced the theory of holography while he was working to improve the resolution of an electron microscope [15]. The term hologram is coined by D. Gabor from the Greek words "holos" and "gramma". The word holos means whole and gramma indicate the message. Because of not having truly coherent light sources, there had not been any further development in the holography during the next decade [18].

In 1960, N. Bassov, A. Prokhorov and C. Townes invented the laser. Therefore having coherent light source was ideal for making holograms [18]. In 1962, E. Leith and J. Upatnieks developed the off-axis holography technique. In the same year, Y. N. Denisyuk produced holograms that could be viewed by using white light. In 1965, a model of computer generated hologram(CGH) was presented by B. R. Brown and A. W. Lohmann [18]. In 1989, MIT Media Laboratory Spatial Group designed and built a holographic video system [5], [8]. That system could work in real-time [5]. However, the information content was reduced by elimination of the vertical parallax, reduction of resolution and reduction of the image size and the horizontal viewing zone [8].

The organization of this thesis is as follows. The next chapter provides the optical and mathematical model for off-axis holography. The theory of scalar diffraction is also given in that chapter. In chapter 3, the pointwise simulator is presented and its input specification, hologram generation and reconstruction processes are given. In chapter 4, the plane wave spectrum simulator is presented. As in Chapter 3 the input specification, hologram generation and reconstruction processes are explained in detail. Also in Chapter 4 the simulation results are given in subsection 4.4 of the chapter. Subsection 4.5 provides the discussion about the simulation results. In chapter 5 comparison between the two simulators under several scenarios is given. Chapter 6 provides some conclusions about the performances of the simulators and future work.

Chapter 2

Off-axis Holography

Holography uses the physical phenomena of interference and diffraction to record on a photographic film and to reconstruct a three-dimensional image. A laser beam is split into the object beam, which illuminates the object, and the reference beam which illuminates the recording medium directly. The magnitude of the superposition of the object beam **O** and the reference beam **R** are recorded on a photosensitive film and it is called the hologram. The interference of two beams provides the medium to store both the magnitude and phase of the incident object field. The recording medium have to be sensitive to at least 1500 linepairs/millimeter, to record the fringes properly [8].

An illustration of a typical off-axis holographic set up is given in Figure 2.1. Diffraction through the object, which is represented by $O(x, y)$, interferes with a reference beam $R(x, y)$. The reference beam is taken as a plane wave whose amplitude is R_0 and it is incident upon the recording medium with its direction of propagation in the x-z plane. An illustration of the reference beam is given in Figure 2.1. The mathematical expression of $R(x, y)$ is

$$R(x, y) = R_0 e^{jkx \sin\theta} e^{jkz} \tag{2.1}$$

where k is the wave number, θ is the angle shown in Figure 2.1. Because of dealing

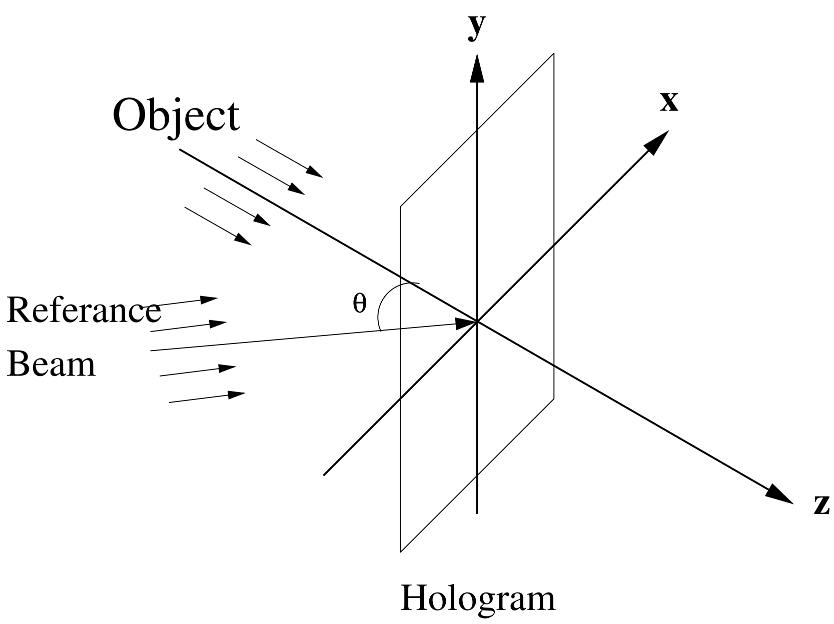

Figure 2.1: Generation of off-axis hologram

with scalar optical diffraction the polarization of the fields are omitted. Moreover, all wavefronts are assumed to be mutually coherent sources of monochromatic light. Furthermore, the square magnitude of the field equals to optical intensity. The time-harmonic field incident on the hologram is written as

$$\psi(x, y) = O(x, y) + R(x, y) \quad . \tag{2.2}$$

The stored fringe pattern on the hologram is represented as

$$I(x, y) = \left|O(x, y) + R(x, y)\right|^2 \quad . \tag{2.3}$$

The expansion of Eq. 2.3 is shown as

$$I(x, y) = \left|O(x, y)\right|^2 + \left|R(x, y)\right|^2 + O(x, y)R(x, y)^* + R(x, y)O(x, y)^* \tag{2.4}$$

where * represents complex conjugate. The term $\left|O(x, y)\right|^2$ is called object self-interference and it is a spatially varying pattern. The object self-interference causes distortion in the reconstruction process. One of the methods that is used to solve this problem is the separation of the object self-interference from the object beam in the spatial domain. To obtain the separation, we have to increase the incidence angle of the reference beam to at least three times the angle

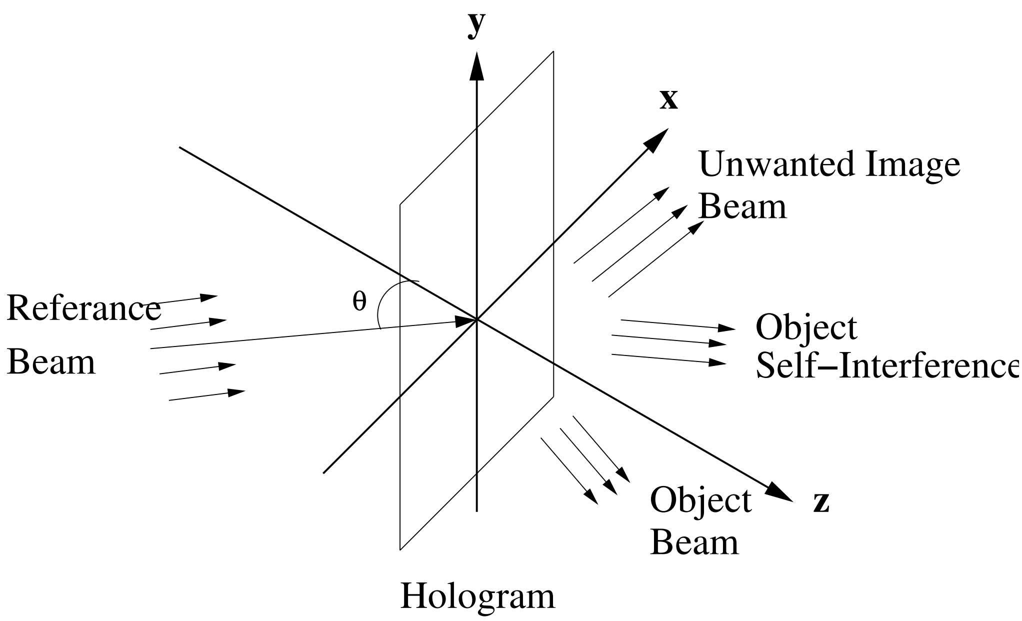

Figure 2.2: Reconstruction process of off-axis hologram

subtended by the object beam, because the object self-interference occupies two times larger bandwidth compared to the object beam. Unfortunately, increasing the reference beam angle is expensive in computational holography. The signal $\left|R(x,y)\right|$ is called the reference bias and it represents a spatially invariant (DC) that increases the magnitude of the intensity on the hologram. The components $O(x,y)R(x,y)^*$ and $R(x,y)O(x,y)^*$ are the interference between the object wavefront and the reference beam. These signals contain all of the holographic information that is necessary for the object reconstruction.

Illumination of the hologram by the reference beam reconstructs the recorded three-dimensional object. The pattern that is obtained by the illumination diffracts and makes the object visible as it is physically present and tangible. The reconstruction process is illustrated in Figure 2.2. The diffraction from the illuminated hologram is given as

$$\begin{aligned}
\psi_{rec}(x,y) &= \big[R(x,y)I(x,y)\big] **h(x,y) \\
&= R(x,y)\big|R(x,y)\big|^2 **h(x,y) \\
&\quad +R(x,y)\big|O(x,y)\big|^2 **h(x,y) \\
&\quad +\big|R(x,y)\big|^2 O(x,y) **h(x,y) \\
&\quad +R(x,y)^2 O(x,y)^* **h(x,y)
\end{aligned} \tag{2.5}$$

where $h(x, y)$ is the impulse response of the system which represents optical diffraction. The function $**$ represents the two-dimensional convolution. The first term in Eq 2.5 is the uniform beam of light which propagates straight through the hologram. The second term is the undesired cross term artifact. The third term is the desired reconstruction of the object. The fourth term is the diffraction field of the object at a different distance with a spatially shift in x-direction.

Some researchers record only the field in their simulations (in a digital environment). However in optical holography, there is no way to store only the field [9] but by using some computational techniques we can obtain the holographic fringes. These computational techniques are called computational holography [8]. Computational holography begins with a three-dimensional numerical description of the object or scene to be reproduced. Then the diffraction pattern due to the object scene on the hologram plane is calculated. The calculated diffraction pattern and the reference beam are added to obtain the interfered signal. The intensity of the interfered signal is stored on a holographic display. The display is illuminated by a reference beam and spatially modulates the reference beam according to the stored fringe pattern to achieve the reconstruction process in optical holography.

Computational holography has two bottlenecks in computation speed according to [8]. One of them is caused by having enormous number of samples to represent microscopic features. The other one is the computational complexity of the simulation of the light diffraction and obtaining the interference pattern. Therefore, several techniques are used to reduce information content. For instance, elimination of vertical parallax brings great reduction in the information content. Moreover, the reduction in the size of the object or the viewing zone brings some additional advantages in managing the information content. By using the technique presented in this thesis, we can simulate the light propagation without having a reduction in the vertical parallax of the object. Moreover, the presented technique provides fast computation.

The analysis of the scalar optical diffraction starts from Maxwell's equations [21]. Moreover, the dielectric medium, which is used in the analysis, is assumed to be linear, homogeneous and non-dispersive. By applying the properties of the dielectric medium to the Maxwell's equations, we can represent the behavior of the electric and magnetic fields by a single scalar wave equation as

$$\nabla^2 u - \frac{n^2}{c^2}\frac{\partial^2 u}{\partial t^2} = 0 \tag{2.6}$$

where ∇^2 is the Laplacian operator, n represents the refrective index and c is the vacuum velocity of light [21]. The term $u(P,t)$ is a real function and represents the optical wave. By applying necessary boundary conditions and simplifications which can be found in literature [21], [22], we obtain the phasor representation of $u(P,t)$ as

$$U(P_0) = \int\int_{\Sigma} h(P_0,P_1)U(P_1)ds \tag{2.7}$$

where $U(P_1)$ is the excitation at the corresponding point. We can obtain $u(P,t)$ from its phasor representation as

$$u(P,t) = Re\big\{U(P)e^{-j2\pi vt}\big\} \quad . \tag{2.8}$$

The parameter $h(P_0,P_1)$ is the impulse response and given as

$$h(P_0,P_1) = \frac{1}{j\lambda}\frac{e^{jkr_{01}}}{r_{01}}\cos\theta \tag{2.9}$$

where θ is the angle between the normal vector of the aperture and $\vec{r_{01}}$ which is the vector joining the observation point and an abstract source in aperture.

In this thesis, two hologram simulators are designed and implemented. First one is the pointwise simulator and the second one is plane wave spectrum simulator. Moreover, neither one of the simulators needs Fresnel or Fraunhofer approximations. The pointwise simulator is easy to model, but it takes too long a computational time to get the results. Plane wave spectrum simulator provides much shorter calculation time of the diffraction pattern than the pointwise simulator. However, the model used in the plane wave spectrum simulator is mathematically more complicated than the model used in the pointwise simulator.

Chapter 3

Pointwise Simulator

3.1 Introduction

In this chapter, mathematical model of the pointwise simulator is presented. The model is based on the Rayleigh-Sommerfeld diffraction integral. Therefore there is no need to have Fresnel or Fraunhofer approximations. This chapter includes the relation between discrete and continuous theory of the scalar optical diffraction. Then the pointwise simulator based on the discrete theory is presented. The simulator has two parts. First part of the simulator is used to generate the off-axis hologram of a given object. Second part of the simulator provides the reconstruction process of the given hologram. Both parts of the simulator can be fed by synthetically generated input data.

The reason of having pointwise simulator is to calculate the diffraction pattern of the object correctly. Also the generation of the pointwise simulator is easy. Moreover, we have got a tool which will be useful to check the degree of correctness of other simulators.

3.2 Off-axis Hologram Calculation

Off-axis hologram of a given object is obtained by the summation of the diffraction field of the object and the reference beam propagating the different angular direction from the object waves. The mathematical representation of the diffraction field due to an object is expressed in the Eq. 2.7. However, we want to calculate the diffraction field of the object in a digital environment. Therefore, a discrete model of the scalar optical diffraction is generated. In this model, the object is represented by using impulse functions. The mathematical representation of an object is given as

$$f(x,y) = \sum_{n,m} a(n,m)\delta(x - nX, y - mX) \tag{3.1}$$

where the parameter X is the spatial sampling period and as it is seen in the above equation spatial sampling period is same in both x-axis and y-axis. The variables n and m are integers in the range $[\frac{-N}{2}, \frac{N}{2})$. When the Eq. 3.1 is substituted into Eq. 2.7, the diffraction field is obtained as

$$O(x',y') = \int\int h(x,y,x',y')\Big\{\sum_{n,m} a(n,m)\delta(x - nX, y - mX)\Big\}dxdy \tag{3.2}$$

where the variables x' and y' represent the location of P_1 and x and y are the variables determine the location of P_0. The Eq. 3.2 can be rewritten as

$$O(x',y') = \sum_{n,m} h(nX, mX, x', y')a(n,m) \tag{3.3}$$

We use arrays to display the diffraction field of the object. Therefore, the sampled version of $O(x',y')$ is used in the discrete model of the scalar optical diffraction and it is represented as

$$O(x',y') = \sum_{n',m'} O_D(n',m')\delta(x' - n'X, y' - m'X) \tag{3.4}$$

where the variable $O_D(n',m')$ is the samples of the $O(x',y')$. The Eq. 3.4 can be written as

$$O(x',y') = \sum_{n',m'}\sum_{n,m} h(nX, mX, n'X, m'X)a(n,m)\delta(x' - n'X, y' - m'X) \tag{3.5}$$

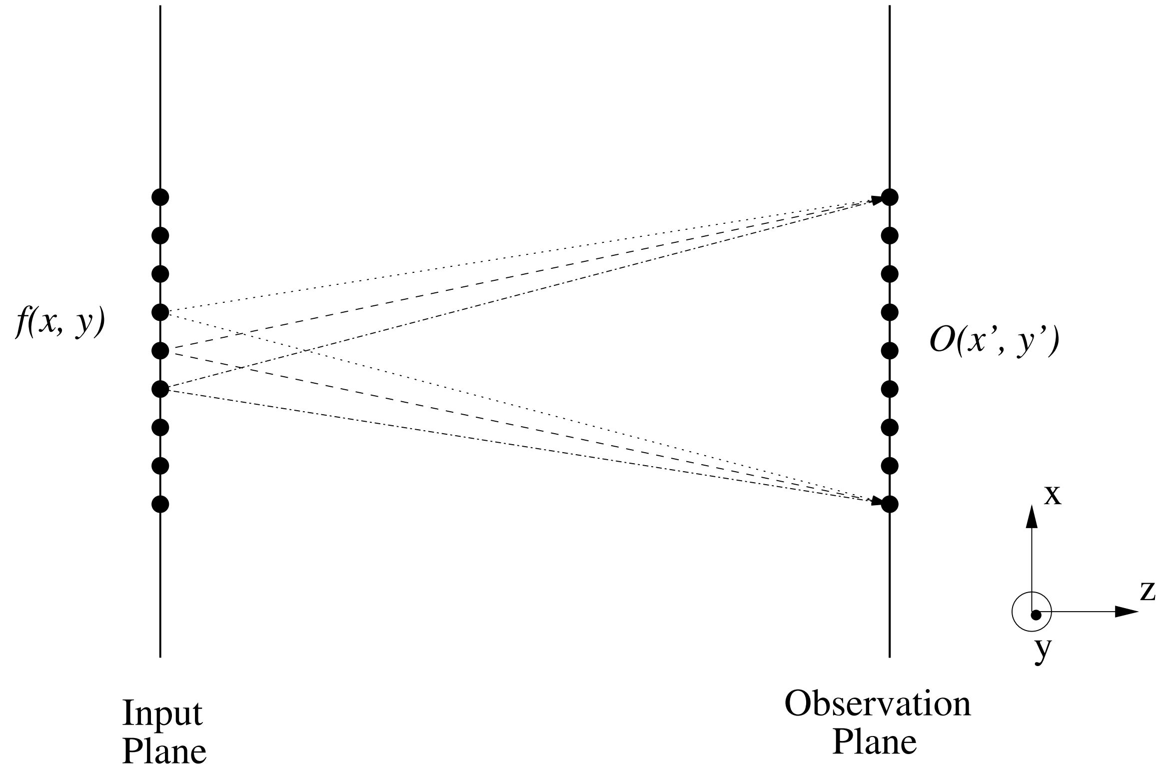

Figure 3.1: The illustration of the discrete scalar diffraction model

There is a two-dimensional illustration of the discrete model in Figure 3.1. The given object is represented by its samples in Figure 3.1. The sampling points are shown by circles. The same representation is done for the diffraction field on observation plane in Figure 3.1. There are some restrictions in the generated diffraction model. One of the restrictions is the generated diffraction model which provides the sampled diffraction field of the sampled object. Another restriction is caused by the variable $h(nX, mX, n'X, m'X)$, because in discrete domain it is calculated in a window. There is an illustration of the window in Figure 3.2. Therefore, there is a low-pass operation on the variable $h(nX, mX, n'X, m'X)$.

To obtain the diffraction field of the given object, we have to compute the impulse response function $h(nX, mX, n'X, m'X)$. In continuous domain the impulse response can be represented as

$$h(P_0, P_1) = h(x, y, z) = \frac{1}{j\lambda} \frac{e^{j\frac{2\pi}{\lambda}\sqrt{x^2+y^2+z^2}}}{\sqrt{x^2+y^2+z^2}} \cos\theta \tag{3.6}$$

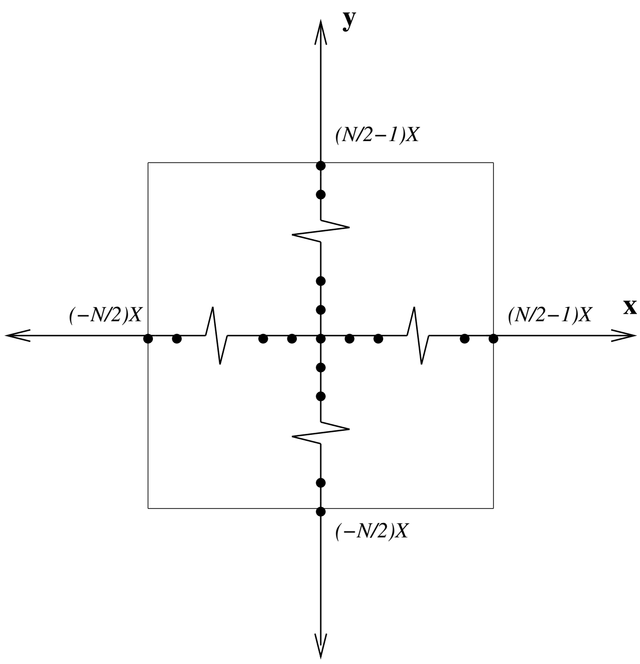

Figure 3.2: Illustration of the window

when P_0 is taken as $(0, 0, 0)$. The term $h(x, y, z)$ is the kernel of the pointwise model. It can be seen from Eq. 3.6 that the characteristic of the impulse response function is similar to a chirp function. Properties of the chirp function are given in [22]. Detailed information about sampling of a chirp signal can be found in literature [14], [23] and [34]. The discrete kernel of the pointwise model is obtained as

$$x = nX, \quad y = mX, \quad z = pX \tag{3.7}$$

where the variable p does not need to be an integer. Then by substituting the variables in Eq. 3.7 to Eq. 3.6, the kernel is rewritten as

$$h(nX, mX, pX) = \frac{1}{j\lambda X\sqrt{n^2 + m^2 + p^2}} e^{j\frac{2\pi}{\lambda}X\sqrt{n^2+m^2+p^2}} \frac{p}{\sqrt{n^2 + m^2 + p^2}} \tag{3.8}$$

By normalizing the above equation we get the discrete kernel as

$$h_{a,b}[n, m] = \frac{1}{jH\sqrt{n^2 + m^2 + b}} e^{ja\sqrt{n^2+m^2+b}} \frac{\sqrt{b}}{\sqrt{n^2 + m^2 + b}} \tag{3.9}$$

where a equals to $\frac{2\pi}{\lambda}X$ and the variable b is p^2. Moreover the variable H is related to the magnitude of the kernel and equals to λX.

The mathematical expression of the sampled reference beam is obtained as

$$R(n,m) = R_0 e^{j\Gamma n} \tag{3.10}$$

where Γ is defined as $a \sin\theta$.

The parameters needed to obtain discrete reference beam and discrete impulse response are N, p, X, Γ and R_0. In the pointwise simulator the parameters depend on the wavelength. Therefore assigning a value to the wavelength changes all the corresponding physical parameters. The variable z_0 is chosen according to the chosen wavelength to get diffraction pattern on the observation plane at the desired location and it determines the variable p. The simulator gets the variable N which is determined previously by the user. The variable Γ in Eq. 3.10 determines the incidence angle of the reference beam. However, the variable Γ has to be assigned to a value between $-\pi$ and π, because the reference beam is circulant according to its incidence angle and it can be seen in Eq. 2.1 and Eq. 3.10. For instance we obtain the same reference beam when we assign the parameter Γ to 0.3 or 6.58. Also, assigning Γ to -0.3 or 5.98 provides the same reference beam. The parameter R_0 has to be large to suppress the cross-term effect.

The diffraction due to an object is simulated by the pointwise simulator. The mathematical relation between the given object and the diffraction pattern can be expressed as

$$O_D(n',m') = \sum_{n,m=\frac{-N}{2}}^{\frac{N}{2}-1} a(n,m,z(n,m))h_{a,b(n,m)}(n',m') \tag{3.11}$$

where $O_D(n',m')$ is the discrete form of the variable $O(x,y)$ in Eq. 2.2. The parameter $a(n,m,z(n,m))$ is the given object. The term $z(n,m)$ represents the z-axis location of each point light source that makes up the object. Also the variable $b(n,m)$ gives the distance between hologram plane and the points on the object. As it can be seen from Eq. 3.11, the optical system is linear but

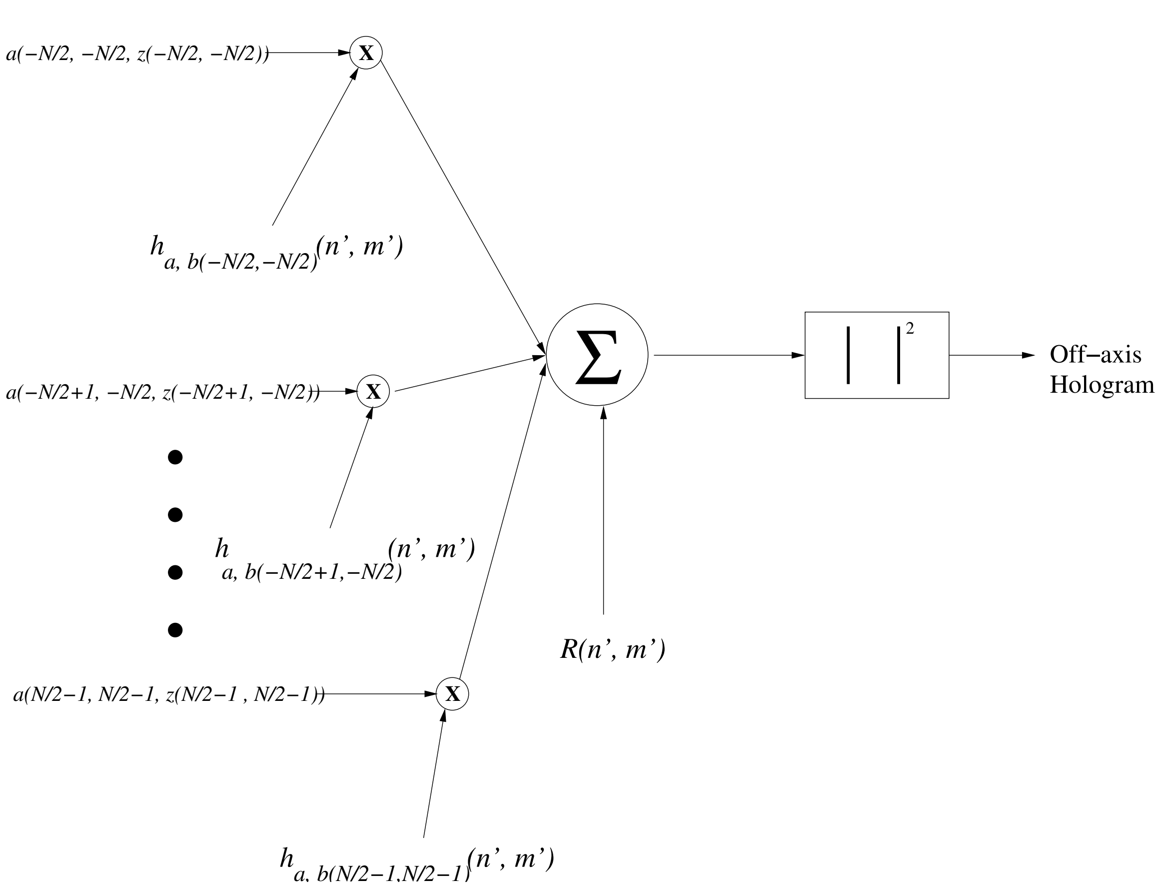

Figure 3.3: Discrete Computation of Off-axis Hologram

not shift-invariant on z-axis. It is linear because Eq. 3.11 satisfies the linearity properties. However, the variation on the variable $b(n, m)$ causes to have different discrete kernels for the each point sources. Therefore the diffraction field of the object is computed by summing up the diffraction field of all the point sources. After then the reference beam is added to the diffraction field of the object. Finally, the magnitude of the obtained field gives us the off-axis hologram of the object. The block diagram of the system corresponding to hologram recording is shown in Figure 3.3

The program expects proper input variables. For instance, the variable N which determines the size of the filter, is an integer. However, the variable p is a real variable and stored by using double precision. Moreover, the input object has to be supplied to the simulator as a union of point sources. There is a popular format for the description of an object in computer graphics uses vertices and faces [19] and it is used to obtain the input object. Therefore, another program is written to convert from popular formats to the special input format of off-axis hologram generator program. The details of the input generation program is given in appendix A.

The hologram generation program needs two arrays. They are provided as files. The properties of the files and the details of the hologram generation program are given in Appendix D. First array gives the surface illumination variation of the object. Second array provides the variable N.

The hologram generation program provides two output arrays. One of them is used to display the off-axis hologram of the given object. The other is a data array of which elements is determined by double precision and gives the off-axis hologram.

3.3 Reconstruction Process

In the reconstruction process, the calculated hologram is illuminated by the same reference beam used in the off-axis hologram generation process to get the object at its original place. Then the obtained field is diffracted backwards. Similar diffraction model as in the previous section is used in the computation of diffraction. Backward diffraction is obtained by replacing the negative wave number in the impulse response given in Eq. 3.9. Therefore, the impulse response of the system becomes

$$h_{a,b,B}[n,m] = \begin{cases} \frac{1}{jH\sqrt{n^2+m^2+b}} e^{-ja\sqrt{n^2+m^2+b}} \frac{\sqrt{b}}{\sqrt{n^2+m^2+b}}, \text{if } \ |n|,|m| \leq \frac{N-1}{2} \\ 0 \qquad\qquad\qquad\qquad , \text{elsewhere} \end{cases} \tag{3.12}$$

where the parameters a and b are the same as in the forward diffraction process. The block diagram of the reconstruction process is given in Figure 3.5.

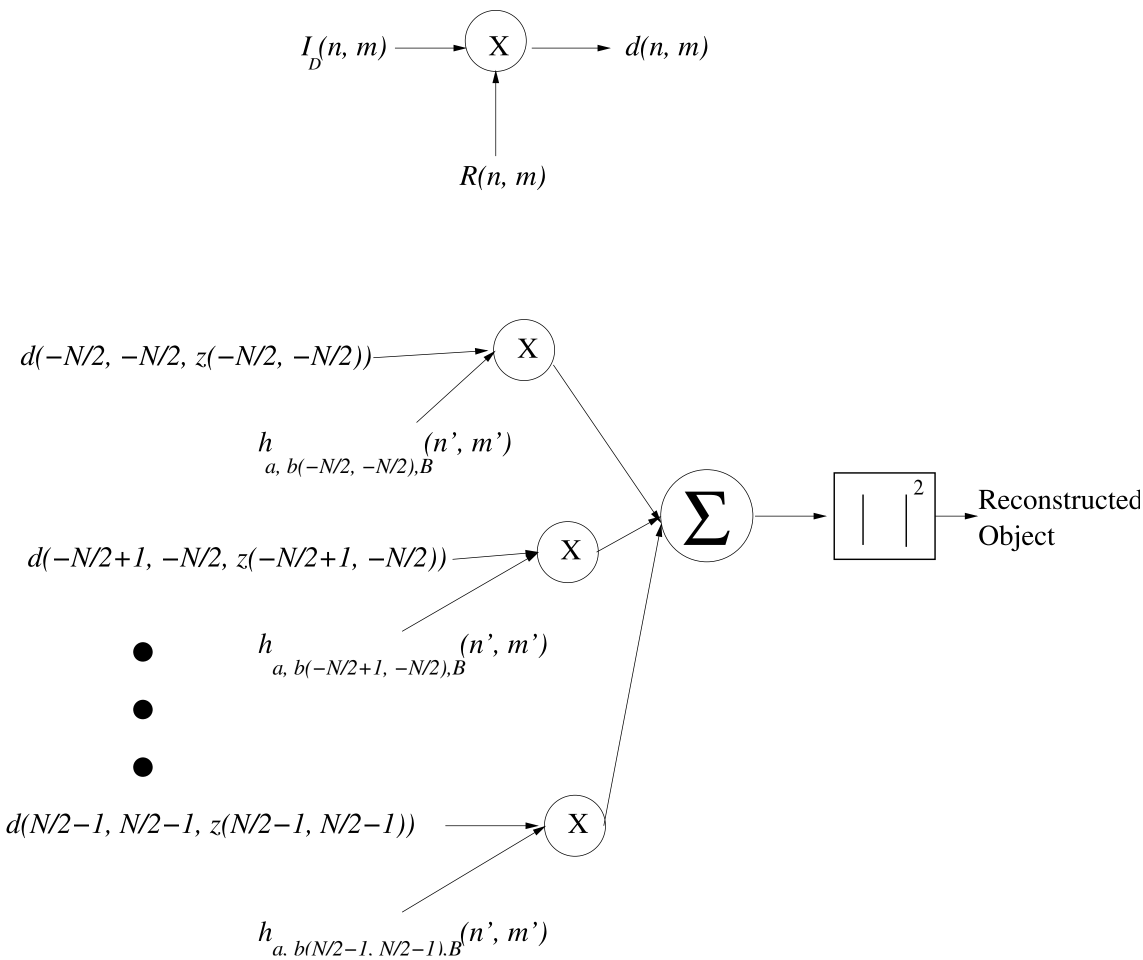

Figure 3.4: Discrete computation of the reconstruction process

The parameters R_0, Γ, N, X, and p have to be supplied to the program by the user. The details of the object reconstruction program is given in Appendix D. Reassignment of the parameters brings flexibility in the generated simulator.

There is only one output array in the object reconstruction program and it displays the reconstructed object.

3.4 Simulation Results

In the simulations, the variable N is taken as 512. Therefore the dimensions of the impulse response is restricted to 512x512. To reduce the calculation error, precisions of the variables are chosen as 8 bytes (double precision due to the machine used for simulations). Simulation results are displayed on the screen and stored in a file in raw image format. The gray level variations are quantized to 256 levels. Level 0 represents the darkest region and level 255 gives the brightest region. Three-dimensional object in Figure 3.12 is converted to two-dimensional while displaying on the screen by using orthographic projection. In the simulations the variables λ, X and z are taken as 633nm, $2N\lambda$ and $4N^3\lambda$. Moreover the parameters of reference beam, R_0 and Γ, are taken as 200 and 0.8 in order to decrease the effect of the cross term in Eq 2.4. In the reconstruction process the DC component is subtracted to decrease the effect of the uniform beam of light propagating through the hologram.

In the first simulation, we examine the obtained results of scalar optical diffraction of a simple object. The object, which is represented by $a(n, m)$, is shown in Figure 3.5. By using simple objects we can easily comment on the obtained diffraction field. Figure 3.6 represents the real part of the diffraction field and 3.7 is the cross-section of the real part of the diffraction field which is taken from the center of it. Figure 3.8 gives the magnitude of the diffraction pattern and Figure 3.9 provides the cross-section taken from the center. Figure

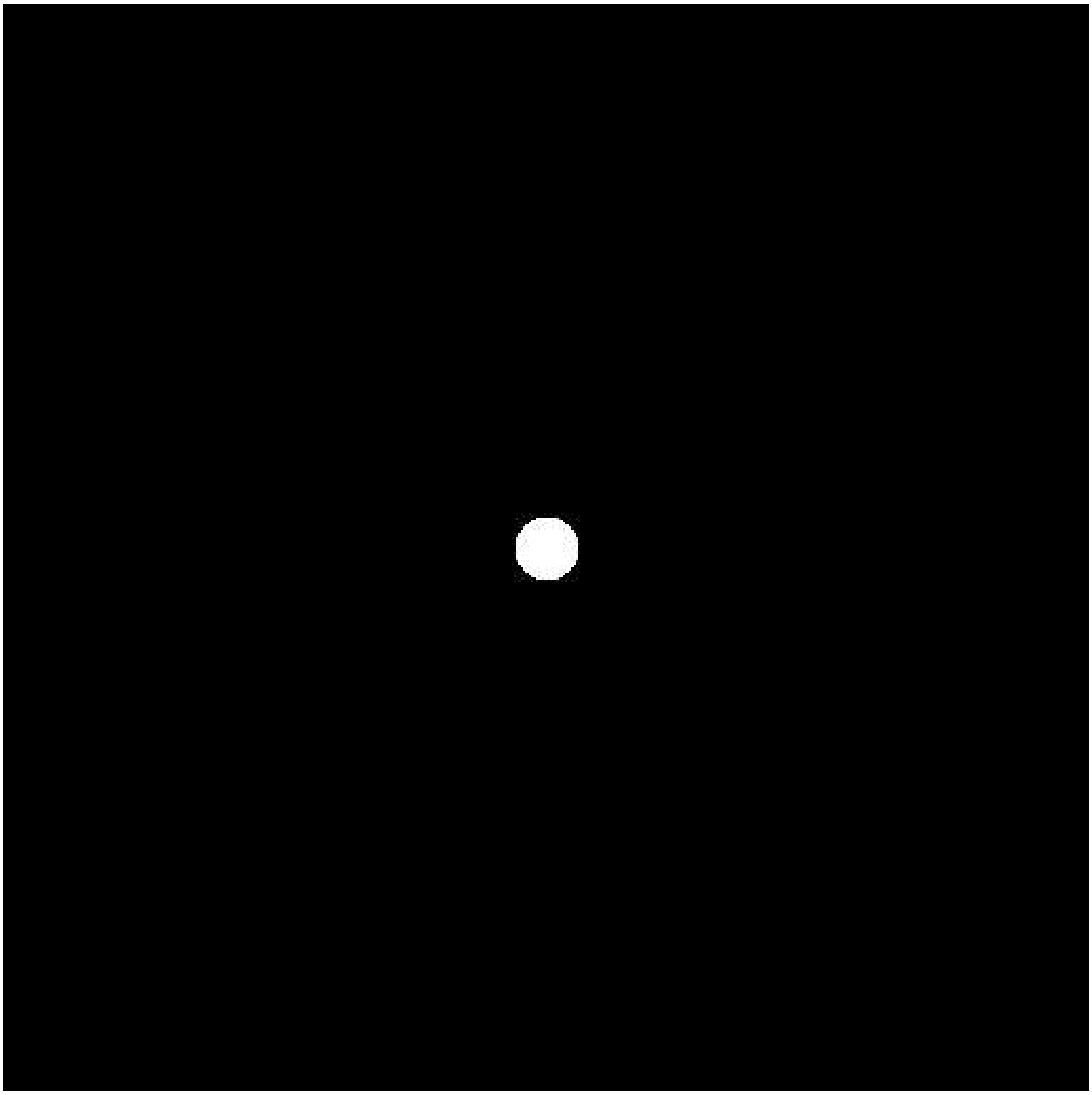

Figure 3.5: An input object

3.10 represents the off-axis hologram of the object $a(n,m)$and Figure 3.11 gives the reconstructed object. Because of the twin-image, the reconstructed object is a little bit distorted. The distortion causes variation on the light distribution of the reconstructed object and it can be seen in the Figure 3.11.

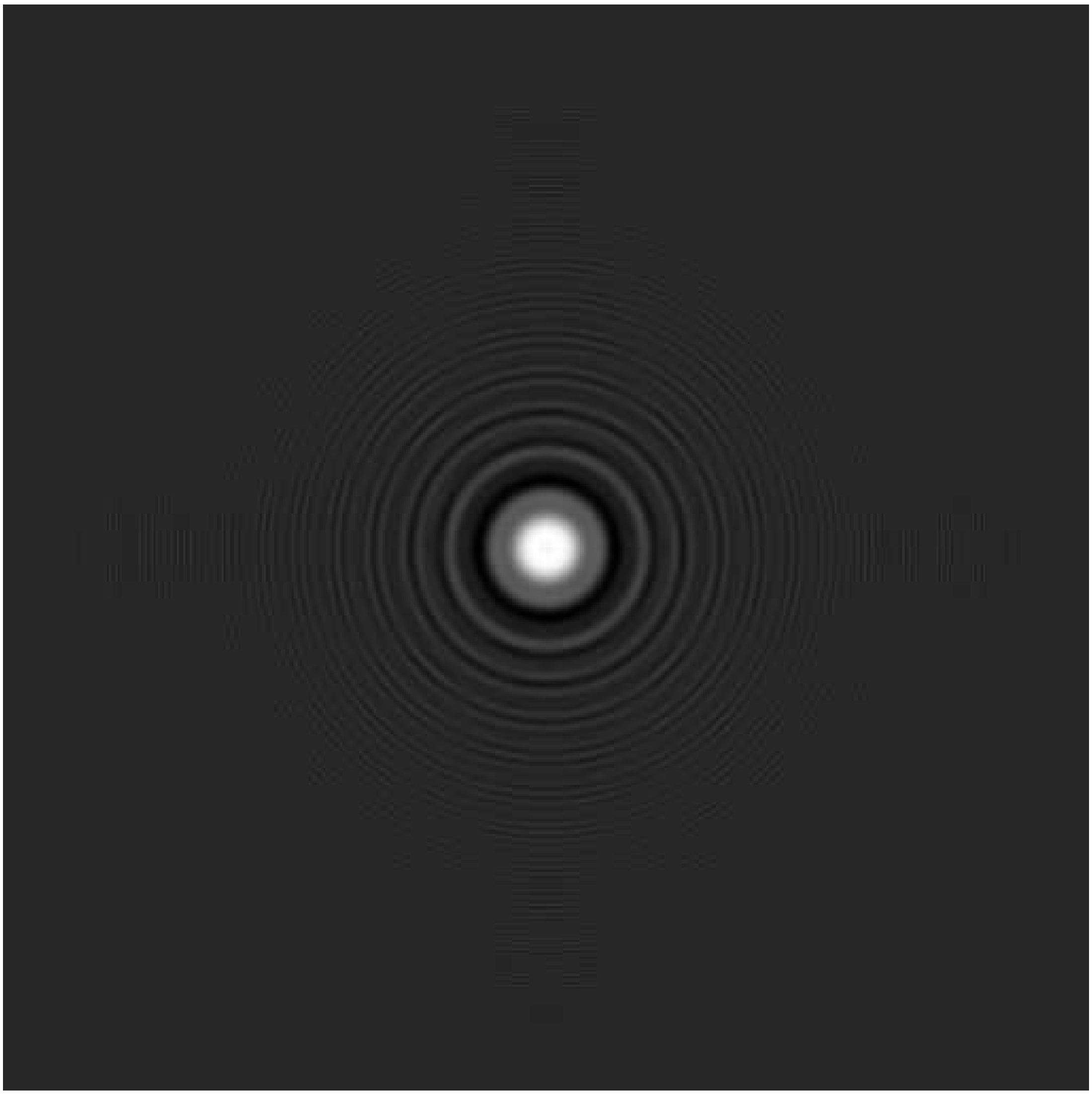

Figure 3.6: Real part of the diffraction pattern corresponding to the input shown in Figure 3.5

Figure 3.12 is an input for another simulation. It can be seen that there are two small square objects, but they are located on different positions of z-axis. The square of which is on top with respect to the other, is located closer to the hologram plane. The Figure 3.12 represents the orthographic projection of the squares. In orthographic projection, we display only x-axis and y-axis components of the object. Figure 3.13 gives the off-axis hologram of the input. In Figure 3.14 we can see the reconstructed image of the distant square and Figure 3.15 gives the reconstructed image of closer square. Moreover, Figures

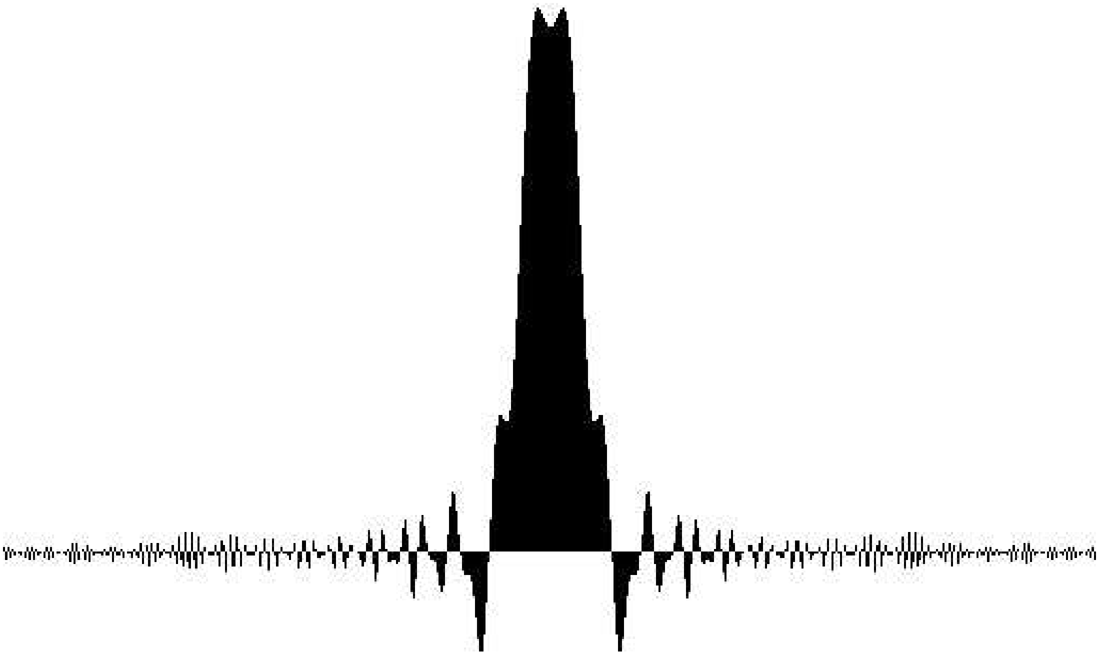

Figure 3.7: Cross-section at the center of real part of the diffraction pattern shown in Figure 3.6

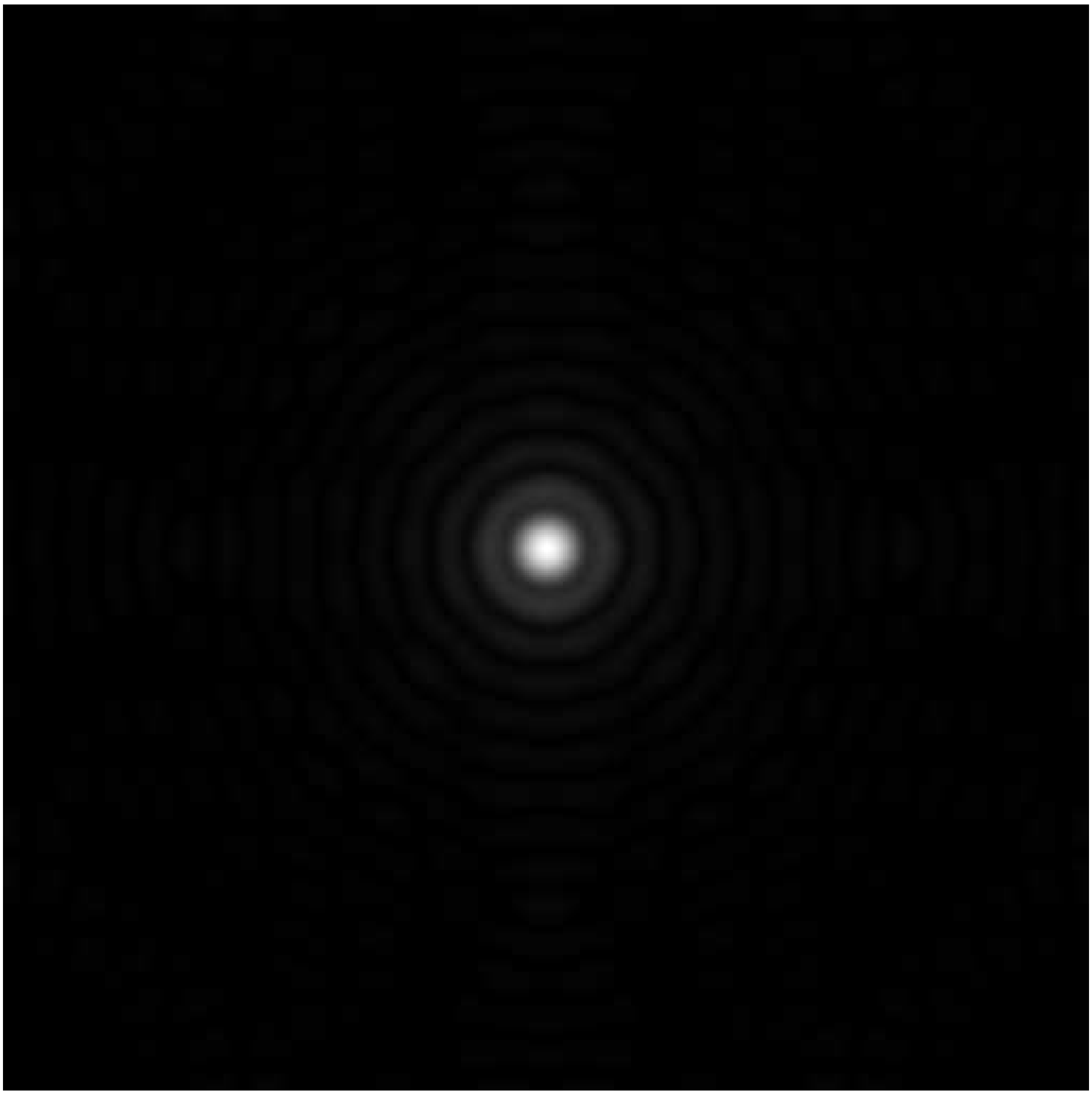

Figure 3.8: Magnitude of the diffraction pattern corresponding to the input shown in Figure 3.5

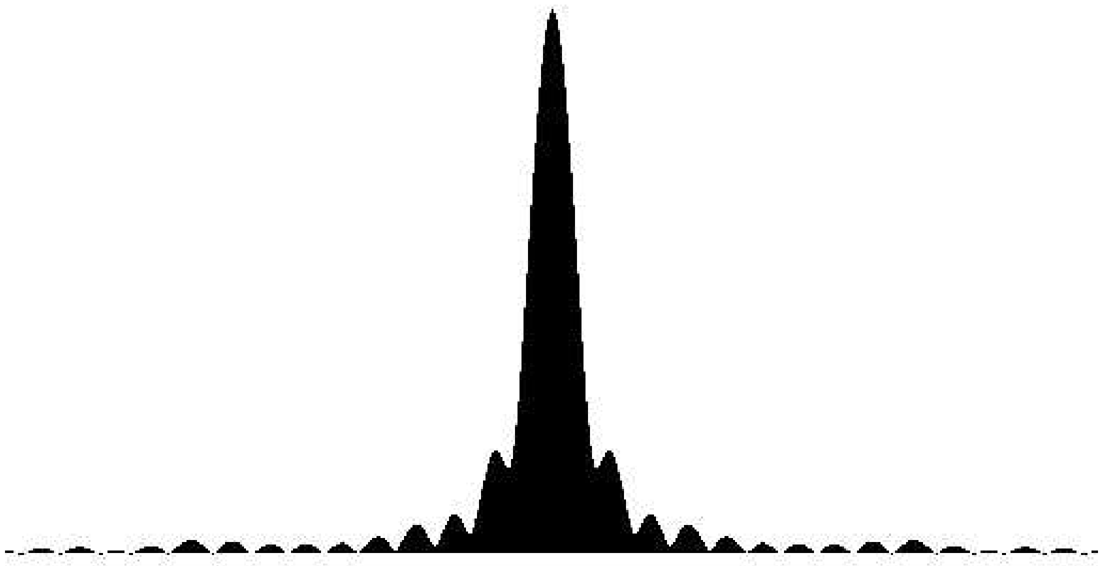

Figure 3.9: Cross-section at the center of magnitude of the diffraction pattern shown in Figure 3.8

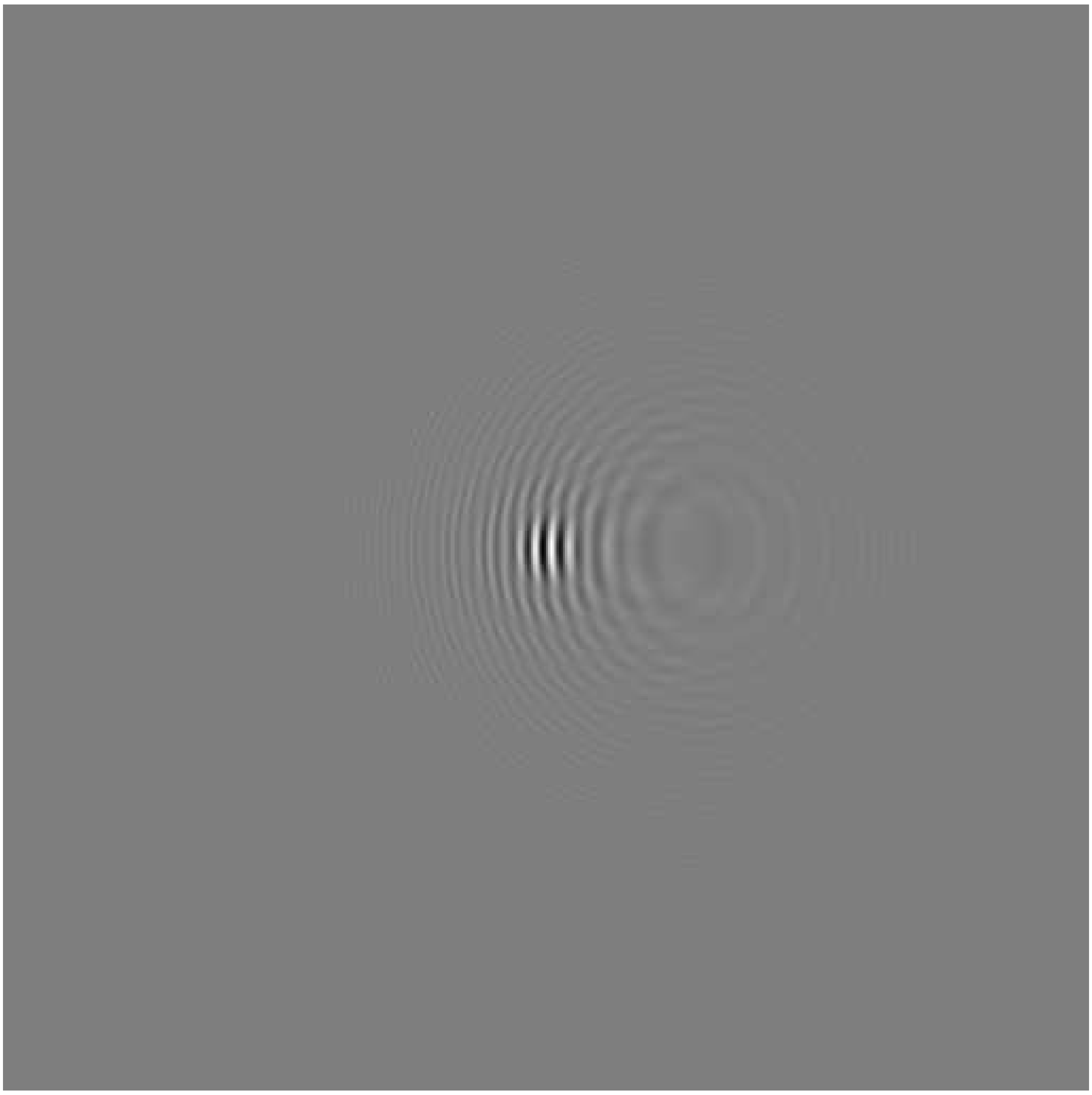

Figure 3.10: Off-axis hologram of the object shown in Figure 3.5

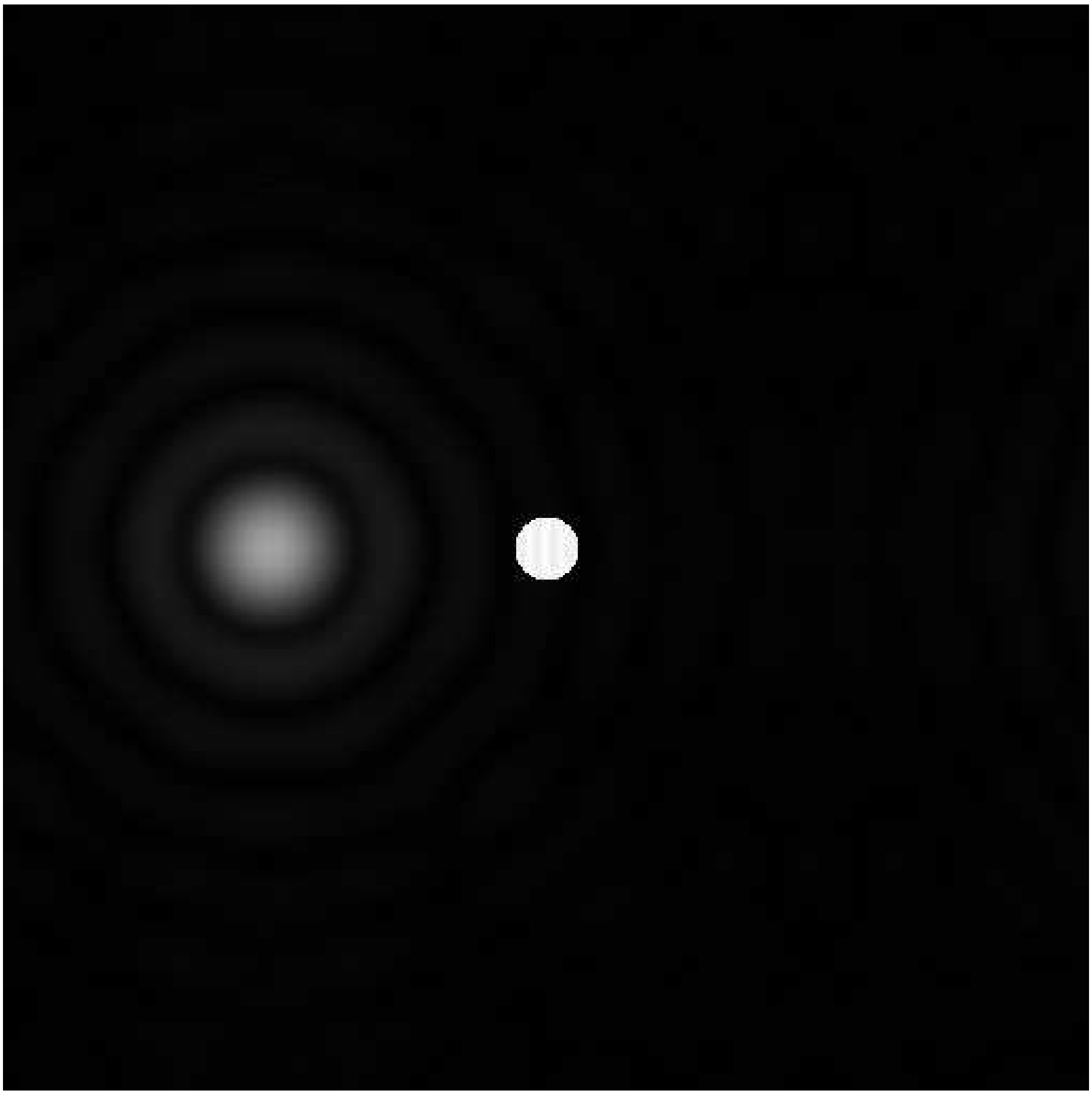

Figure 3.11: Magnitude of the reconstructed object from off-axis hologram shown in Figure 3.10

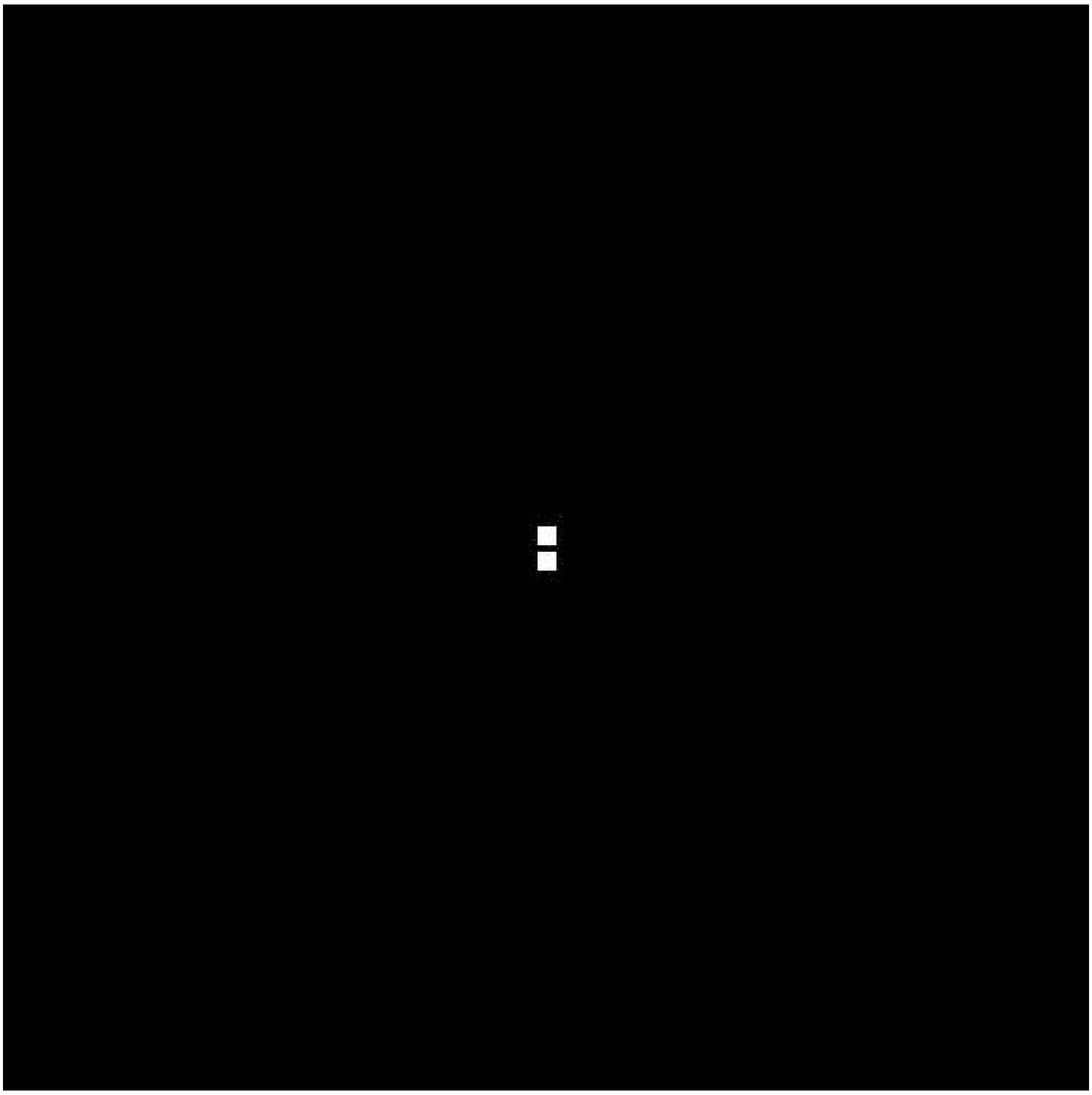

Figure 3.12: Orthographic projection of an input object. The square on top with respect to the other one is located closer to the hologram plane.

3.15 and 3.14 represent how two objects which are located at different positions on z-axis, can interact the diffraction patterns of each other.

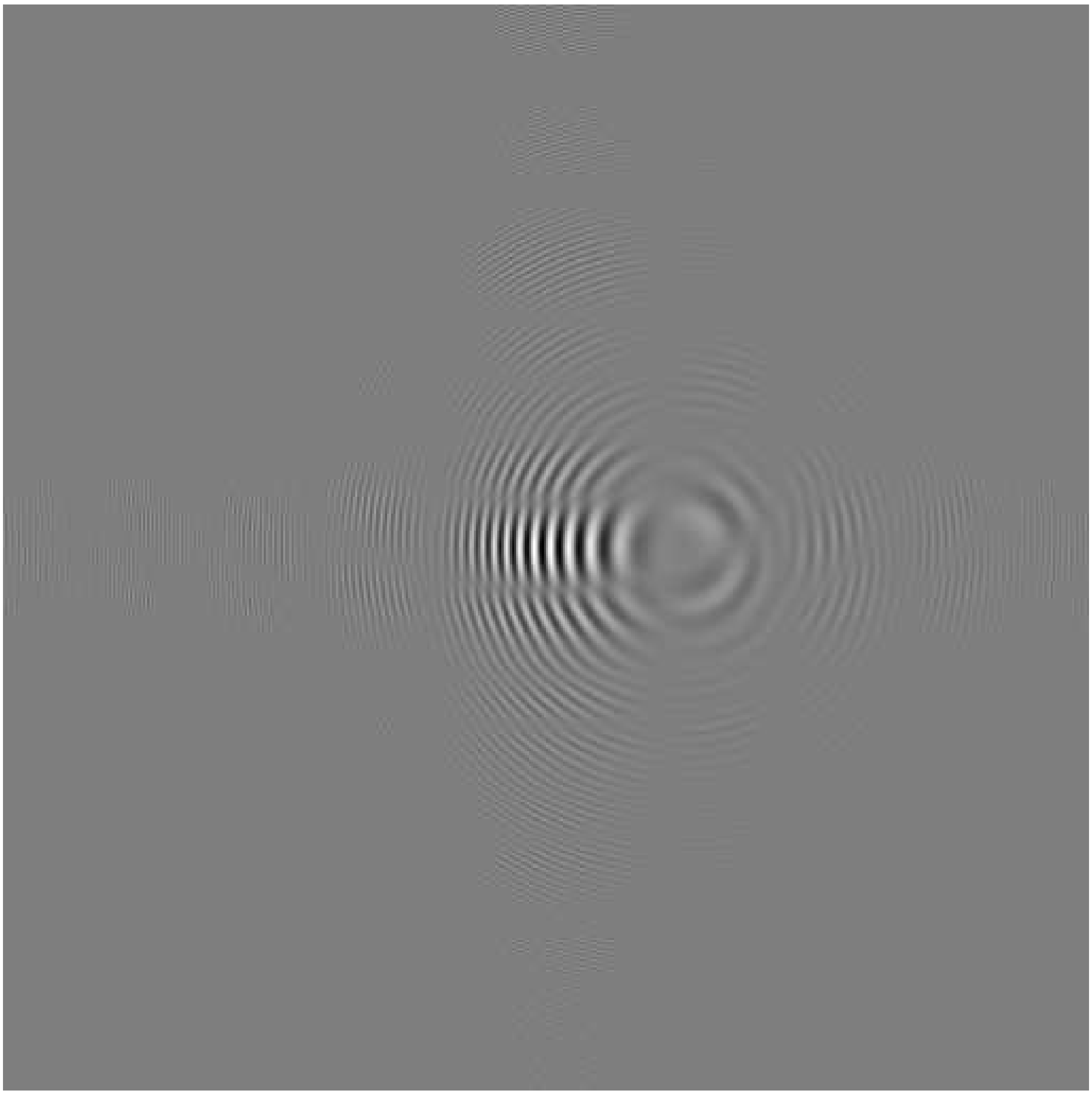

Figure 3.13: Off-axis hologram of the object in Figure 3.12

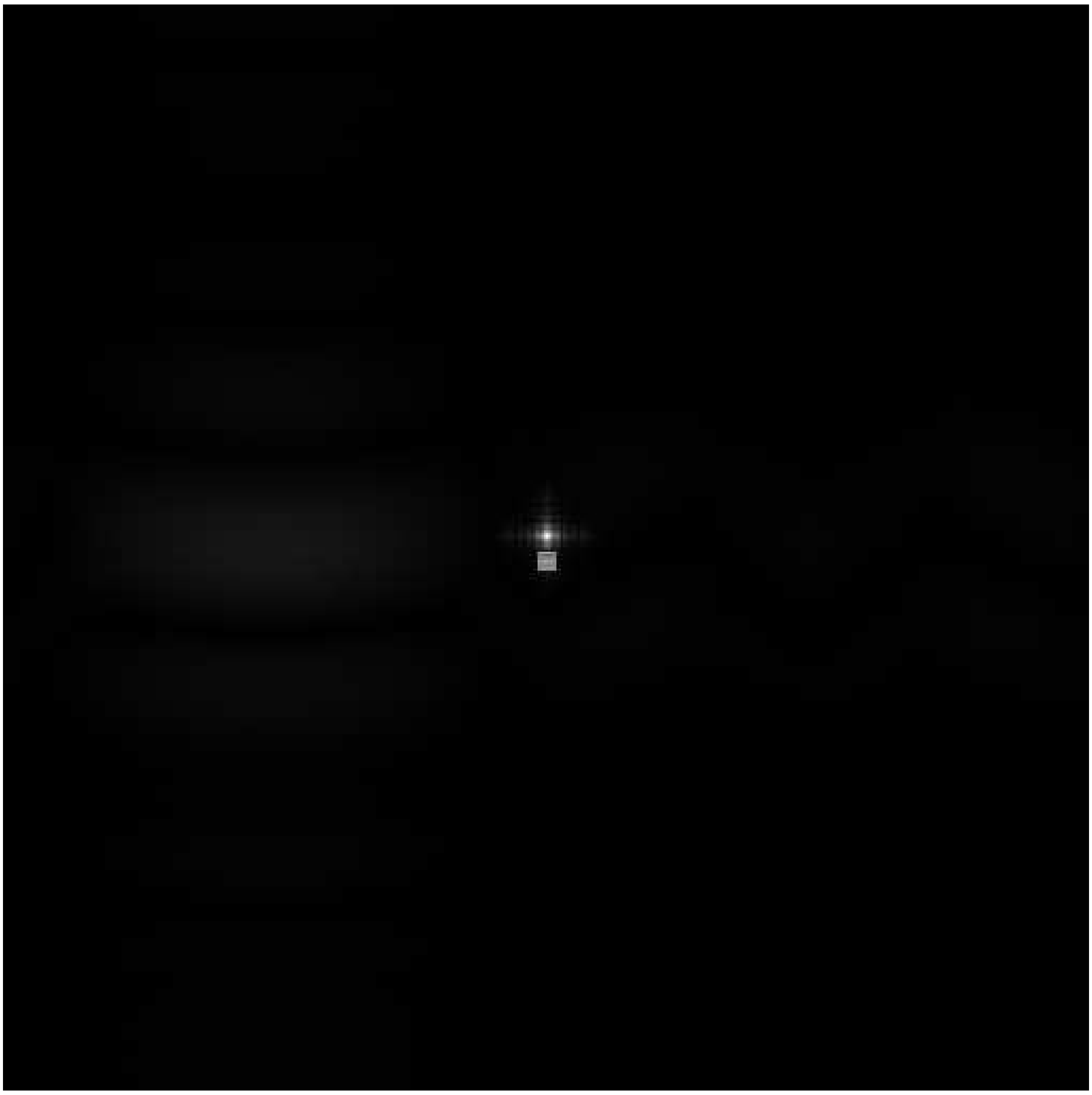

Figure 3.14: Magnitude of a reconstructed object from the off-axis hologram shown in Figure 3.13

32

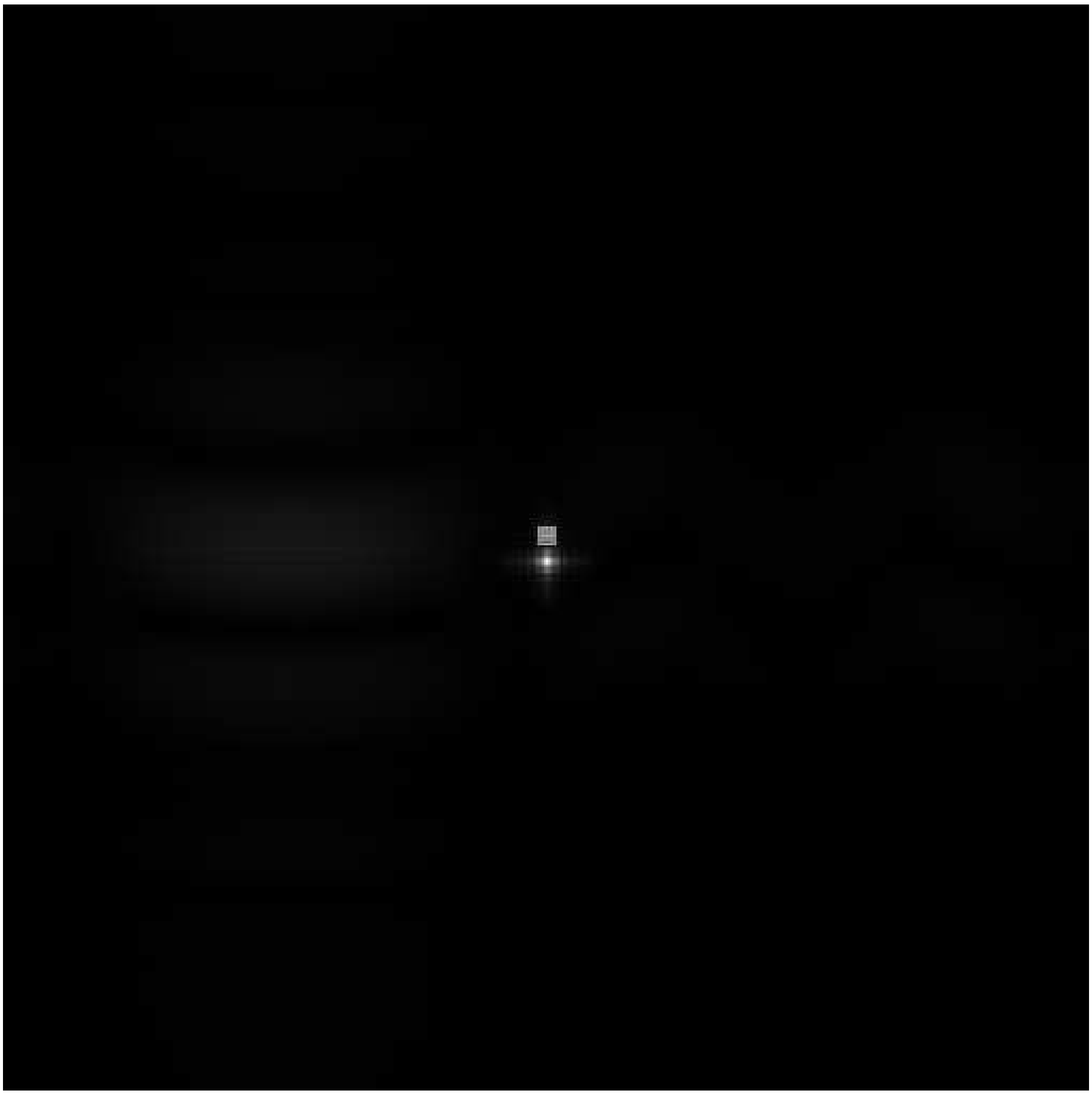

Figure 3.15: Magnitude of another reconstructed object from the off-axis hologram of Figure 3.13

Chapter 4

Plane Wave Spectrum Simulator

4.1 Introduction

In this chapter, we present a modified technique for calculating the diffraction field. The method is computationally fast because it uses the Fast Fourier Transform(FFT) algorithm. Furthermore, it is based on the Rayleigh-Sommerfeld diffraction integral so there is no need to have Fresnel or Fraunhofer approximations. The scalar optical diffraction between tilted input and observation plane can be calculated by using the model presented. The chapter includes continuous and discrete theory of the method. Then the simulator based on the method is presented. The simulator is built up by two parts. First part of the simulator generates the off-axis hologram of the given object. Second part of the simulator is used to reconstruct the object from the off-axis hologram. After that simulation results and conclusions are given.

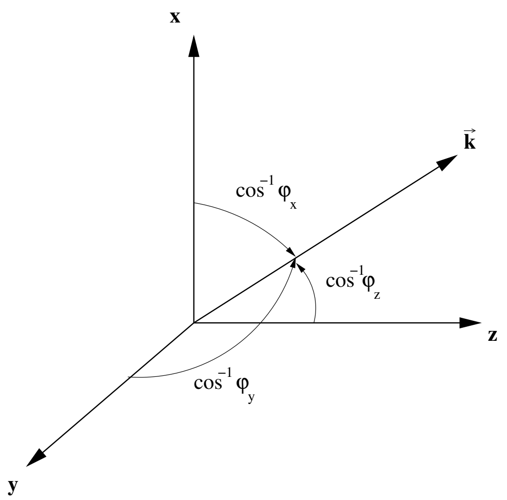

Figure 4.1: Illustration of vector $\vec{k}$

4.2 Off-axis Hologram Calculation

Scalar optical diffraction can be calculated by using several models. As it is shown in Chapter 3, it can be obtained by superposition of the diffraction patterns of the point light sources which make up the input plane. However, the calculation of the diffraction pattern on the observation plane is a time consuming process when a method such as that in Chapter 3 is used. Therefore, models that can provide fast computations have been searched for years [2], [27] and [32]. In this work, plane wave spectrum approach is used to calculate the diffraction pattern, because it allows fast computation.

The diffraction formulation for monochromatic coherent wave, shown in Eq. 2.7, can also be expressed in the frequency domain [13], [32] and is shown as

$$\psi(\vec{x}) = \int A(k_x, k_y) e^{j\vec{k}^T\vec{x}} dk_x dk_y \tag{4.1}$$

where $\vec{x}$ is the position vector given as $[\begin{array}{ccc} x & y & z \end{array}]^T$. The parameter $\vec{k}$ is the three-dimensional wave vector whose components are k_x, k_y and k_z representing the spatial frequency of the propagating wave along the x, y and z axes as illustrated in Figure 4.1. The parameters φ_x, φ_y and φ_z represent the directional cosines and their mathematical expressions are given as

$$\varphi_x = \frac{\lambda}{2\pi} k_x, \quad \varphi_y = \frac{\lambda}{2\pi} k_y, \quad \varphi_z = \frac{\lambda}{2\pi} k_z \quad . \tag{4.2}$$

As it can be seen from the Eq. 4.2 and Figure 4.1, they are interrelated through

$$\varphi_z = \sqrt{1 - {\varphi_x}^2 - {\varphi_y}^2} \quad . \tag{4.3}$$

The term $\psi(\vec{x})$ is the three-dimensional field and $A(k_x, k_y)$ is the complex amplitude of the plane waves which propagate along the $\vec{k}$ direction. Moreover, replacing $z = 0$ into Eq. 4.1, we obtain the field on a reference plane $z = 0$ as

$$f(x, y) \triangleq \psi(x, y, 0) = \int A(k_x, k_y) e^{j(k_x x + k_y y)} dk_x dk_y \ . \tag{4.4}$$

We observe from Eq. 4.4 that $\frac{A(k_x,k_y)}{(2\pi)^2}$ equals to the 2-D Fourier transform (FT) of the field on $z = 0$ plane.

By using Eq. 4.1, we can find the diffraction pattern on an observation plane. The observation plane is spanned by $\vec{x'} = \mathbf{R}\vec{x} + \vec{b}$ as x takes values over the input plane. The parameter $\mathbf{R}$ is a rotation matrix and $\vec{b}$ is the translation vector in space. The rotation matrix $\mathbf{R}$ is defined as

$$\mathbf{R} = \begin{bmatrix} r_{11} & r_{12} & r_{13} \\ r_{21} & r_{22} & r_{23} \\ r_{31} & r_{32} & r_{33} \end{bmatrix} \tag{4.5}$$

Moreover, the rotation matrix has some properties. One of the properties of the rotation matrix $\mathbf{R}$ is the transpose of the matrix $\mathbf{R}$ represented as $\mathbf{R}^T$ equals to the inverse of the matrix $\mathbf{R}$ shown as $\mathbf{R}^{-1}$. Also, the rows of $\mathbf{R}$ represent the coordinates in the original space of unit vectors along the coordinate axes of the rotated space and the columns of $\mathbf{R}$ represent the coordinates in the rotated space of unit vectors along the axes of the original space. There is an illustration of a typical scenario in Figure 4.2. We define $z = 0$ plane as the input plane and it is spanned by $\hat{x} = (1, 0, 0)$ and $\hat{y} = (0, 1, 0)$ unit vectors. Moreover, the observation plane is spanned by $\hat{x'} = \mathbf{R}\hat{x}$ and $\hat{y'} = \mathbf{R}\hat{y}$ unit vectors originating from point $\vec{b}$.

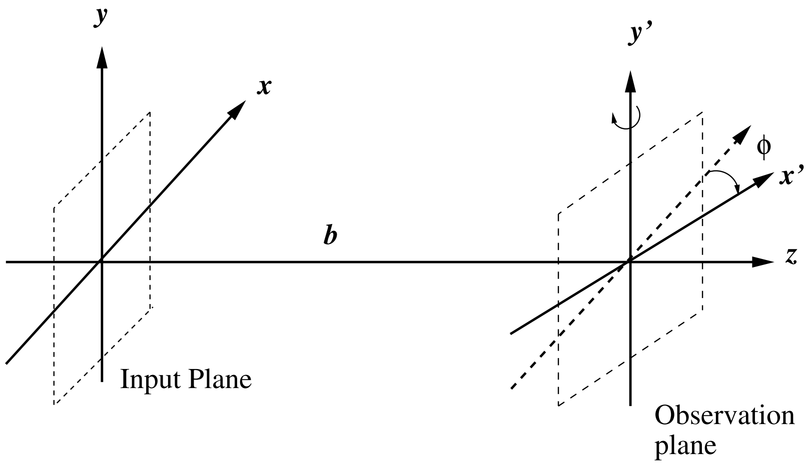

Figure 4.2: Illustration of a scenario which has tilted observation plane around y-axis

To obtain the diffraction pattern on the observation plane, $\vec{x'} = \mathbf{R}\vec{x} + \vec{b}$ is substituted into Eq. 4.1. Then, we get the mathematical expression of the diffraction pattern on observation plane as

$$\begin{aligned} g(x', y') \triangleq \psi(\mathbf{R}\begin{bmatrix} x \\ y \\ 0 \end{bmatrix} + \vec{b}) &= \int A(\vec{k}) e^{j(\vec{k}^T(\mathbf{R}\vec{x}+\vec{b}))} dk_x dk_y \\ &= \int A(\vec{k}) e^{j((\mathbf{R}^T\vec{k})^T\vec{x})} e^{j\vec{k}^T\vec{b}} dk_x dk_y \\ &= \int A(\mathbf{R}\vec{k'}) e^{j(\vec{k'}^T\vec{x})} e^{j(\mathbf{R}\vec{k'})^T\vec{b}} J(k_z, k'_z) dk'_x dk'_y \end{aligned} \tag{4.6}$$

where $\vec{k'}$ represents the propagation direction of plane waves with respect to the observation plane. The relation between $\vec{k}$ and $\vec{k'}$ represents a frequency mapping operation and it is given as $\vec{k} = \mathbf{R}\vec{k'}$. In other words, the frequency components of the signal on the input plane, which gives the complex coefficients of the plane waves, are assigned to the frequency components of a signal on the observation plane. For instance, let us consider a plane wave propagate from the input plane to the observation plane along the z-axis and it is parallel to the input plane. When the plane wave reaches the observation plane, it is described by another frequency component. As a result of this, each the frequency component of the input plane is mapped to a specific frequency component of the observation plane. The function $J(k_z, k'_z)$ is the Jacobian and equals to $\frac{k_z}{k'_z}$. Appendix B contains how we can obtain an equivalent of the Jacobian. Please note that k'_z is a function of k'_x and k'_y; and the relation is given as

$$k'_z = \sqrt{(\frac{2\pi}{\lambda})^2 - (k'_x)^2 - (k'_y)^2} \tag{4.7}$$

Furthermore, k_z is a function of k_x and k_y. By using the frequency mapping relation $\vec{k} = \mathbf{R}\vec{k'}$, we can obtain k_z from k'_x and k'_y. The explicit relations between k_x, k_y, k_z and k'_x, k'_y, k'_z are

$$\begin{aligned} k_x &= r_{11}k'_x + r_{12}k'_y + r_{13}\sqrt{k^2 - {k'_x}^2 - {k'_y}^2} \\ k_y &= r_{21}k'_x + r_{22}k'_y + r_{23}\sqrt{k^2 - {k'_x}^2 - {k'_y}^2} \\ |k_z| &= \sqrt{k^2 - {k_x}^2 - {k_y}^2} \end{aligned} \tag{4.8}$$

As it is seen from the Eq. 4.8, the frequency mapping operation is performed on a surface of a sphere. The terms $\sqrt{k^2 - {k'_x}^2 - {k'_y}^2}$ and $\sqrt{k^2 - {k_x}^2 - {k_y}^2}$ define the surface of the sphere. The radius of the sphere is determined by the parameter k which equals to $\frac{2\pi}{\lambda}$. Therefore, the frequency range of the signals on the input and observation planes can be effected by the curvature of the sphere. In most cases the input signal which represents the input field is a base-band signal. As a result of this, the frequency range of the signal which is obtained after the frequency mapping operation is affected by the curvature of the sphere. There is an illustration of the frequency mapping operation for a specific scenario in Figure 4.3. The region in Figure 4.3 that forms a circle and labelled as number 1 represents the frequency range in scalar optical diffraction. The gray region in Figure 4.3 which is labelled with the number 2 is the frequency range of the input field. Also it can be seen from the Figure 4.3 that the maximum frequency of the input signal is about $\frac{1}{4\lambda}$. Because the width of the frequency region of the input signal is about $\frac{1}{4}$ of the diameter of the circle. The white region in Figure 4.3 labelled with the number 3 provides the frequency region of the signal that is obtained after the frequency mapping operation $\vec{k} = \mathbf{R}\vec{k'}$. In this illustration there is a 45° tilt angle around the y-axis. Moreover, effect of the curvature can be easily seen on the white region.

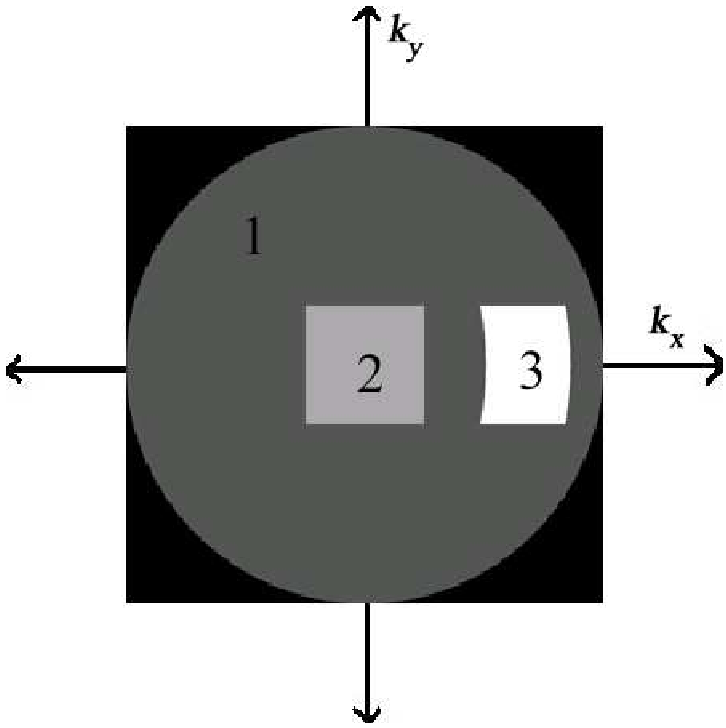

Figure 4.3: Illustration of frequency mapping operation

The term $e^{j\vec{k}^T\vec{b}}$ which is given in Eq. 4.6 provides the phase delay for each plane wave and it is represented by the function $H(\vec{k'},\mathbf{R},\vec{b})$. Moreover, the function $H(\vec{k'},\mathbf{R},\vec{b})$ is the Fourier transform of the kernel defined in Eq. 3.6. Also, the mathematical expression of the function $H(\vec{k'},\mathbf{R},\vec{b})$ is found as

$$H(\vec{k'},\mathbf{R},\vec{b}) = e^{j(\mathbf{R}\vec{k'})^T\vec{b}} \quad . \tag{4.9}$$

The relation between $f(x,y)$ and $g(x,y)$ can be obtained from Eq. 4.4 and Eq. 4.6 as

$$g(x',y') = \frac{1}{4\pi^2}\mathcal{F}^{-1}{}_{\vec{k'}\to\vec{x'}}\left\{4\pi^2\mathcal{F}_{\vec{x}\to\vec{k}}\{f(x,y)\}\Big|_{\vec{k}\to\mathbf{R}\vec{k'}} H(\vec{k'},\mathbf{R},\vec{b})\frac{k_z}{k'_z}\right\} \tag{4.10}$$

where $F(k_x,k_y)$ is the FT of the $f(x,y)$. Please note that $4\pi^2$ and $\frac{1}{4\pi^2}$ terms cancel each other and therefore not necessarily needed for the implementation of the algorithm.

Discrete model of the system, which represents the scalar optical system diffraction, is obtained by sampling equations 4.4 and 4.6. Sampling a signal in space domain causes replications in its frequency domain representation, and vice versa. Therefore in discrete environment we can deal only with periodic inputs and outputs. The implemented simulator displays only one period of the input and the output. By sampling the space and the frequency domains, we obtain

$$x = Xn_s,\ y = Xm_s$$
$$k'_x = \frac{2\pi}{NX}n'_f,\ k'_y = \frac{2\pi}{NX}m'_f \tag{4.11}$$

where X is the sampling period. The variable N shows the size of the frame we deal with. The discrete variables n_s and m_s represent the space points that we take samples. Also n'_f and m'_f provide the frequency components that we use in the calculations. Moreover, the discrete variables n_s, m_s, n'_f and m'_f are integer numbers in the range $[-N/2, N/2)$ [12], [13]. The discrete version of k'_z is

$$k'_z = \frac{2\pi}{NX}\sqrt{\beta^2 - {n'_f}^2 - {m'_f}^2} \tag{4.12}$$

where β is equal to $\frac{NX}{\lambda}$.

The variables k'_x and k'_y are uniformly sampled. Hence the angle between the consecutive plane wave components, as represented by the corresponding $\vec{k_D}'$, which is the discrete version of $\vec{k'}$, becomes larger as the wave vector of the plane wave moves away from the observation plane normal. An illustration of the discrete frequencies is given by Figure 4.4. In the Figure, the number of plane waves in the x direction is eight. Black dots represent the different plane wave components making up the optical field distribution. As it is seen from the Figure 4.4 weight of the frequency components which are away from the plane normal need to be adjusted. Moreover, there is a non-uniform sampling in $\vec{k}$ domain. Weight adjustment and nonuniform sampling affects the weights of the samples in such a way to cancel the Jacobian in Eq. 4.6. Therefore the Jacobian in the Eq. 4.6 vanishes in the discrete version.

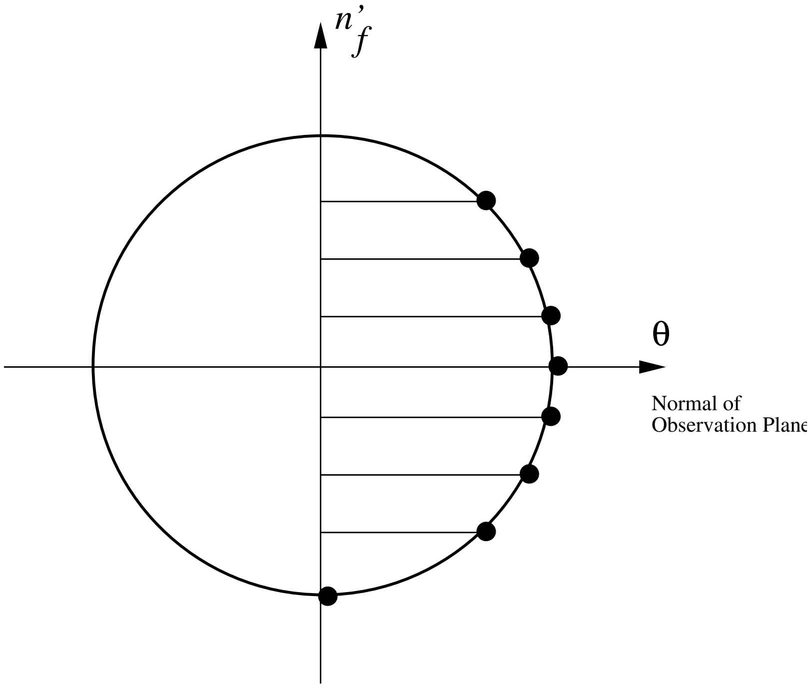

Figure 4.4: Illustration of the discrete frequencies

The sampled periodic input field in continuous domain is represented as

$$f(x, y) = \sum_{n_s, m_s} f_D(n_s, m_s)\delta(x - n_s X, y - m_s X) \tag{4.13}$$

where the signal $f_D(n_s, m_s)$ is the samples of the input field in continuous domain. It may be assumed that the Nyquist criteria is satisfied while sampling the input field. There is a 2-D illustration which is useful to visualize how the samples are taken on the input plane in Figure 4.5. To calculate the diffraction field on the observation plane by using the plane wave spectrum model, we have to calculate the coefficients of the plane waves generated by the input field. The coefficients of the plane waves can be obtained by the Fourier transform of the input field as mentioned in Eq. 4.4. The coefficients of the plane waves are obtained as

$$A(k_x, k_y) = \sum_{n_s, m_s} f_D(n_s, m_s) e^{-j(k_x n_s X + k_y m_s X)} \ . \tag{4.14}$$

Therefore, the signal $A(k_x, k_y)$ is periodic with 2π and determines the coefficients of the N^2 different plane waves. The signal $A(k_x, k_y)$ is represented in the baseband as

$$\begin{aligned}
A(k_x, k_y) &= \sum_{n_f, m_f} A_D(n_f, m_f)\delta(k_x - n_f\frac{2\pi}{NX}, k_y - m_f\frac{2\pi}{NX}) \\
&= \sum_{n_f, m_f} \sum_{n_s, m_s} f_D(n_s, m_s) e^{-j\frac{2\pi}{N}(n_f n_s + m_f m_s)} \qquad (4.15) \\
&\qquad\qquad \delta(k_x - n_f\frac{2\pi}{NX}, k_y - m_f\frac{2\pi}{NX})
\end{aligned}$$

where the variable $A_D(n_f, m_f)$ provides the samples of the signal $A(k_x, k_y)$.

The plane waves generated by the input field constructs the diffraction field on the observation plane. The diffraction field on the observation plane is uniformly sampled and the spatial sampling period is taken as X and how the samples are taken can be seen in the Figure 4.5. The tilt angle around y-axis is taken as $30°$ in the illustration of the scenario in Figure 4.5. Also, we use N^2 different plane waves to construct the diffraction field on the observation plane. Moreover, we want to use FFT algorithm for fast computation. Therefore the spatial frequency interval between consecutive plane wave has to be uniform. In the presented plane wave spectrum model the spatial frequency interval is taken as $\frac{1}{NX}$. Therefore in some scenarios we need the coefficient of the plane wave in between two consecutive plane waves generated by the input field. The plane wave which is needed is determined by the relation $\vec{k} = \mathbf{R}\vec{k'}$. Replacing $k'_x = \frac{2\pi}{NX}n'_f$, $k'_y = \frac{2\pi}{NX}m'_f$ and $k'_z = \frac{2\pi}{NX}\sqrt{\beta^2 - {n'_f}^2 - {m'_f}^2}$ provides spatial frequency of the plane waves which are needed to construct the diffraction field on the observation plane. However, we have only N^2 different plane waves which are generated by the input field and their coefficients. Therefore, we use bilinear interpolation to find the coefficients of the plane waves.

The discrete simulation of the model is performed by the steps indicated below:

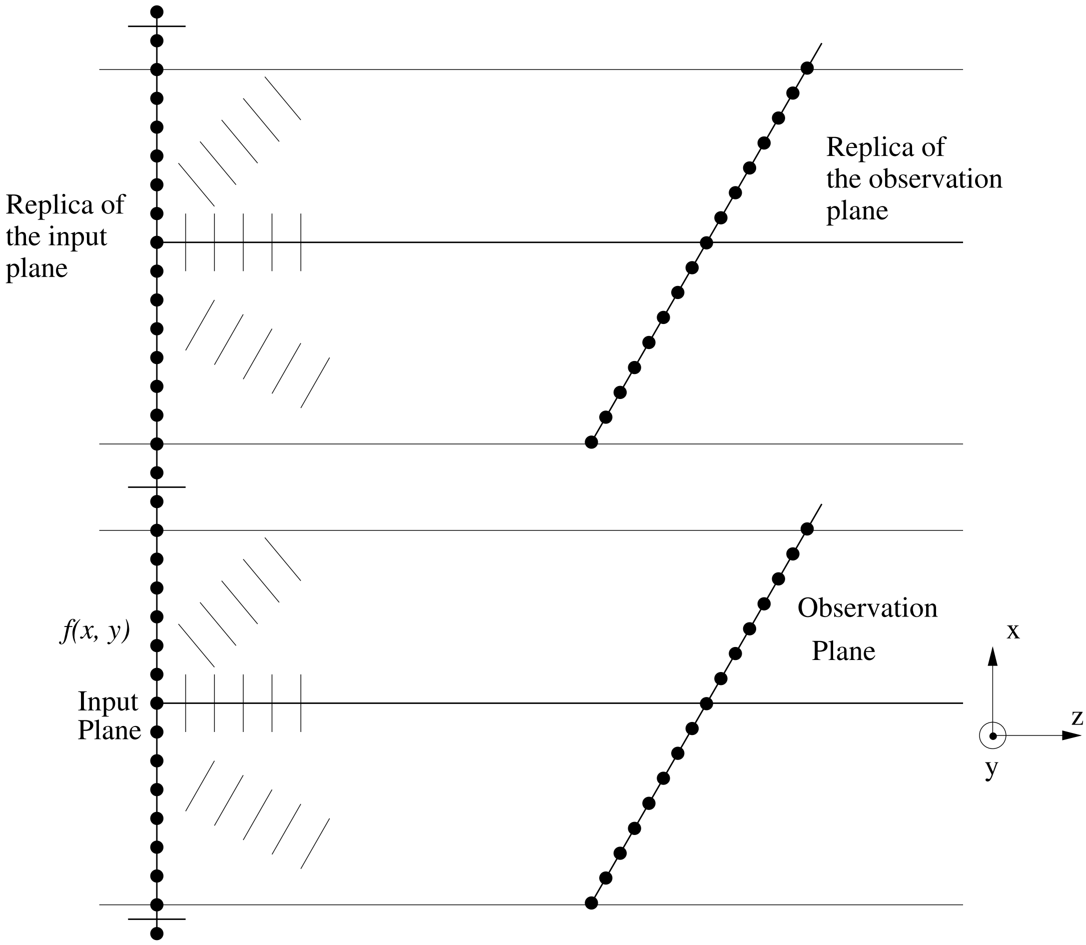

Figure 4.5: Illustration of a sampled input and observation plane and the plane waves generated by the input field.

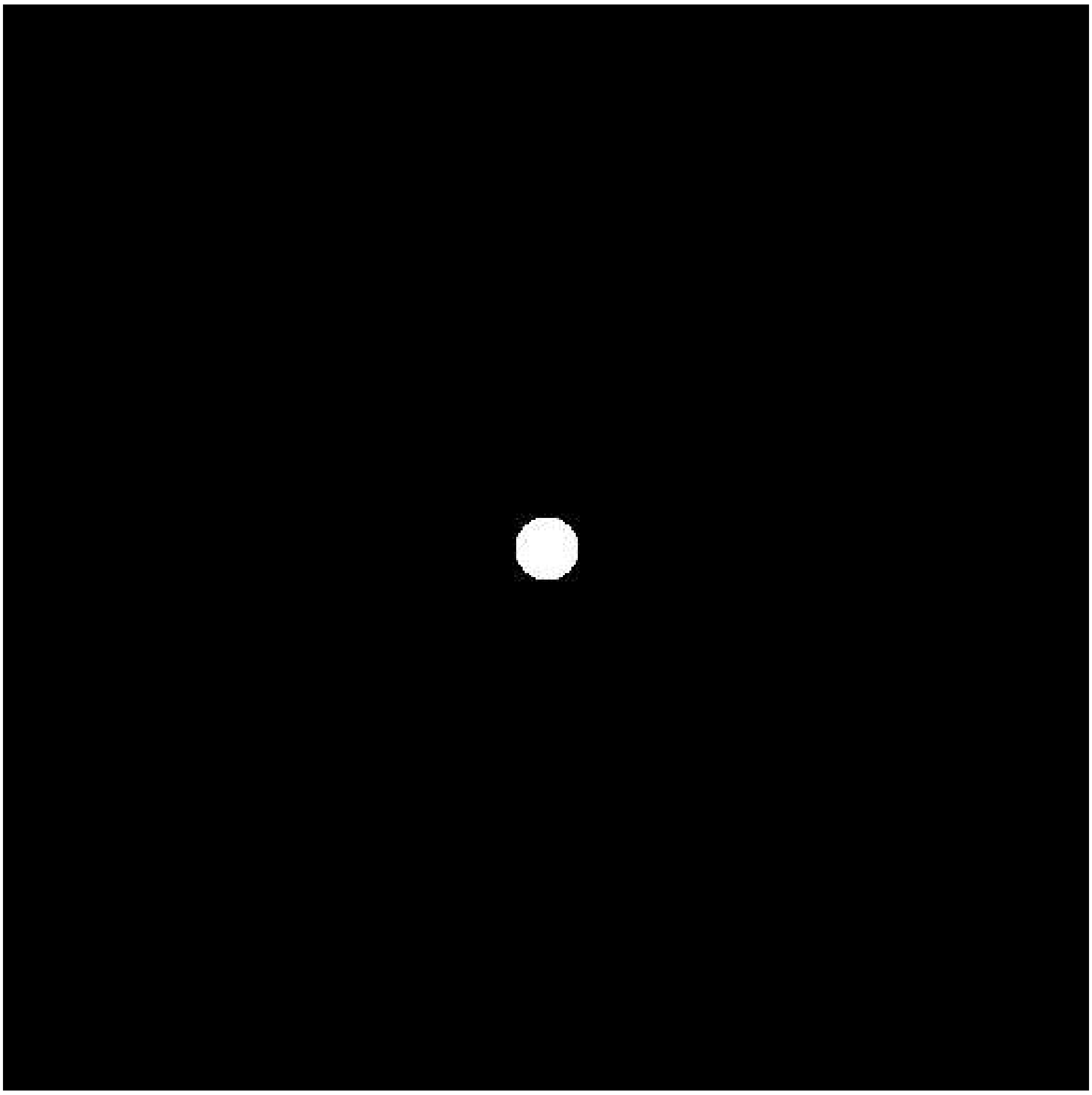

Figure 4.6: An input object

An NxN input array is given by the user. There is an example in Figure 4.6. This array represents the samples of a periodic $f(x, y)$ which are taken in the range $(x, y)\epsilon[\frac{-NX}{2}, \frac{NX}{2})$. Then, an NxN array $f_D(n_s, m_s)$ is created from corresponding samples in the range $(x, y)\epsilon[0, NX)$ of $f(x, y)$ by periodically shifting the given input, accordingly. After that $A_D(n_f, m_f)$ is computed as

$$A_D(n_f, m_f) \triangleq N^2 DFT_{N\mathrm{x}N}\big\{f_D(n_s, m_s)\big\}. \tag{4.16}$$

The array $A_D(n_f, m_f)$ provides the complex amplitudes of the plane waves which suppose in 3-D space to give the 2-D pattern over the input plane. The periodic extension of $A_D(n_f, m_f)$ provides the function $\tilde{A}_D(n_f, m_f)$. Moreover,

$\tilde{A}_{1,D}(n'_f, m'_f)$ is defined as

$$\tilde{A}_{1,D}(n'_f, m'_f) \triangleq \tilde{A}_D(u(n'_f, m'_f), v(n'_f, m'_f)) \tag{4.17}$$

where (n'_f, m'_f) is in the range $[\frac{-N}{2}, \frac{N}{2})$ and $u(n'_f, m'_f)$ and $v(n'_f, m'_f)$ are computed as

$$\begin{aligned} u(n'_f, m'_f) &= (n'_f + s)r_{11} + (m'_f + t)r_{12} \\ &+ \sqrt{\beta^2 - (n'_f + s)^2 - (m'_f + t)^2} r_{13} \\ v(n'_f, m'_f) &= (n'_f + s)r_{21} + (m'_f + t)r_{22} \\ &+ \sqrt{\beta^2 - (n'_f + s)^2 - (m'_f + t)^2} r_{23} \end{aligned} \tag{4.18}$$

where s, t are chosen to be equal to $r_{31}\beta$ and $r_{32}\beta$, respectively. This operation is needed to compute $A(\mathbf{R}\vec{k'})$ given in Eq. 4.6. The function $f(x, y)$ usually represents a base-band signal. Therefore, the frequency components of $A(k_x, k_y)$ are concentrated around the origin. The transformation $\vec{k'} = \mathbf{R}^{-1}\vec{k}$ moves the concentration in Eq. 4.6 from around $(k_x, k_y) = (0, 0)$ to around $(k'_x, k'_y) = (r_{31}\beta, r_{32}\beta)$. Therefore, the signal in Eq. 4.6 whose inverse FT (IFT) is going to be taken, is usually a band-pass signal. To avoid unnecessarily large discrete FT (DFT) sizes, the band-pass signal is converted to a base-band signal by introducing the s and t in Eq. 4.18 during the discrete computations. Please note that $u(n'_f, m'_f)$ and $v(n'_f, m'_f)$ are no longer integers for integer n'_f, m'_f.

The array P describes a function obtained from $\tilde{A}_D(n_f, m_f)$ by bilinear interpolation. The interpolation process is achieved by using nearest 4 pixels to the location indicated by $u(n'_f, m'_f)$ and $v(n'_f, m'_f)$. There is an illustration that describes how the interpolated data is obtained in Figure 4.7. The numbers 1, 2, and 3 in the Figure 4.7 represent sequence of the linear interpolations that are applied to the nearest 4 pixels to get the bilinear interpolated data. Figure 4.8 provides square root of magnitude of a typical $A_D(n_f, m_f)$. We display square root of the magnitude because we want to improve the visibility of the frequency

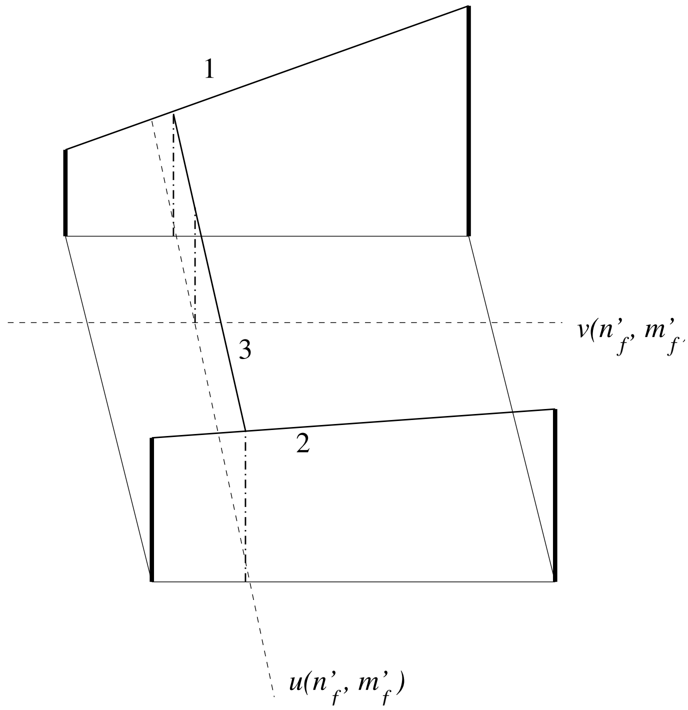

Figure 4.7: The bilinear interpolation

terms towards the edges. The square root operation provides a nonlinear normalization on the magnitude of the $A_D(n_f, m_f)$. Figure 4.9 provides square root of magnitude of $\tilde{A}_{1,D}(n'_f, m'_f)$.

The discrete version of the Fourier transform of the kernel in Eq. 4.9 is represented by the term $H_D(\vec{k'}_D, \mathbf{R}, \vec{b})$ and it is obtained as

$$H_D(\vec{k'}_D, \mathbf{R}, \vec{b}) = e^{j\frac{2\pi}{NX}\ \vec{k_D}^T \vec{b}} \tag{4.19}$$

where $\vec{k_D}^T$ equals to $(n_f, m_f, \sqrt{\beta^2 - {n_f}^2 - {m_f}^2})$. Figure 4.10 provides the real part of a Fourier transform of a kernel of the discrete system. The wavelength is taken as 633 nm and the sampling period equals to 2λ. Moreover there are no rotations around x-axis and y-axis and the translation vector $\vec{b}$ is chosen as 1.30 mm.

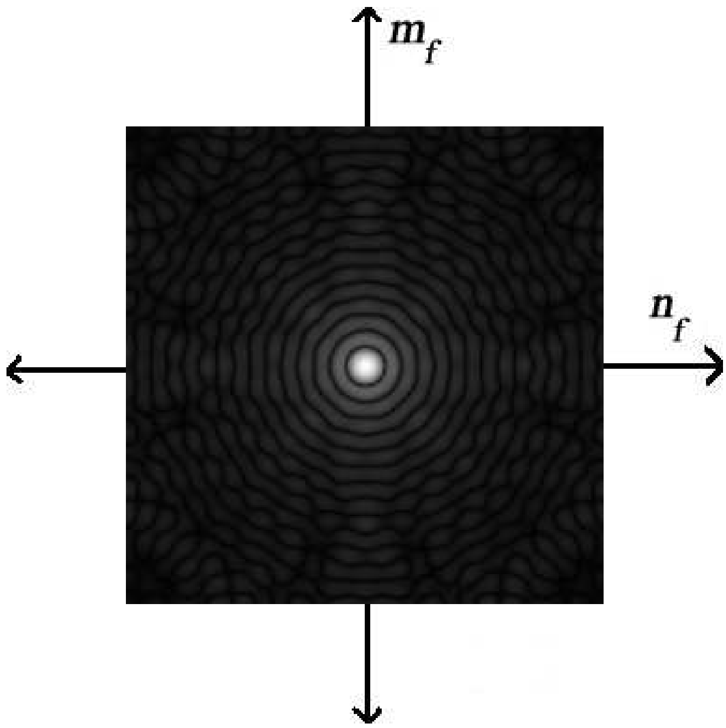

Figure 4.8: Square root of magnitude of $A_D(n_f, m_f)$ corresponding to the object in Figure 4.6. The variables n_f and m_f are integer and they are in the range $[\frac{-N}{2}, \frac{N}{2})$.

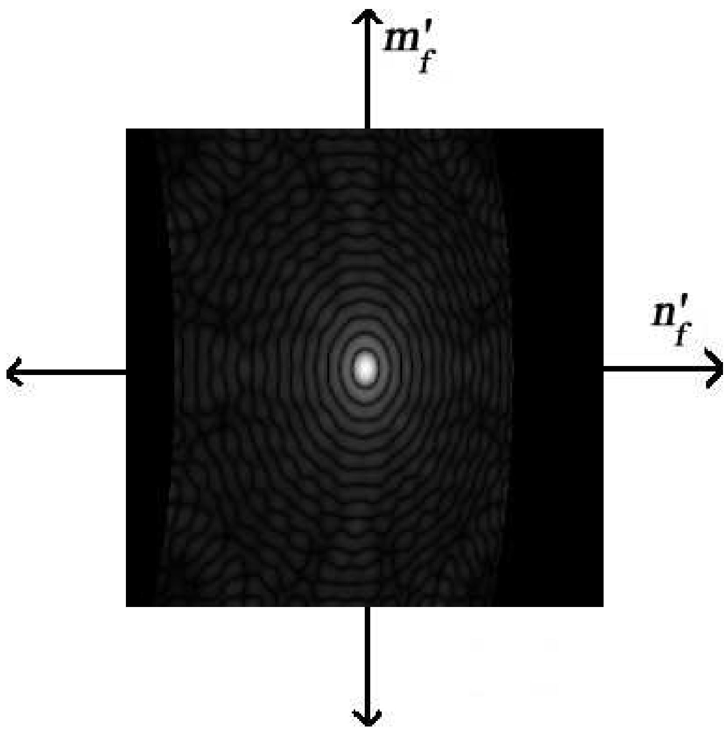

Figure 4.9: Square root of magnitude of $\tilde{A}_{1,D}(n'_f, m'_f)$ corresponding to $A_D(n_f, m_f)$ of Figure 4.8. The variables n'_f and m'_f are integer and they are in the range $[\frac{-N}{2}, \frac{N}{2})$.

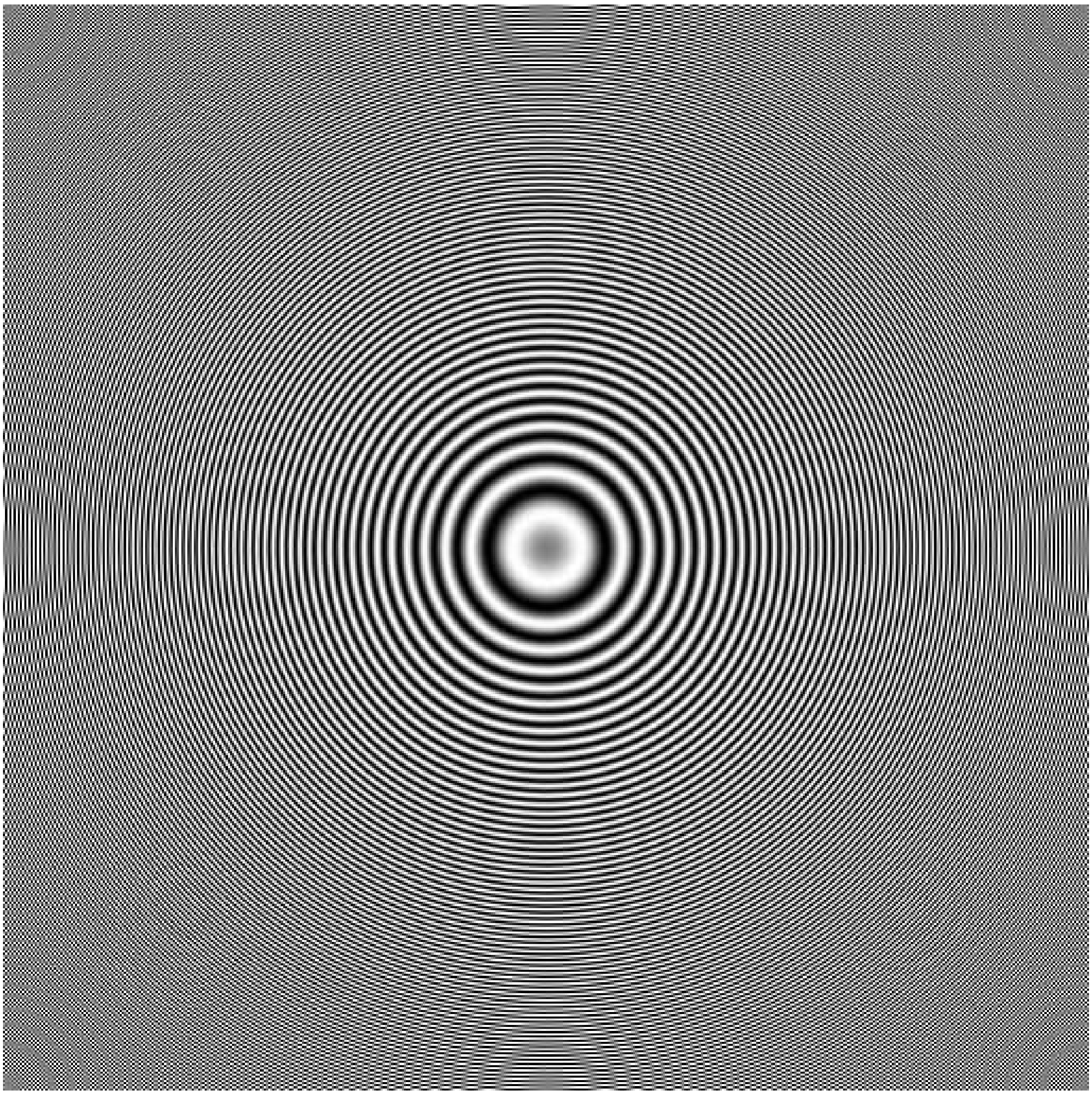

Figure 4.10: Real part of Fourier transform of a kernel of the discrete system

The discrete form of Eq. 4.6 is obtained as

$$g_D(n'_s, m'_s) \triangleq \left\{ \sum_{n'_f, m'_f = 0}^{N-1} \tilde{A}_{1,D}(n'_f, m'_f) e^{j\frac{2\pi}{N}(n'_s n'_f + m'_s m'_f)} e^{j\frac{2\pi}{NX} \ \vec{k_D}^T \vec{b}} \right\} e^{j\frac{2\pi}{N}(n'_s s + m'_s t)} \tag{4.20}$$

$$\left\{ \sum_{n'_f, m'_f = 0}^{N-1} \tilde{A}_{1,D}(n'_f, m'_f) e^{j\frac{2\pi}{N}(n'_s n'_f + m'_s m'_f)} H_D(\vec{k'}_D, \mathbf{R}, \vec{b}) \right\} e^{j\frac{2\pi}{N}(n'_s s + m'_s t)}.$$

The term $e^{j\frac{2\pi}{N}(n'_s s + m'_s t)}$ is used to modulate the signal because the signal is demodulated by using s and t parameters while filling the array $\tilde{A}_{1,D}(n'_f, m'_f)$. The function $g_D(n'_s, m'_s)$ is the discrete form of $\psi(\mathbf{R}(x, y, 0)^T + \vec{b})$. Consequently, the relation between $f_D(n_s, m_s)$ and $g_D(n'_s, m'_s)$ is given as

$$g_D(n'_s, m'_s) = \frac{1}{N^2} DFT^{-1}\{\tilde{A}_{1,D}(n'_f, m'_f) H_D(\vec{k'}_D, \mathbf{R}, \vec{b})\} e^{j\frac{2\pi}{N}(n'_s s + m'_s t)}. \tag{4.21}$$

Please note that N^2 in Eq. 4.16 and $\frac{1}{N^2}$ in the above equation cancels each other and therefore they are not needed during the implementation.

To calculate the off-axis hologram we need a sampled reference beam. Sampling issue of the reference beam is mentioned in Chapter 3 and its mathematical expression is given by Eq. 3.10. The same reference beam is used in the previous chapter is also used in the plane wave spectrum simulator.

The parameters N, X, $\vec{b}$, R_0 and Γ which are used in the simulator, have to be chosen properly because these parameters determine the implemented scenario. The parameters in the calculations depend on the wavelength. Therefore wavelength determines the physical parameters of the implemented scenario. For instance, the translation vector $\vec{b}$ is double precision parameter and we have to multiply it with the spatial sampling period to get the corresponding physical translation. Also the spatial sampling period depends on the wavelength. In the simulated scenarios the variable N is chosen as 512. The variable β is determined by the spatial sampling according to the relation $\beta = \frac{NX}{\lambda}$. Furthermore, the variables Γ and R_0 are chosen as in Chapter 3, because of the reasons that are mentioned in that chapter.

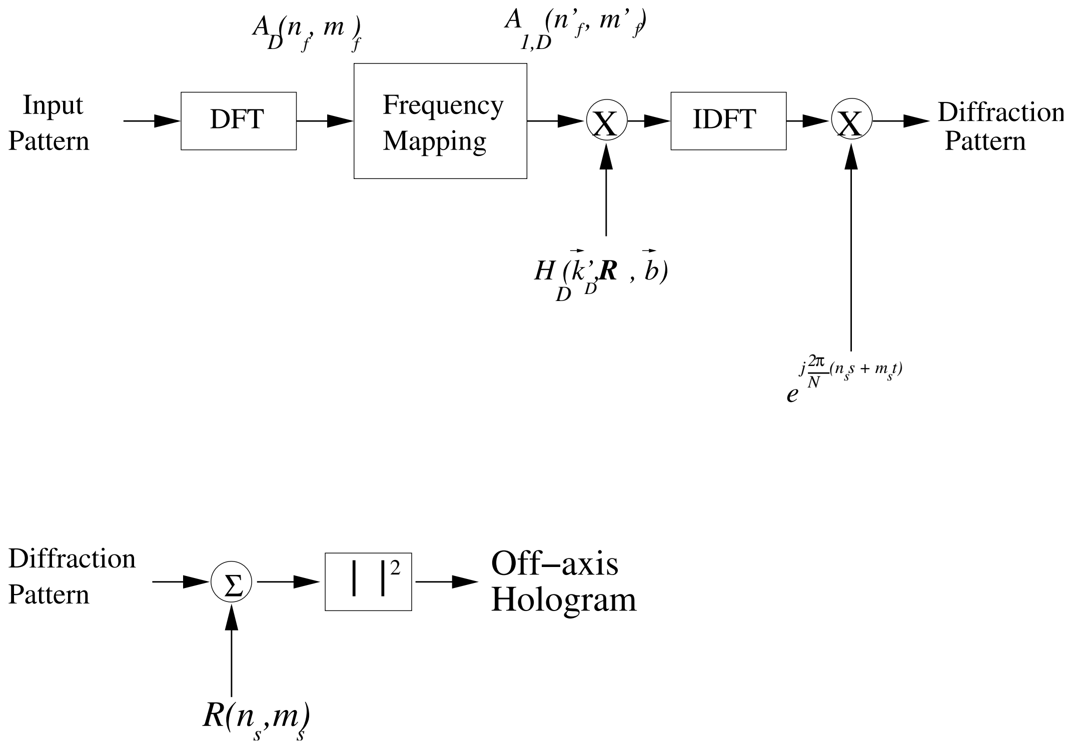

Figure 4.11: Block diagram of plane wave spectrum simulator

The block diagram of the plane wave spectrum simulator described so far in this Chapter is shown in Figure 4.11. The plane wave spectrum simulator needs input files written in binary file format as in the pointwise simulator. Therefore, another program is written to convert popular formats to this specific format.

The diffraction pattern that we can obtain by using the simulator is the diffraction pattern of a periodic input pattern in the physical environment. If the input pattern which is periodic with NX in both x-axis and y-axis is illuminated by a laser which has the same wave length as used in the simulator, we get the same diffraction pattern provided by the simulator. However, the diffraction pattern calculated by the simulator displays only one period of the diffraction pattern. Illustration of the periodicity of the input pattern on the input plane and diffraction pattern on the observation plane is given in Figure 4.12. The mathematical explanation of periodicity is given in Appendix C.

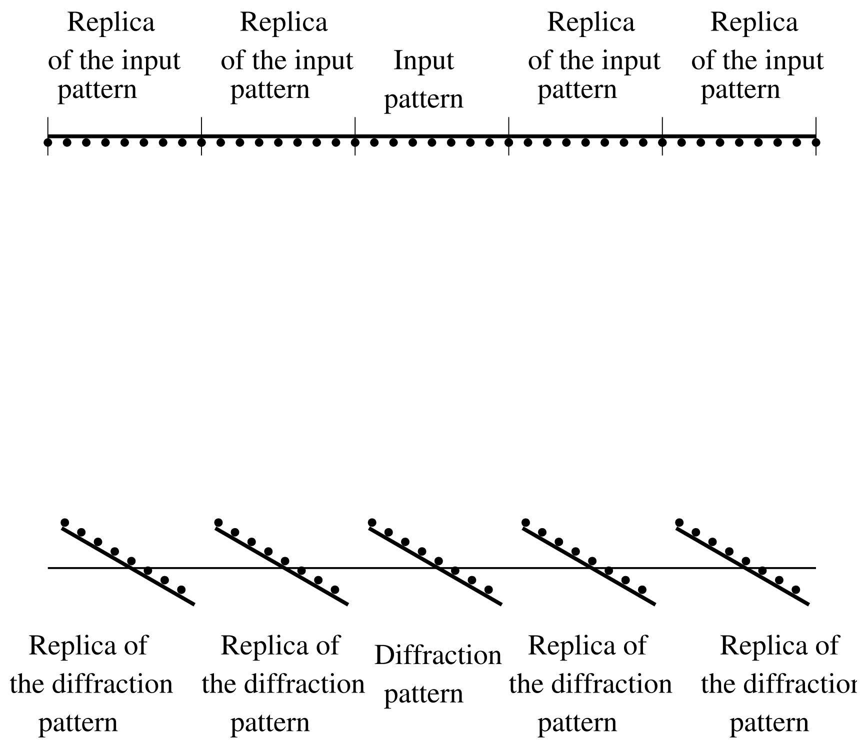

Figure 4.12: An illustration of periodic input and diffraction pattern

The plane wave spectrum simulator calculates scalar optical diffraction between the input and observation planes. Therefore, the object, whose diffraction pattern is calculated, has to be made up of planar faces. In computer graphics, there is a method that uses vertices and faces to construct an object. Fast calculation of the diffraction pattern due to faces brings faster computation compared to pointwise computation. The simulator needs two arrays for each face. One of them provides the light distribution of the face. The other one supplies the location of the center of the window which includes the face and the rotation angles around x-axis and y-axis.

4.3 Reconstruction Process

The reconstruction process is the same as in the pointwise simulator. To get rid of the distortions of the plane wave simulator such as having periodic diffraction pattern and numerical errors caused by the bilinear interpolation, we use pointwise simulator in the reconstruction process. The detailed information on the reconstruction process by using the pointwise simulator is given in subsection 3.3.

4.4 Simulation Results

In the simulations that are presented in this chapter, the variable N which determines the size of the input and the kernel, is taken as 512. The mathematical expression of the Fourier transform of the kernel is given in Eq. 4.9 and there is an illustration of the real part of Fourier transform of a typical kernel in Figure 4.10. To be precise in the calculations 8 bytes (double precision due to the machine used for calculations) are used to represent the variables. Moreover, the simulation results are displayed on the screen and stored in raw image format. The image files have 256 gray levels. The level 0 is used to represent the darkest regions and the level 255 is used to show the brightest regions.

In the simulations several parameters are needed to obtain the simulation results of a scenario. In this chapter, simulation results of six scenarios are given. In these simulations the variable λ is taken as 633 nm. The variables which determine the reference beam R_0 and Γ are chosen as 200 and 0.8, respectively, because we want to suppress the distortion caused by the twin-image. The variable Γ is used to separate the reconstructed object from the twin-image in the spatial domain. The variable R_0 suppresses the cross-term of the object. In the construction process the DC component is subtracted to decrease the effect of the uniform beam of light propagating through the hologram.

In the first simulation, we again investigate the diffraction pattern of the simple object which can be seen in Figure 4.6. The array $f_D(n_s, m_s)$ represents the simple input object. The physical diameter of the circle in Figure 4.6 is

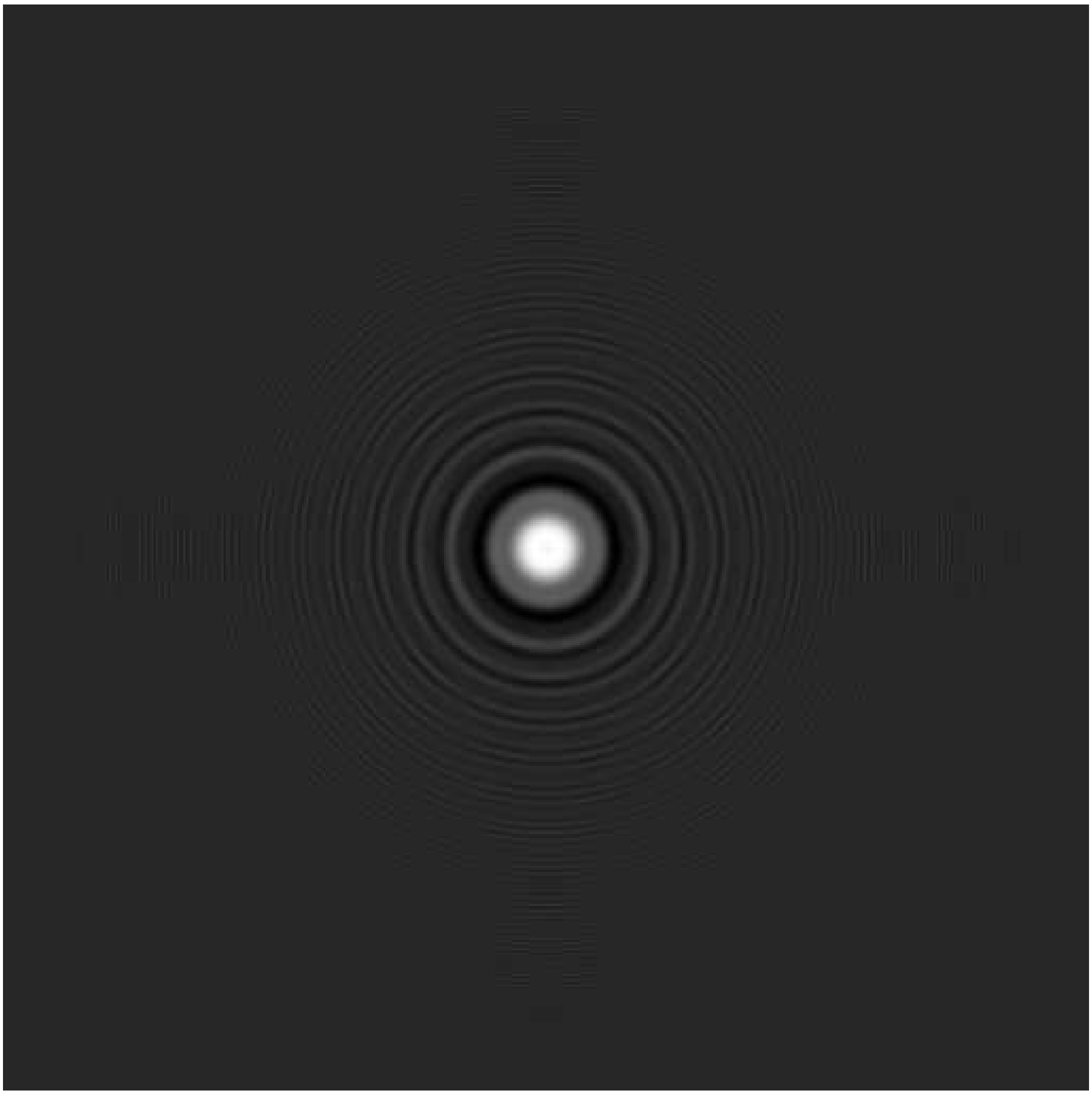

Figure 4.13: Real part of the diffraction pattern corresponds to the input pattern shown in Figure 4.6

0.0188 m. In this simulation, we have parallel input and observation planes. Moreover, there is a 340 m distance between them. Figure 4.13 provides the real part of the diffraction pattern and Figure 4.14 is the cross-section of the real part of the diffraction pattern. The cross-section is taken from the center of it. Figure 4.15 is the magnitude of the obtained diffraction pattern and Figure 4.16 is the cross-section of the magnitude of the diffraction pattern. Figure 4.17 gives the off-axis hologram of the object $f_D(n_s, m_s)$. The reconstructed object can be seen in Figure 4.18. Furthermore, the twin-image can cause distortion on the light distribution of the reconstructed object and it is seen in Figure 4.18.

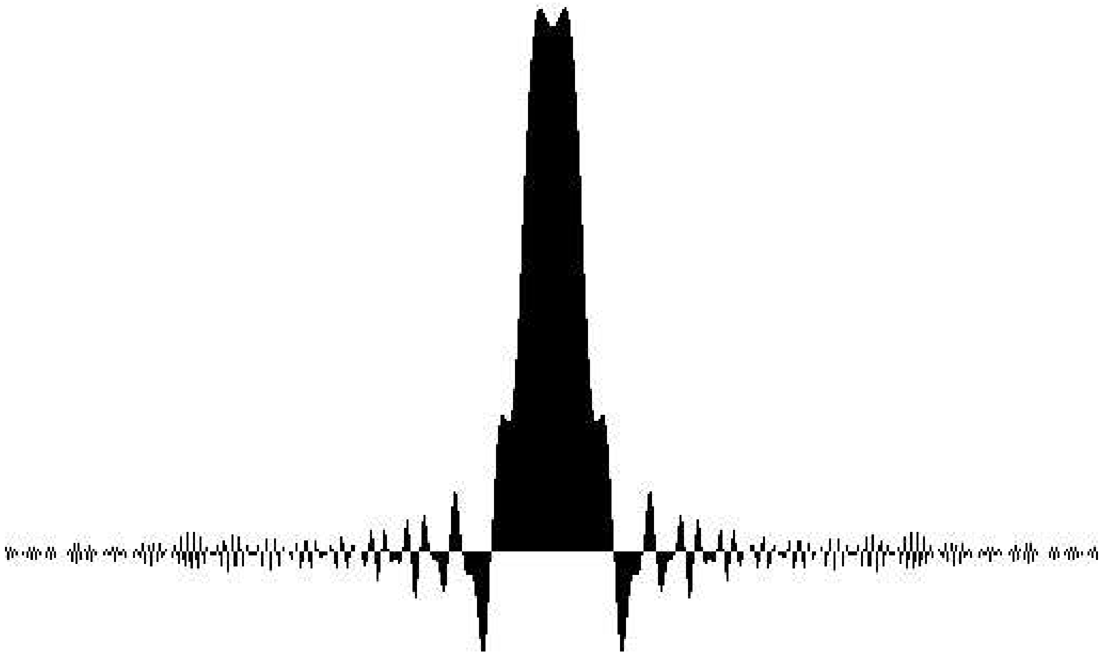

Figure 4.14: Cross-section at center of real part of the diffraction pattern shown in Figure 4.13

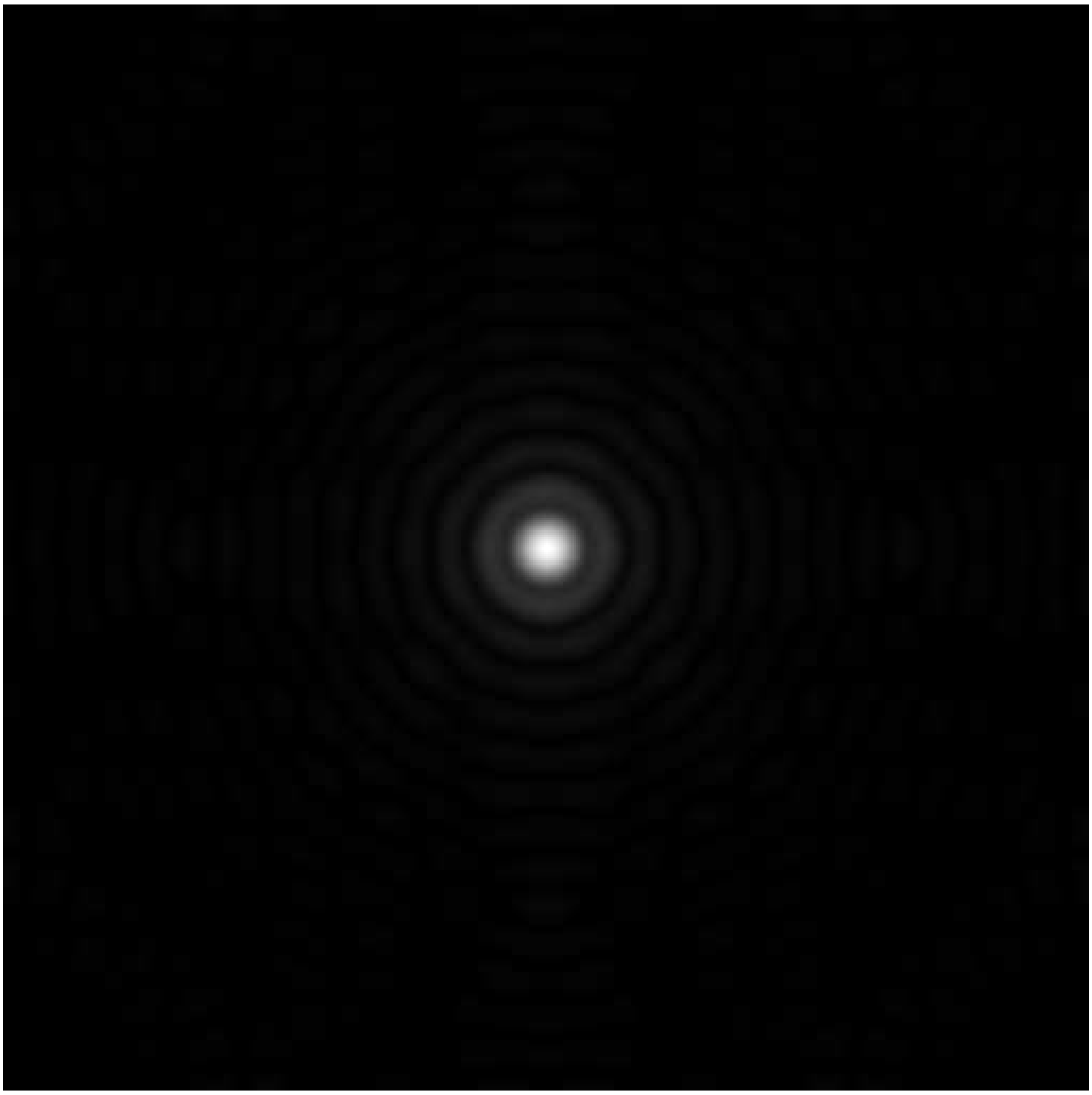

Figure 4.15: Magnitude of the diffraction pattern corresponds to the input pattern shown in Figure 4.6

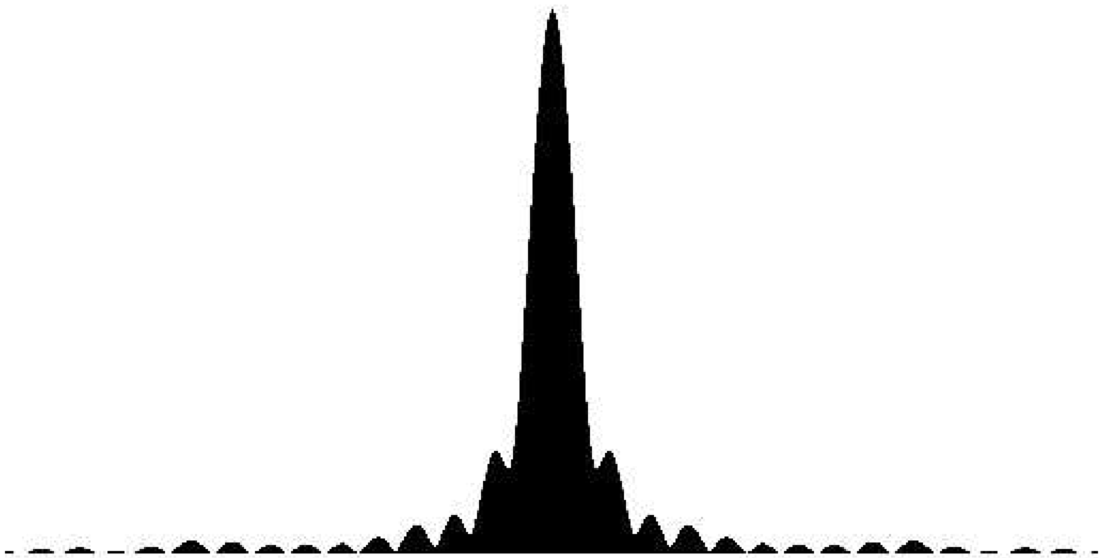

Figure 4.16: Cross-section at center of magnitude part of the diffraction pattern shown in Figure 4.15

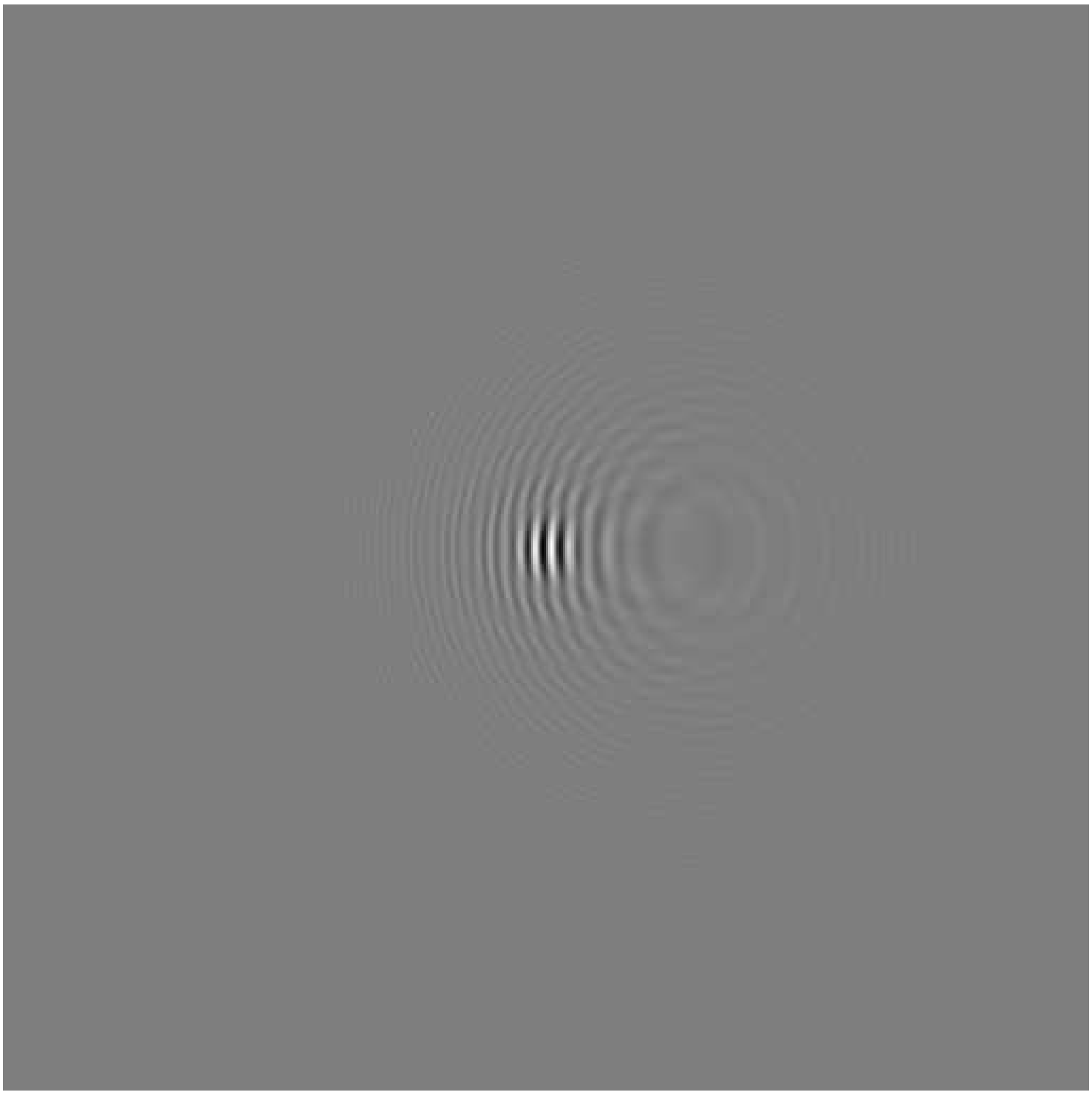

Figure 4.17: Off-axis hologram of the object shown in Figure 4.6

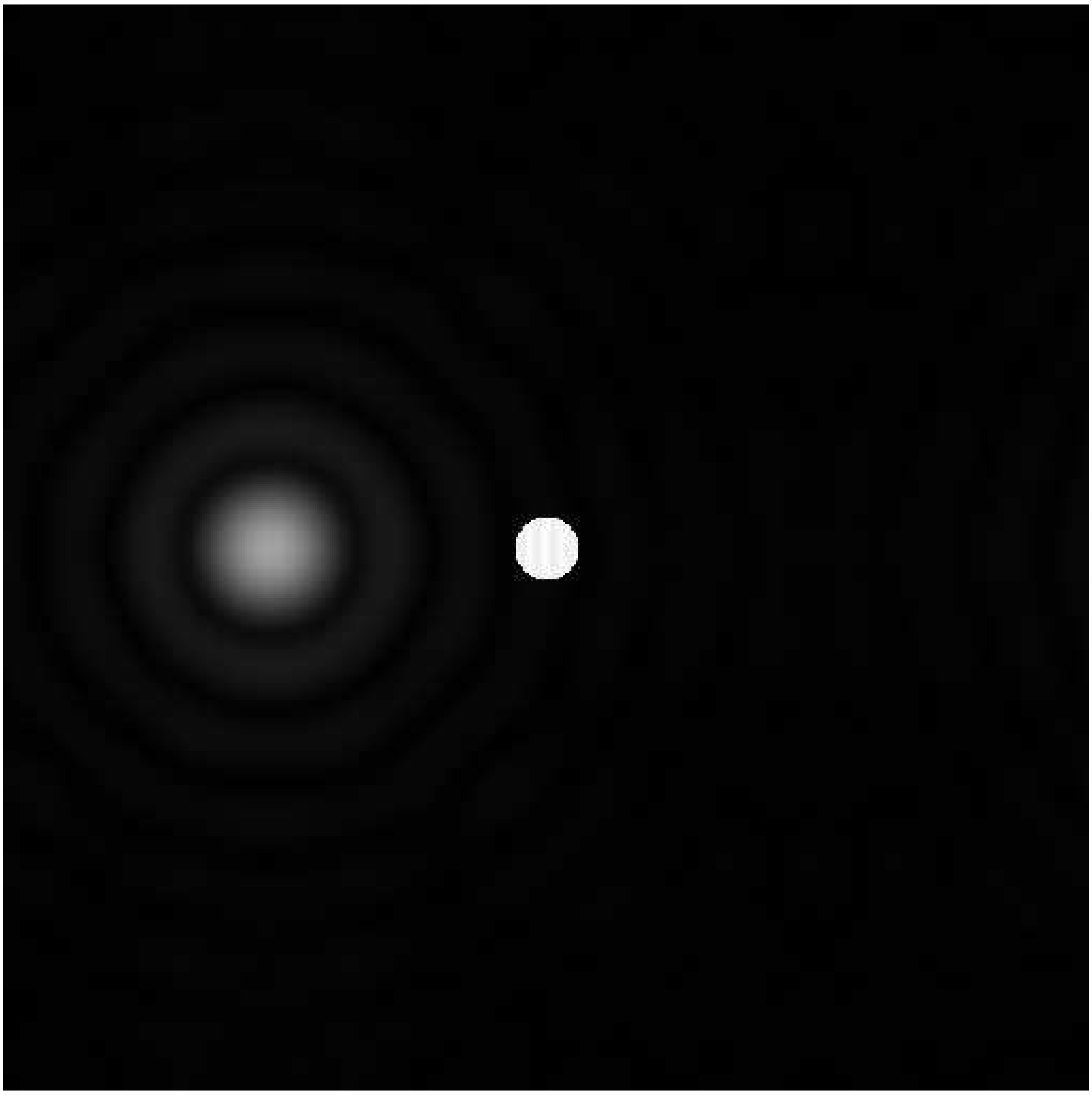

Figure 4.18: Reconstructed object from off-axis hologram shown in Figure 4.17

In the second simulation, the same simple object used in the first simulation is used as the input pattern. The implemented scenario is illustrated in Figure 4.2. In this scenario, we use 2λ sampling period and the distance between the centers of the input and observation plane is 2048λ. Moreover, observation plane has 30° tilt angle around y-axis. The real part of the obtained diffraction pattern is given in Figure 4.21 and the cross-section of it is in Figure 4.22. The magnitude of the diffraction pattern is provided in Figure 4.19. Furthermore, the cross-section of the magnitude part is in Figure 4.20. All the cross-sections are taken along the x-axis and center of the y-axis. The Figure 4.23 provides the off-axis hologram of the object. The Figure 4.24 shows the reconstructed object from the off-axis hologram of the object.

In the third simulation, we use the same simple object as the input of the implemented scenario. The spatial sampling parameter is chosen as 2λ and the distance between the centers of the input and observation plane is taken as 2048λ. In this scenario, the tilt angle of the observation plane around y-axis is 45°. The real part of the obtained diffraction pattern is given in Figure 4.27 and the cross-section of it is in Figure 4.28. The magnitude of the diffraction pattern is provided in Figure 4.25 and the cross-section of the magnitude part is in Figure 4.26. The Figure 4.29 provides the off-axis hologram of the object. The reconstructed object can be seen in Figure 4.30 from the off-axis hologram of the object.

In the fourth simulation all the parameters are the same as the previous simulation except the tilt angle. The tilt angle is chosen as 60°. The real part of the diffraction pattern is given in Figure 4.33 and the cross-section of it is in Figure 4.34. The magnitude of the diffraction pattern is provided in Figure 4.31 and the cross-section of the magnitude part is in Figure 4.32. The Figure 4.35 provides the off-axis hologram of the object. Also, the reconstructed object can be seen in Figure 4.36 from the off-axis hologram of the object.

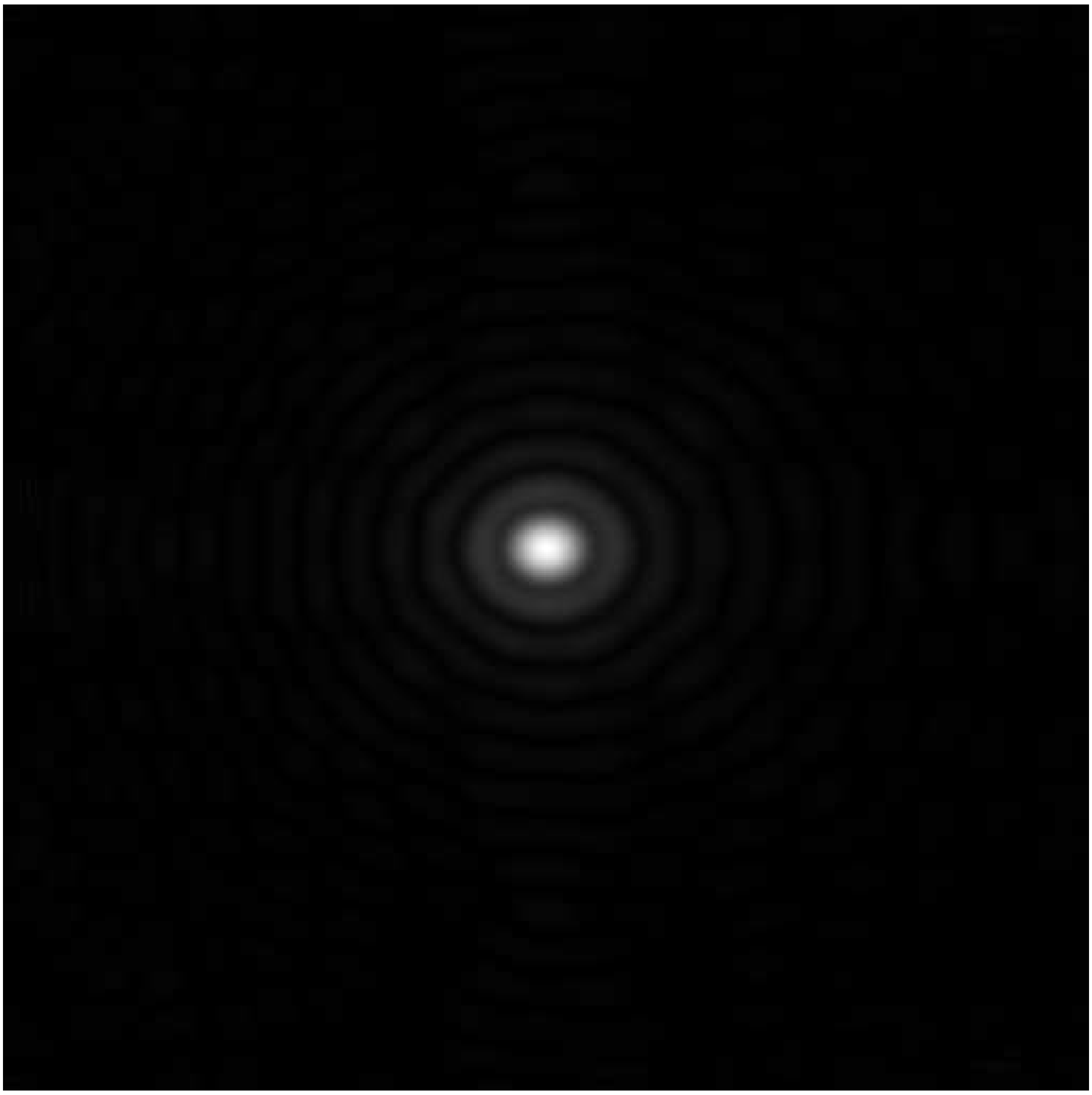

Figure 4.19: Magnitude of the diffraction pattern corresponds to the input pattern shown in Figure 4.6

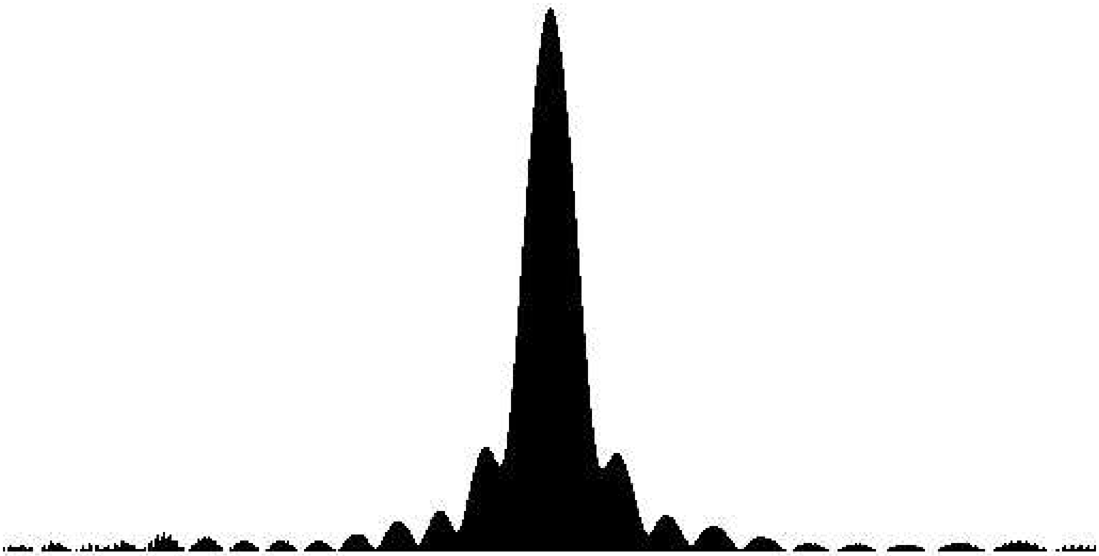

Figure 4.20: Cross-section at center of magnitude of the diffraction pattern shown in Figure 4.19

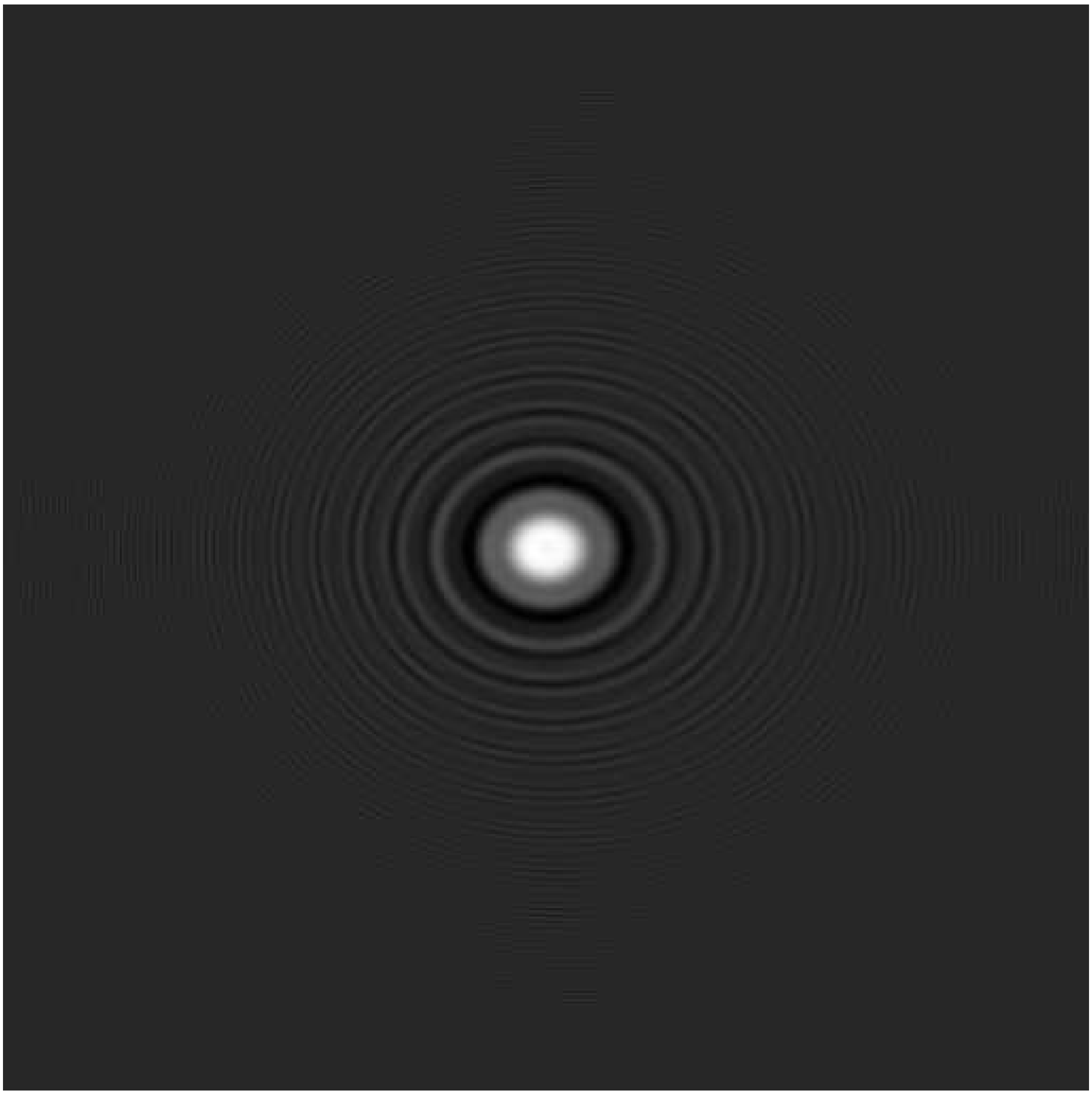

Figure 4.21: Real part of the diffraction pattern corresponds to the input pattern shown in Figure 4.6

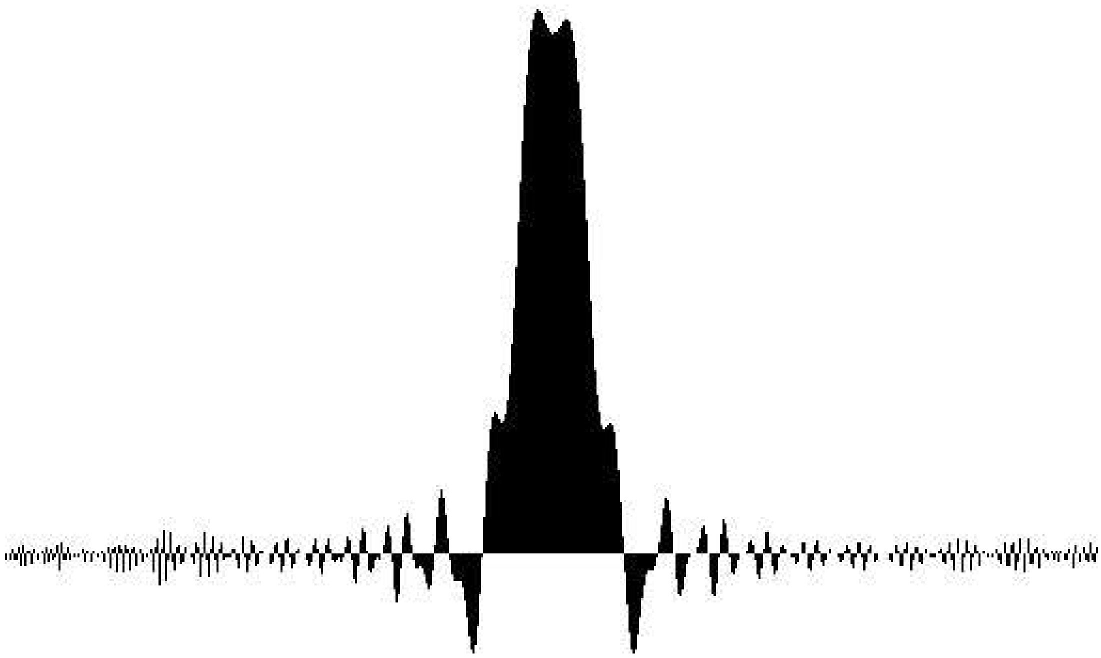

Figure 4.22: Cross-section at center of real part of the diffraction pattern shown in Figure 4.21

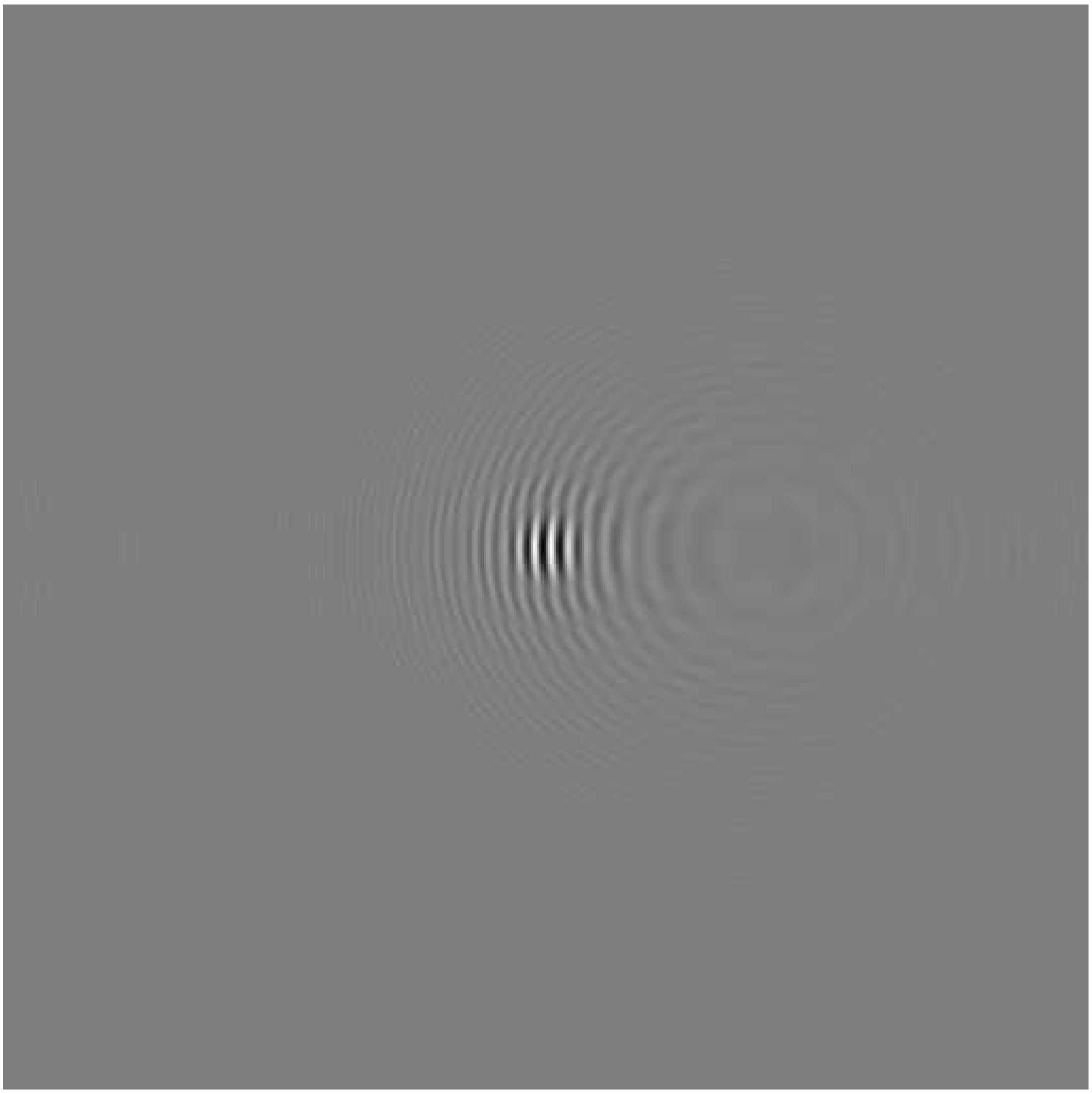

Figure 4.23: Off-axis hologram of the object shown in Figure 4.6

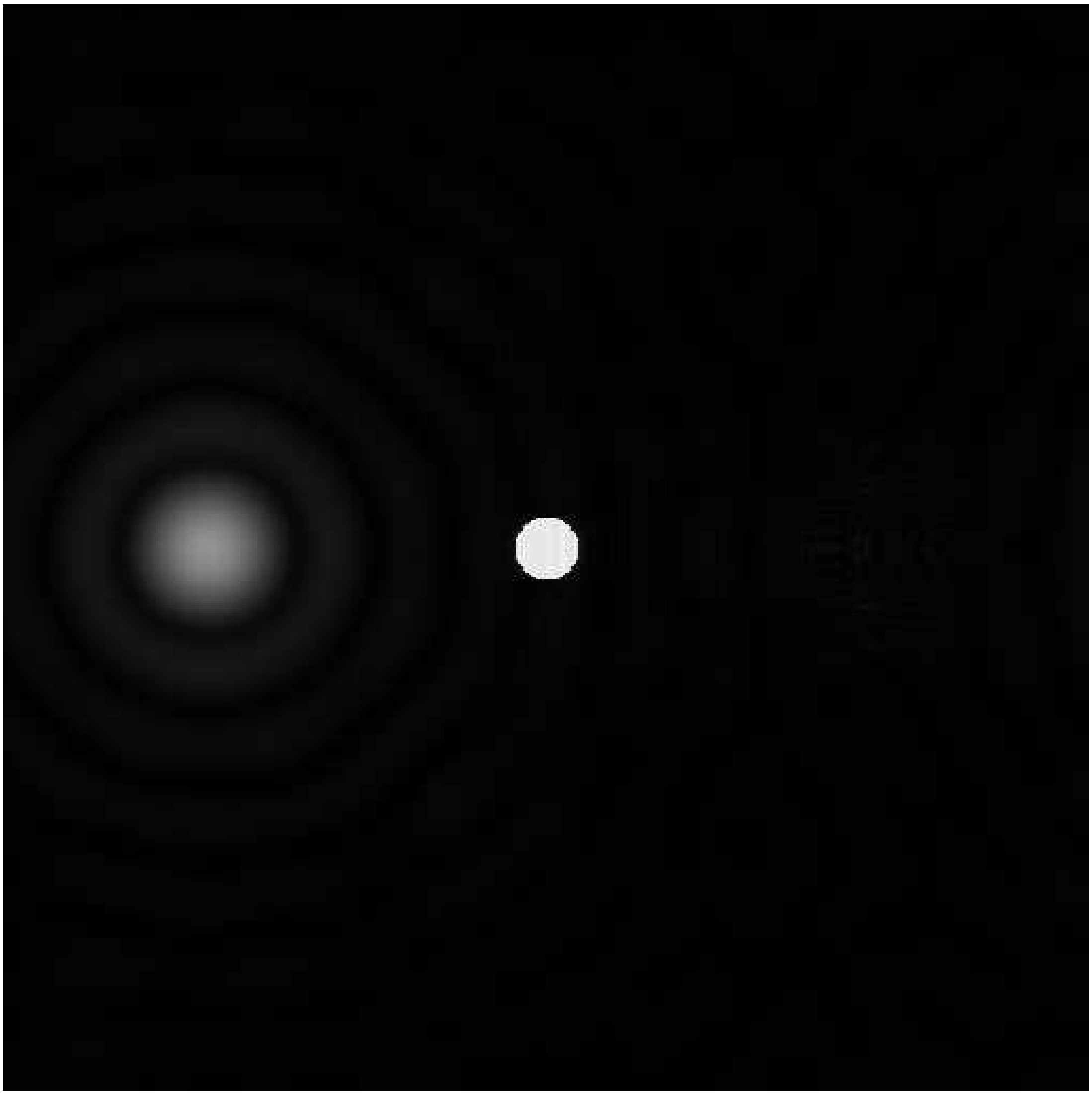

Figure 4.24: Reconstructed object from off-axis hologram shown in Figure 4.23

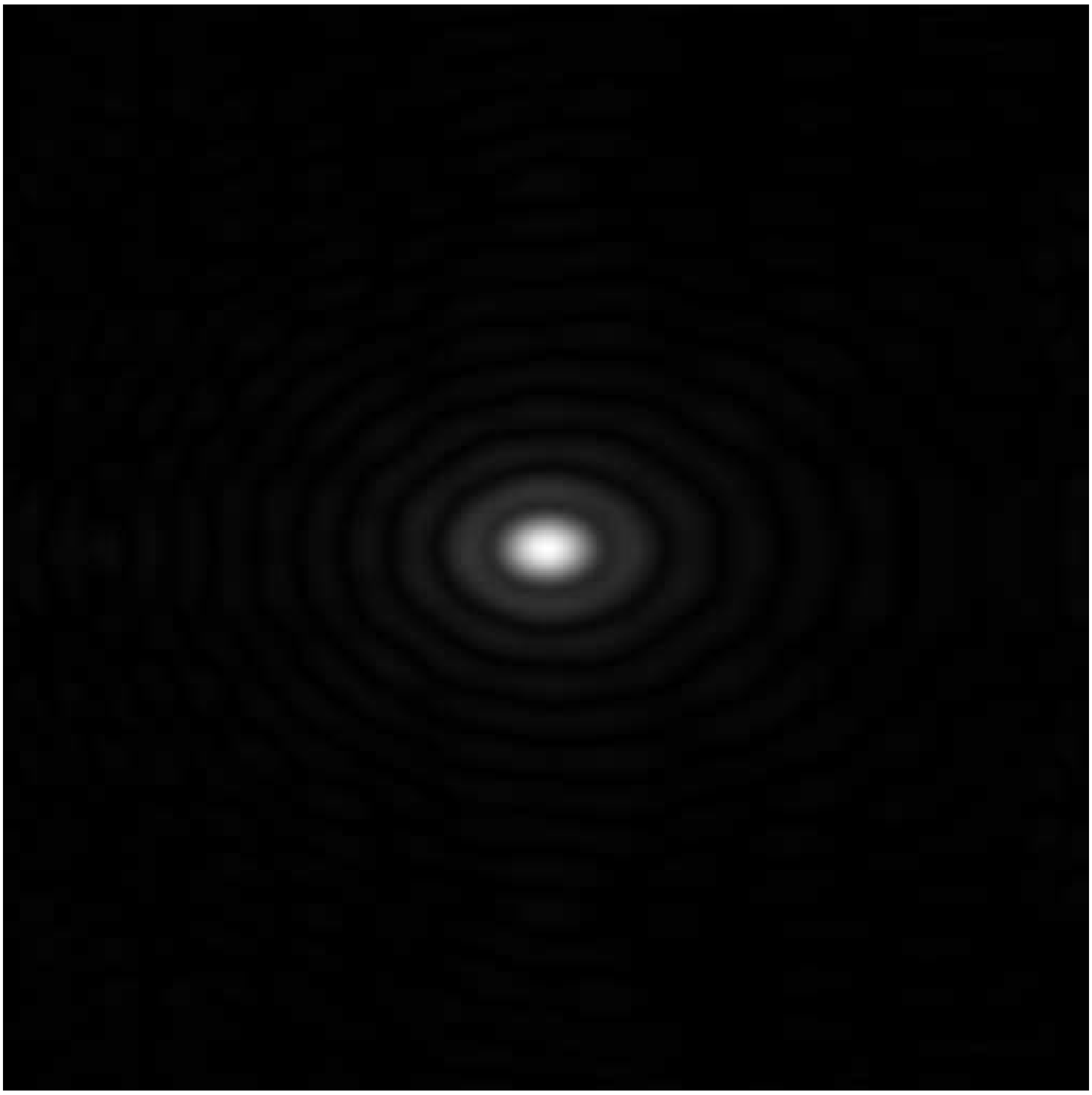

Figure 4.25: Magnitude of the diffraction pattern corresponds to the input pattern shown in Figure 4.6

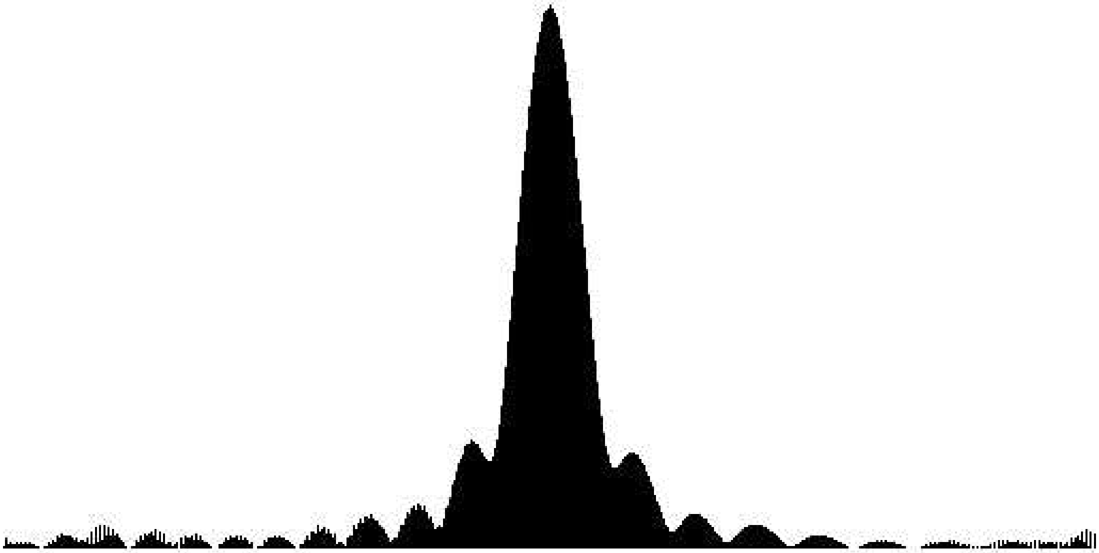

Figure 4.26: Cross-section at center of magnitude of the diffraction pattern shown in Figure 4.25

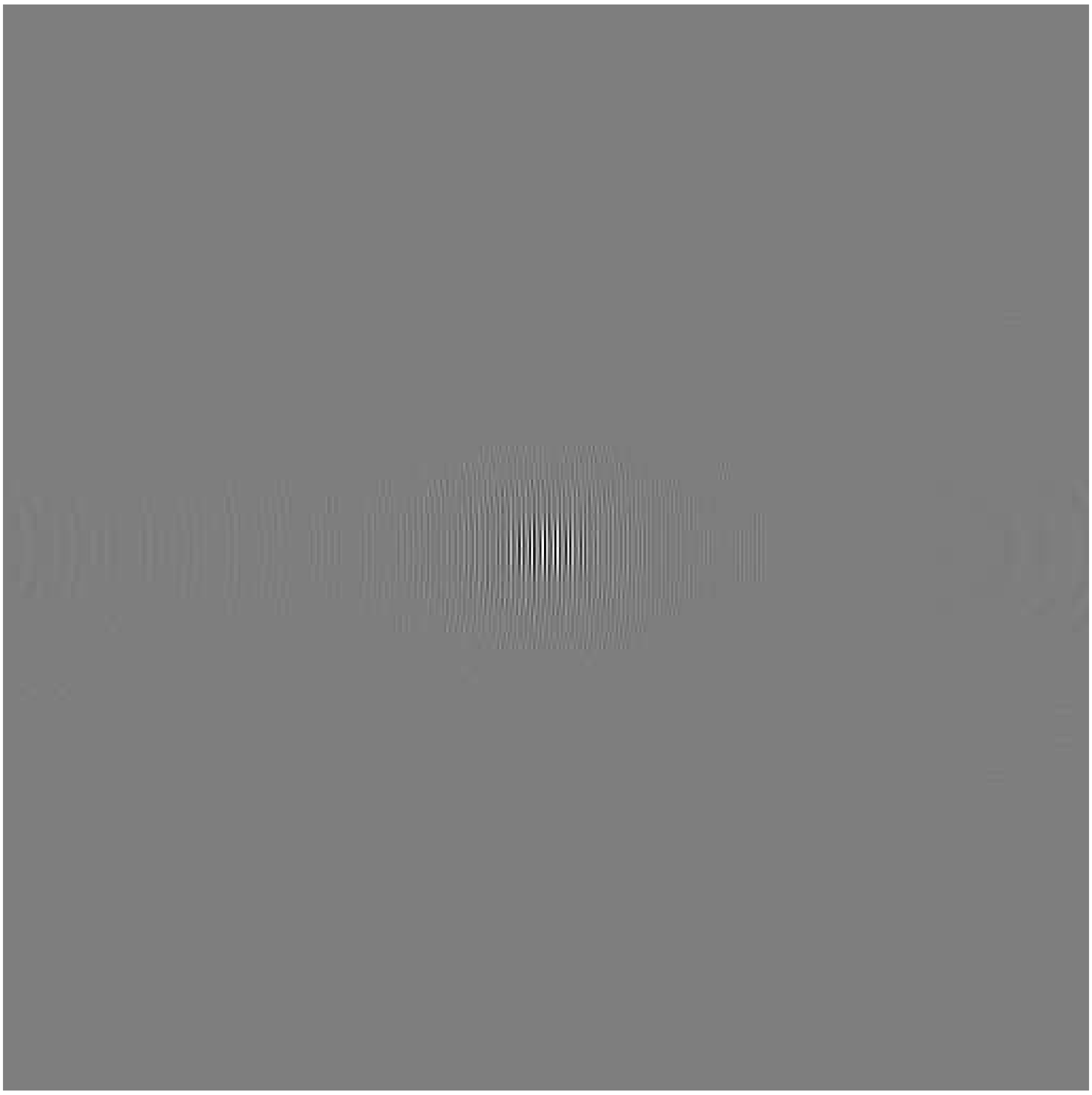

Figure 4.27: Real part of the diffraction pattern corresponds to the input pattern shown in Figure 4.6

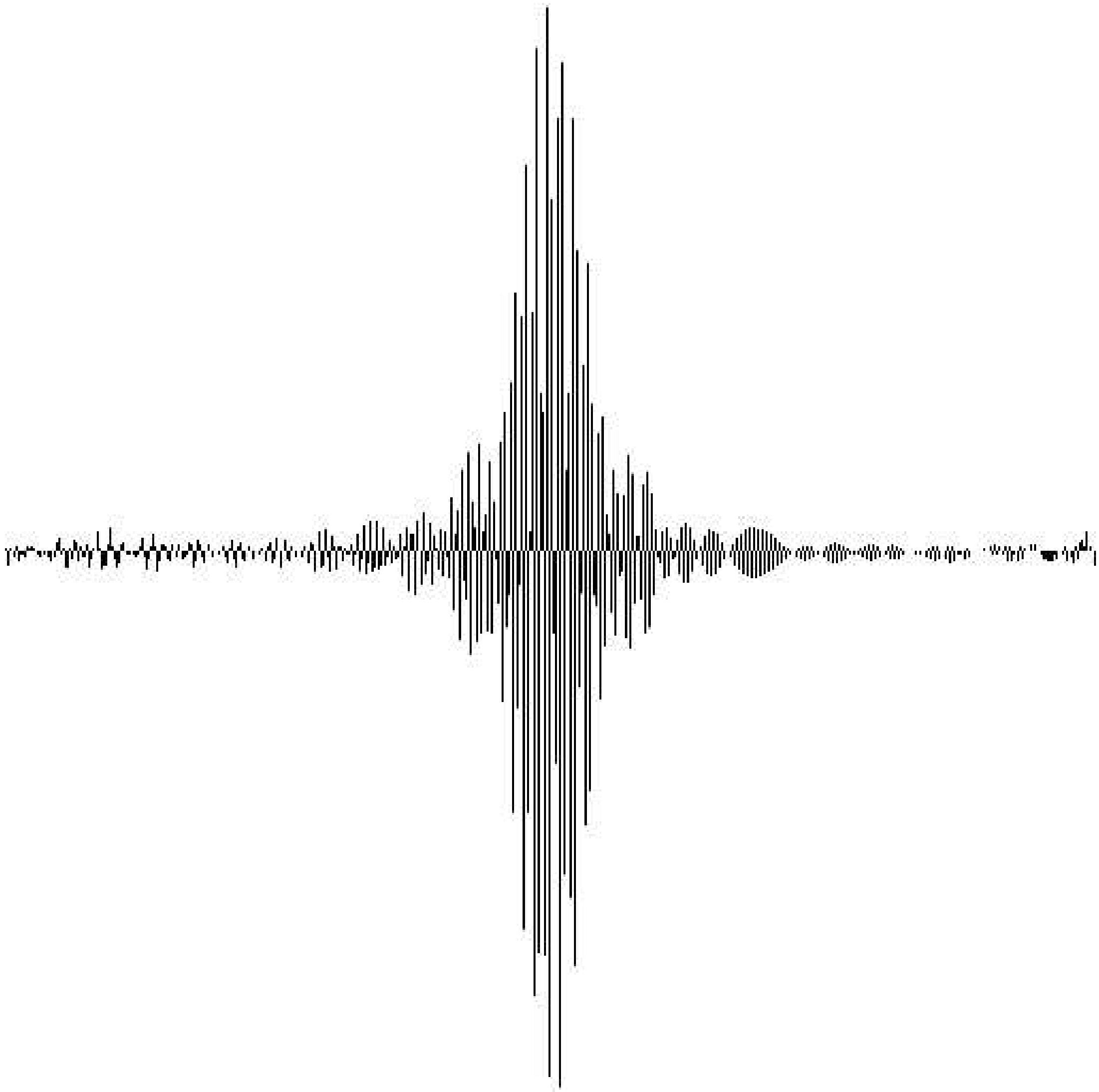

Figure 4.28: Cross-section at center of real of the diffraction pattern shown in Figure 4.27

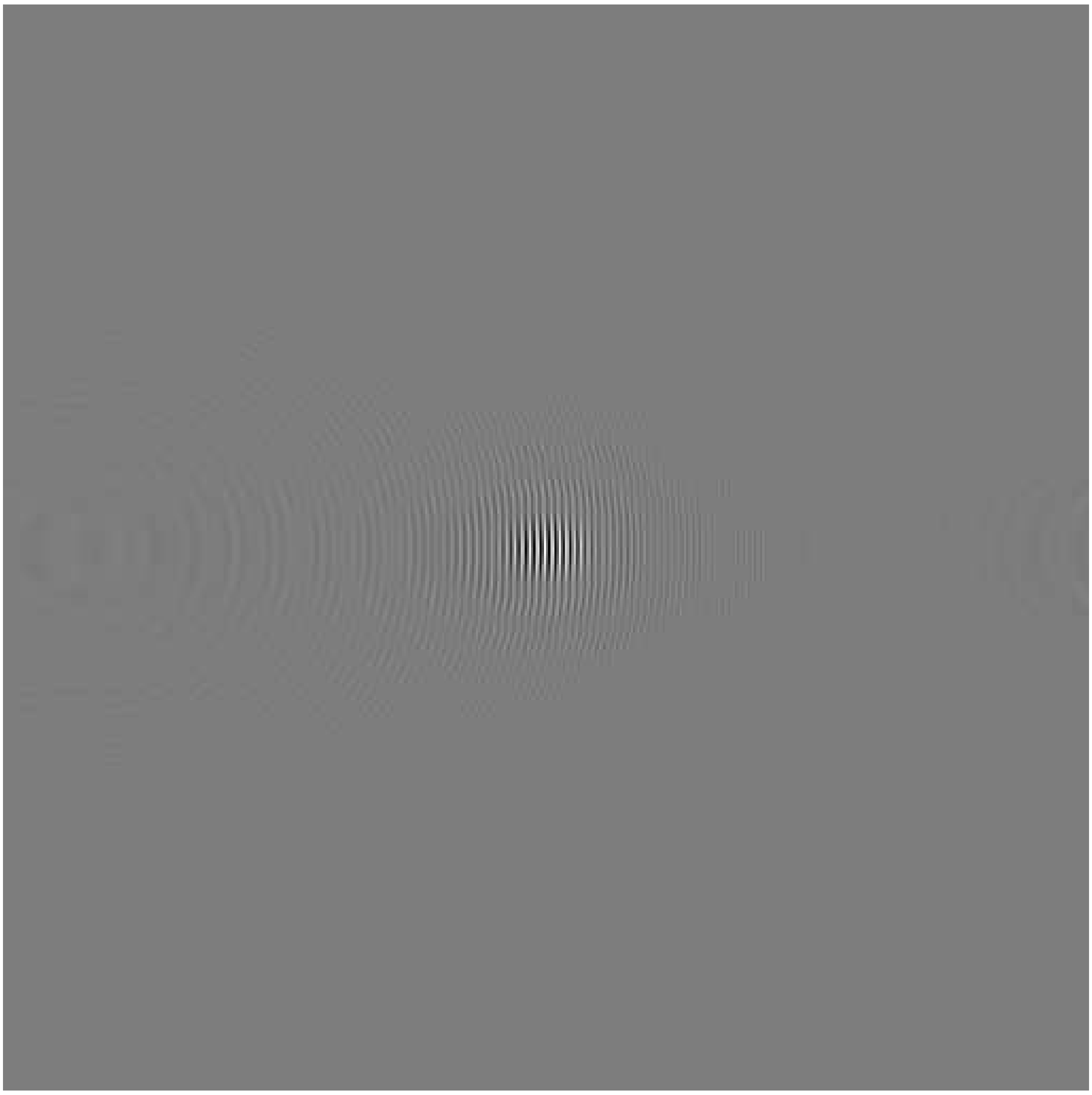

Figure 4.29: Off-axis hologram of the object shown in Figure 4.6

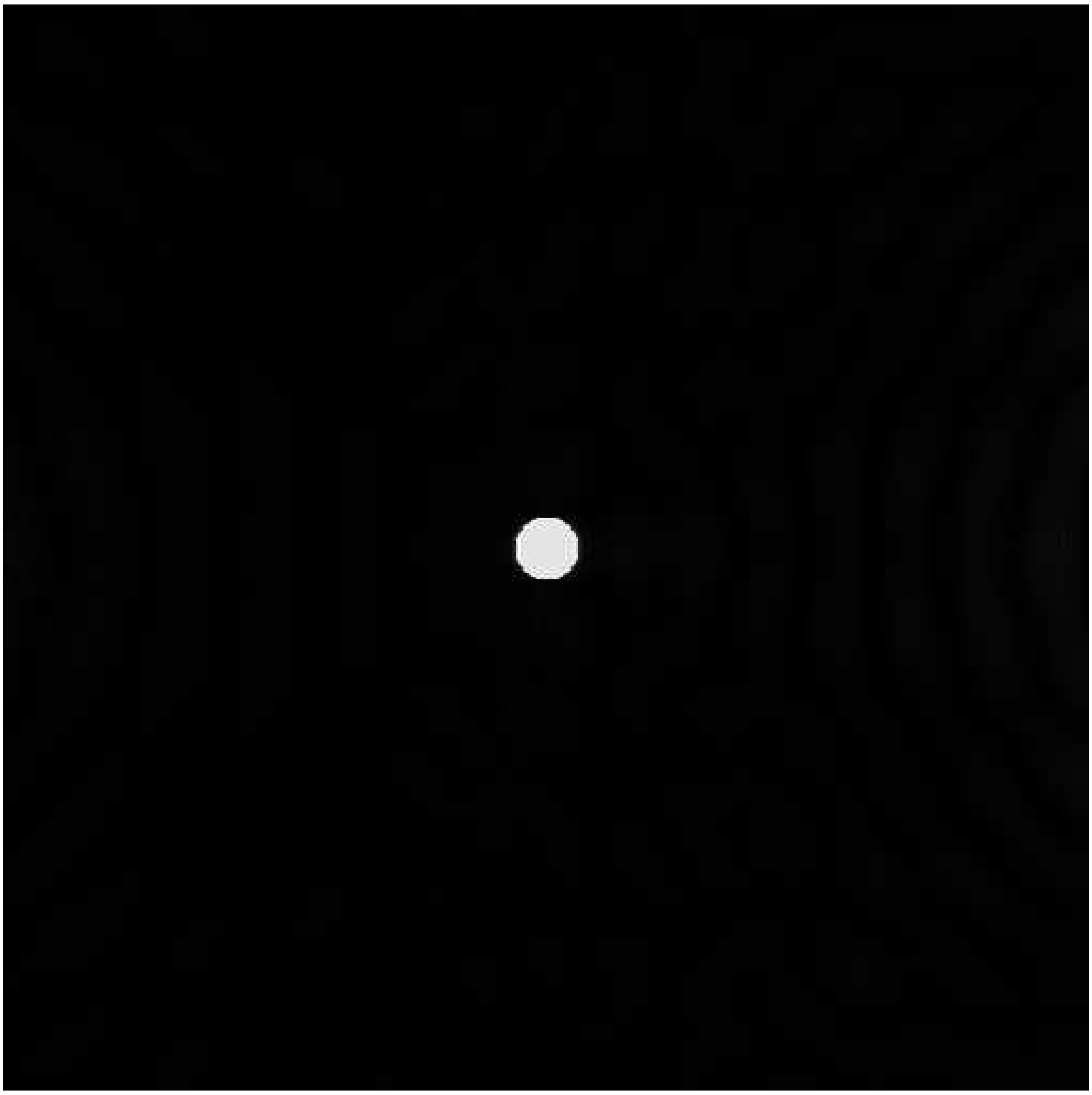

Figure 4.30: Reconstructed object from off-axis hologram shown in Figure 4.29

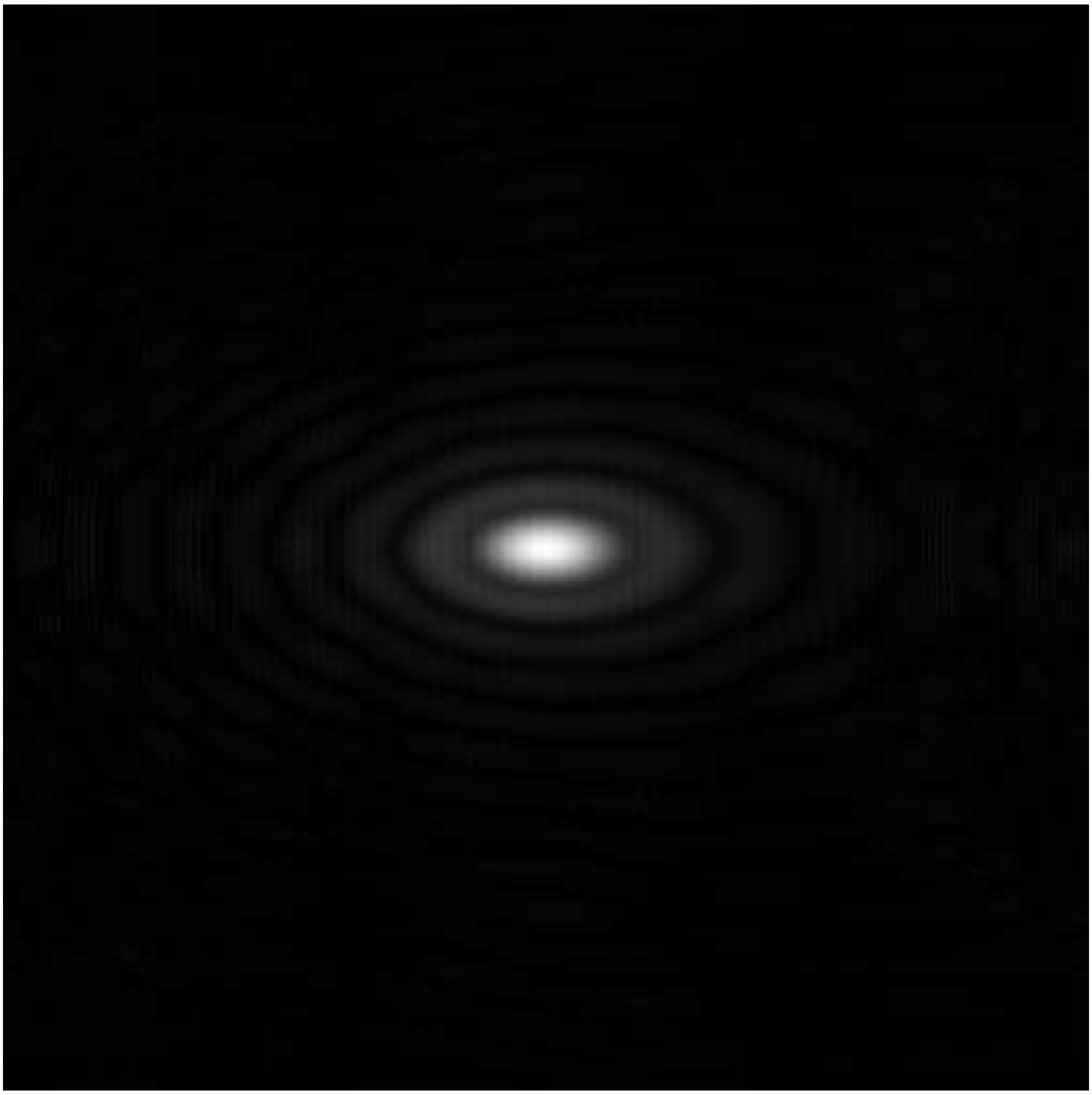

Figure 4.31: Magnitude part of the diffraction pattern corresponds to the input pattern shown in Figure 4.6

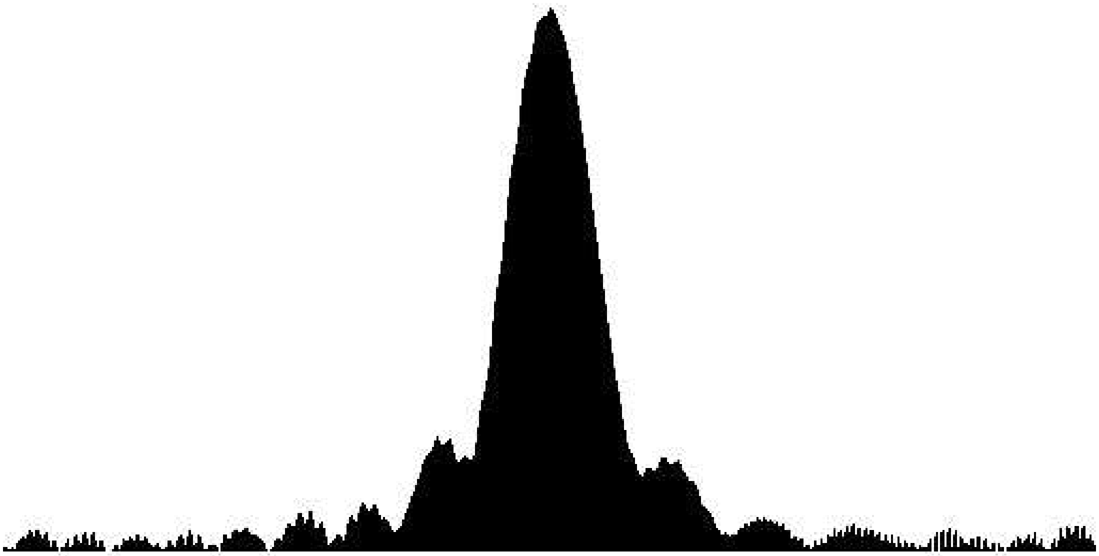

Figure 4.32: Cross-section at center of magnitude of the diffraction pattern shown in Figure 4.31

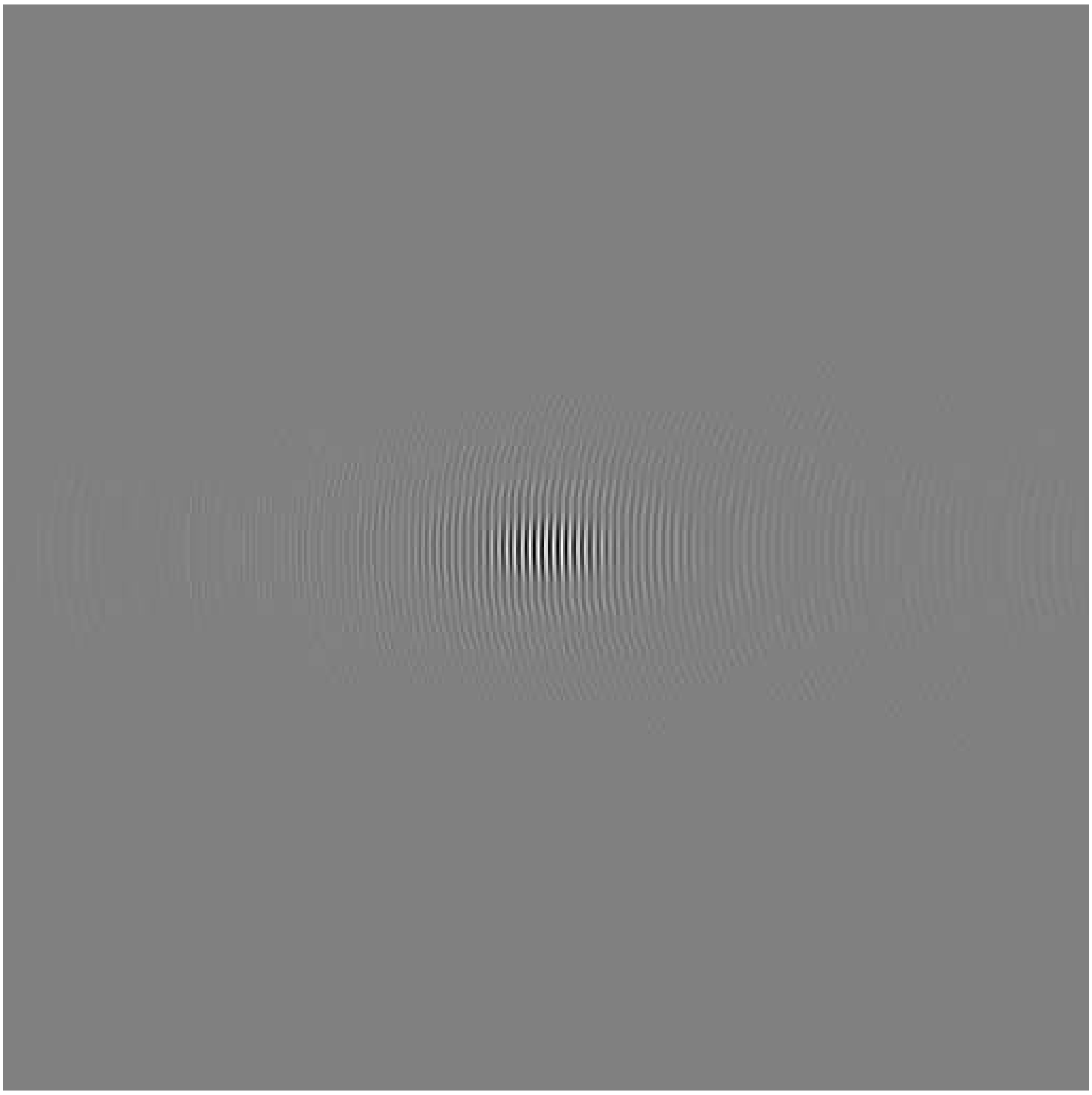

Figure 4.33: Real part of the diffraction pattern corresponds to the input pattern shown in Figure 4.6

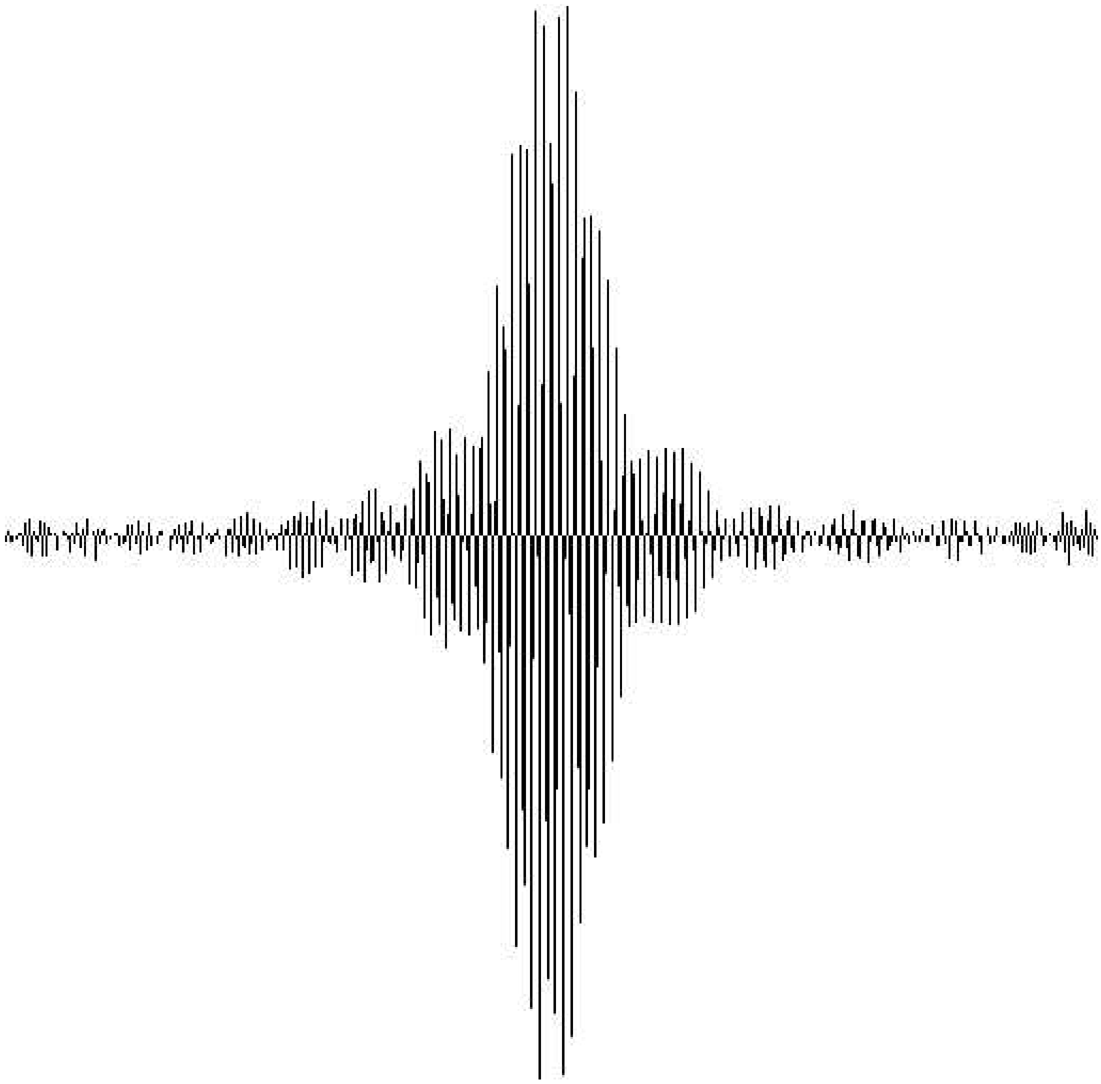

Figure 4.34: Cross-section at center of real of the diffraction pattern shown in Figure 4.33

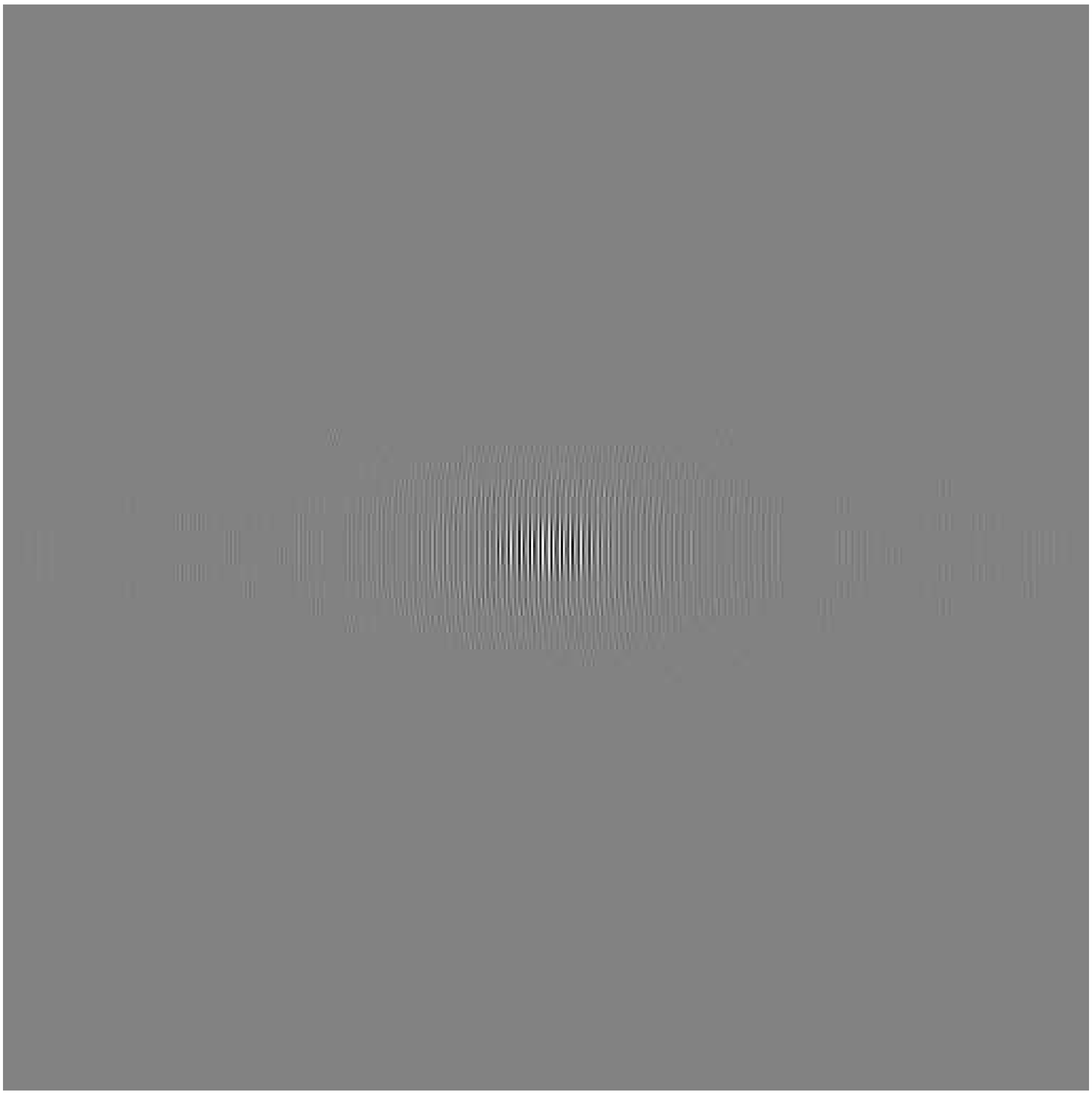

Figure 4.35: Off-axis hologram of the object shown in Figure 4.6

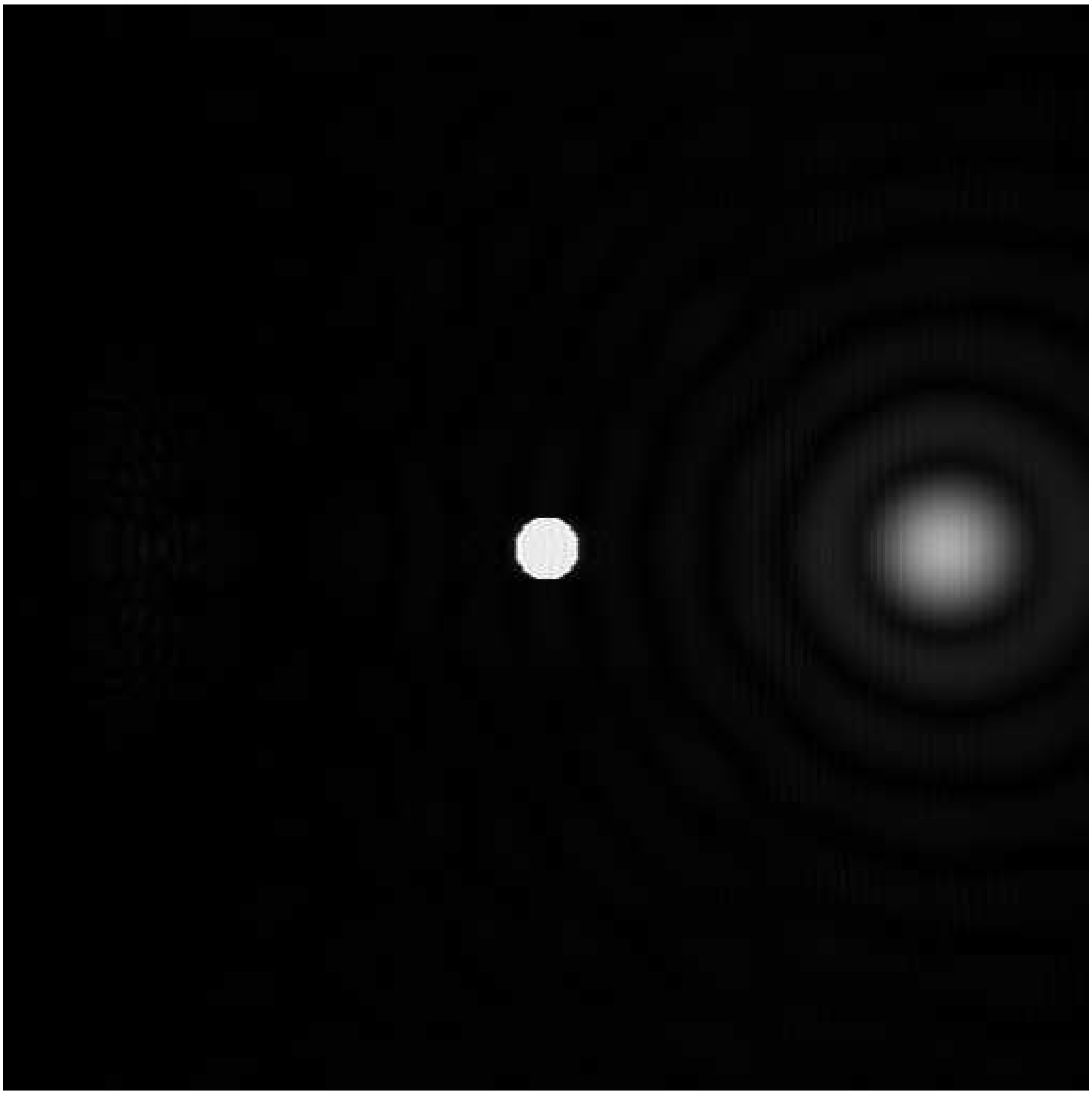

Figure 4.36: Reconstructed object from off-axis hologram shown in Figure 4.35

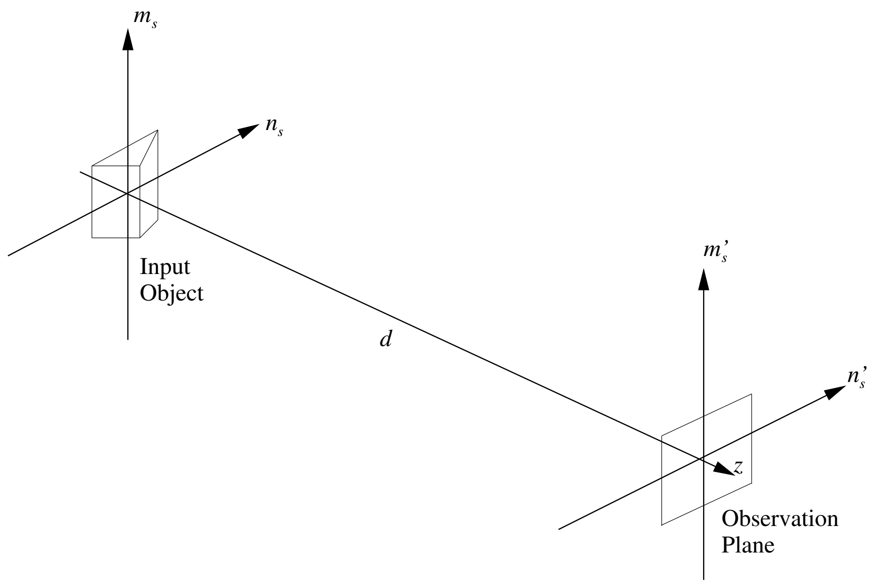

Figure 4.37: Illustration of the fifth scenario

In the fifth simulation an object is obtained by combining several planes. The illustration of the implemented scenario is given in Figure 4.37. The diffraction pattern of the three-dimensional object is computed. The sampling period is 2λ as in the previous simulations. The distance between center of the object and the observation plane is taken as 2048λ.

In the sixth simulation an object is built by using 2 planes and each plane is made up by 2 faces. The generated object can be seen from Figure 4.44. The illustration of the sixth scenario is given in Figure 4.43. The sampling period is 2λ as in the previous simulations and the distance between the center of the object and the observation plane is taken as 2048λ. Figure 4.45 provides the off-axis hologram of the object in Figure 4.44. Figures 4.46 and 4.47 give the reconstructed planes that form the object.

4.5 Discussion and Conclusions

In this chapter, plane wave spectrum model and simulator based on the model are presented. The model depends on the Rayleigh-Sommerfeld diffraction integral to

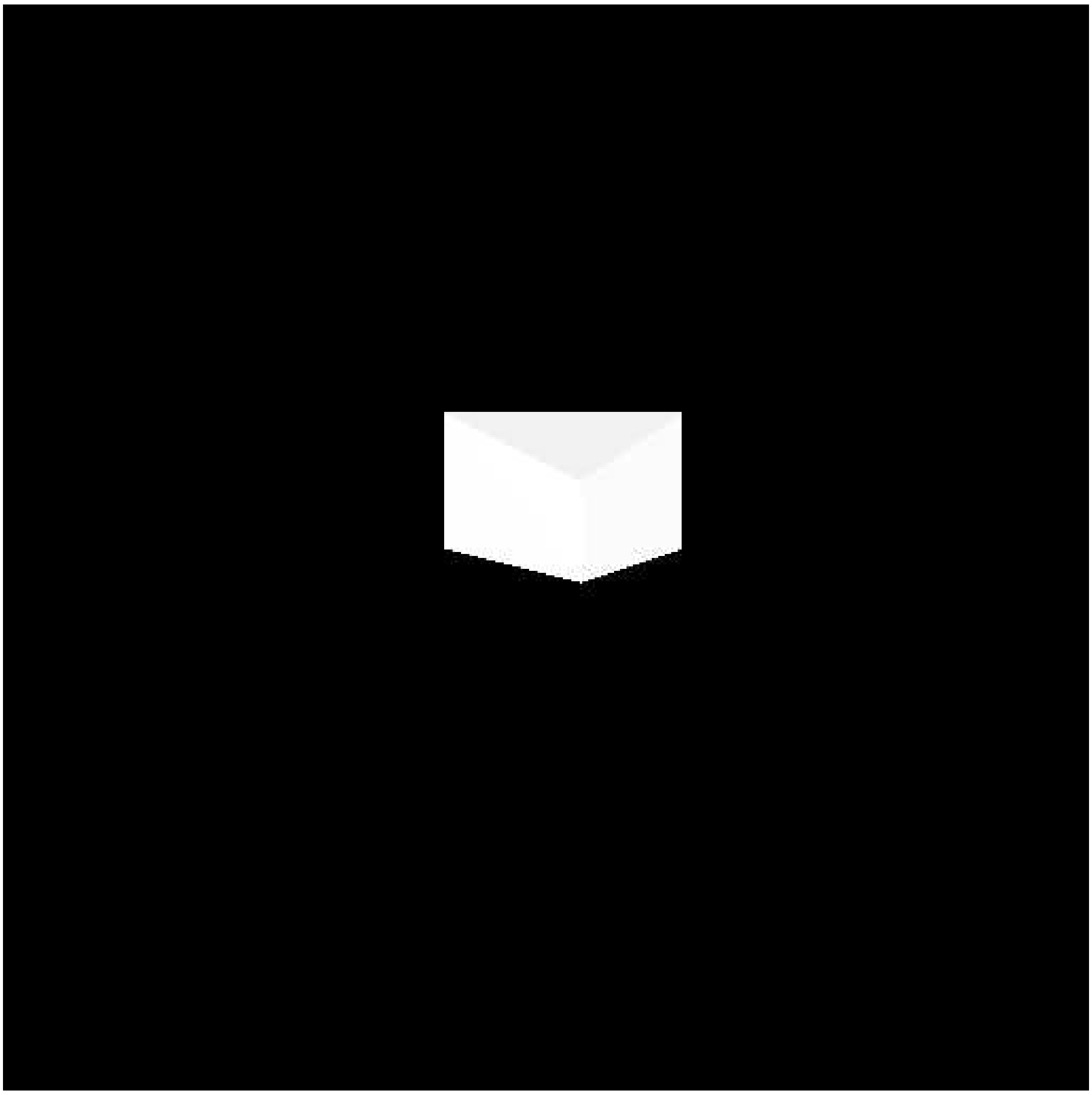

Figure 4.38: An input object

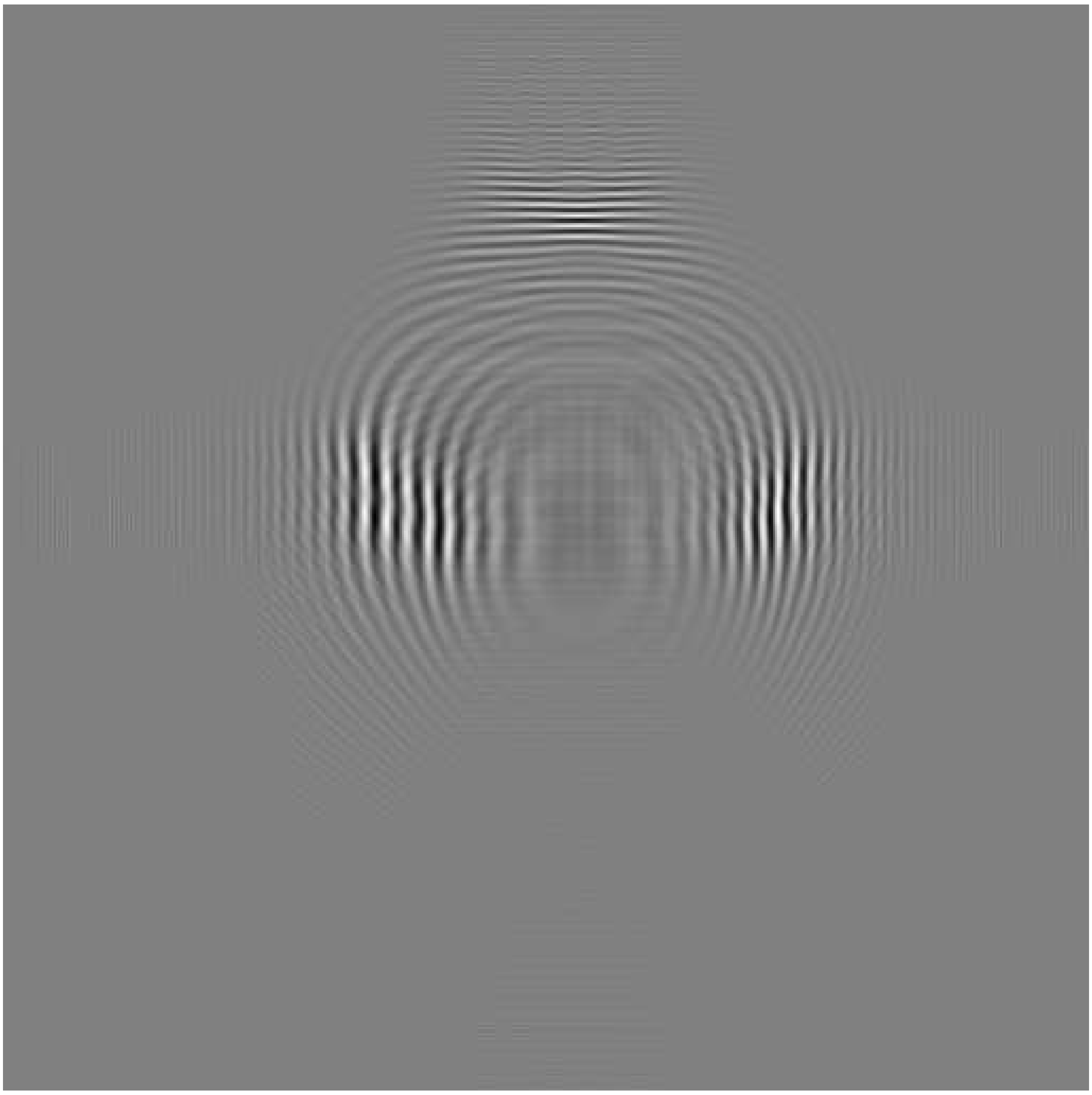

Figure 4.39: Real part of the diffraction pattern of the object shown in Figure 4.38

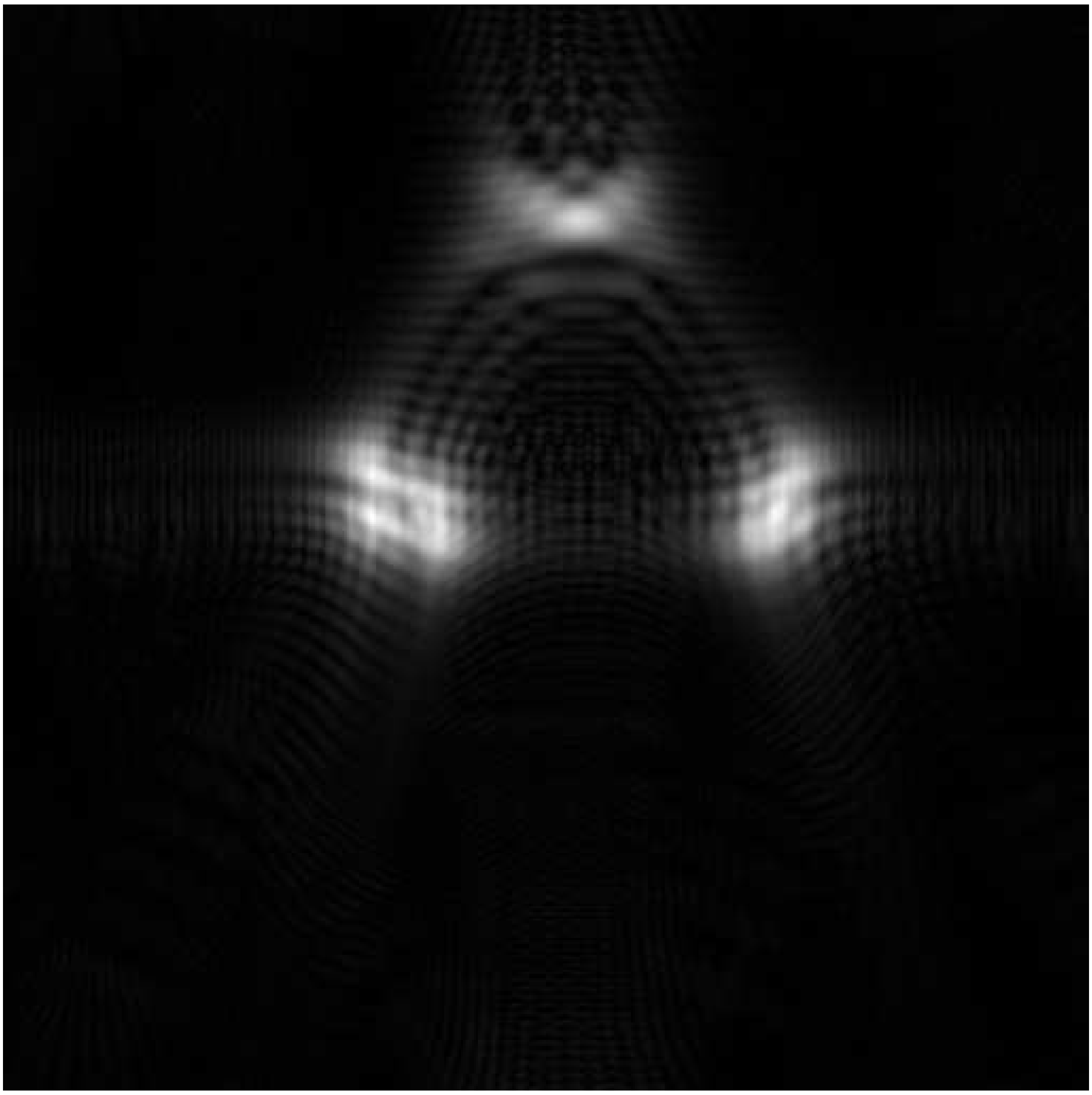

Figure 4.40: Magnitude of the diffraction pattern of the object shown in Figure 4.38

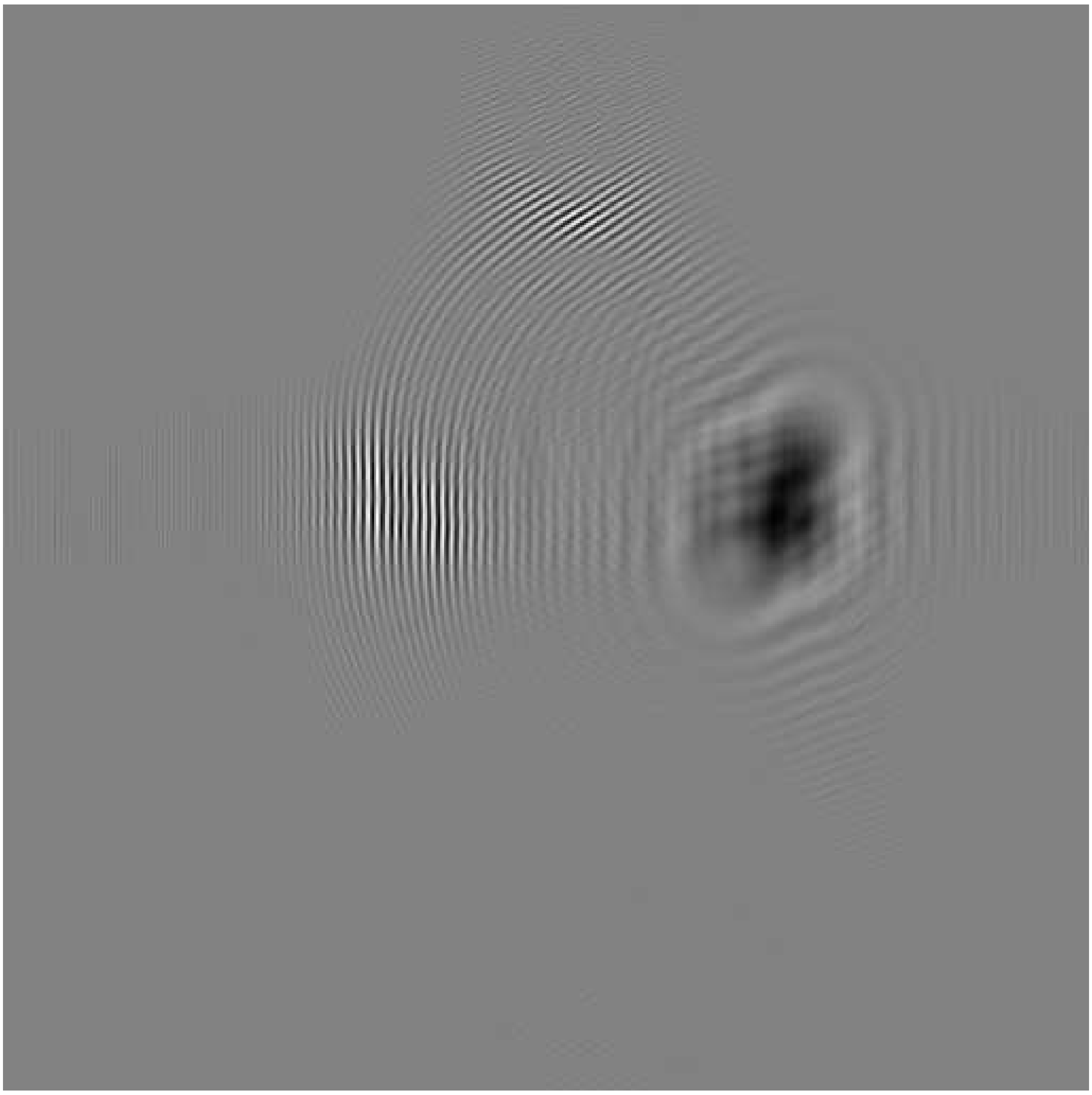

Figure 4.41: Off-axis hologram of the object shown in Figure 4.38

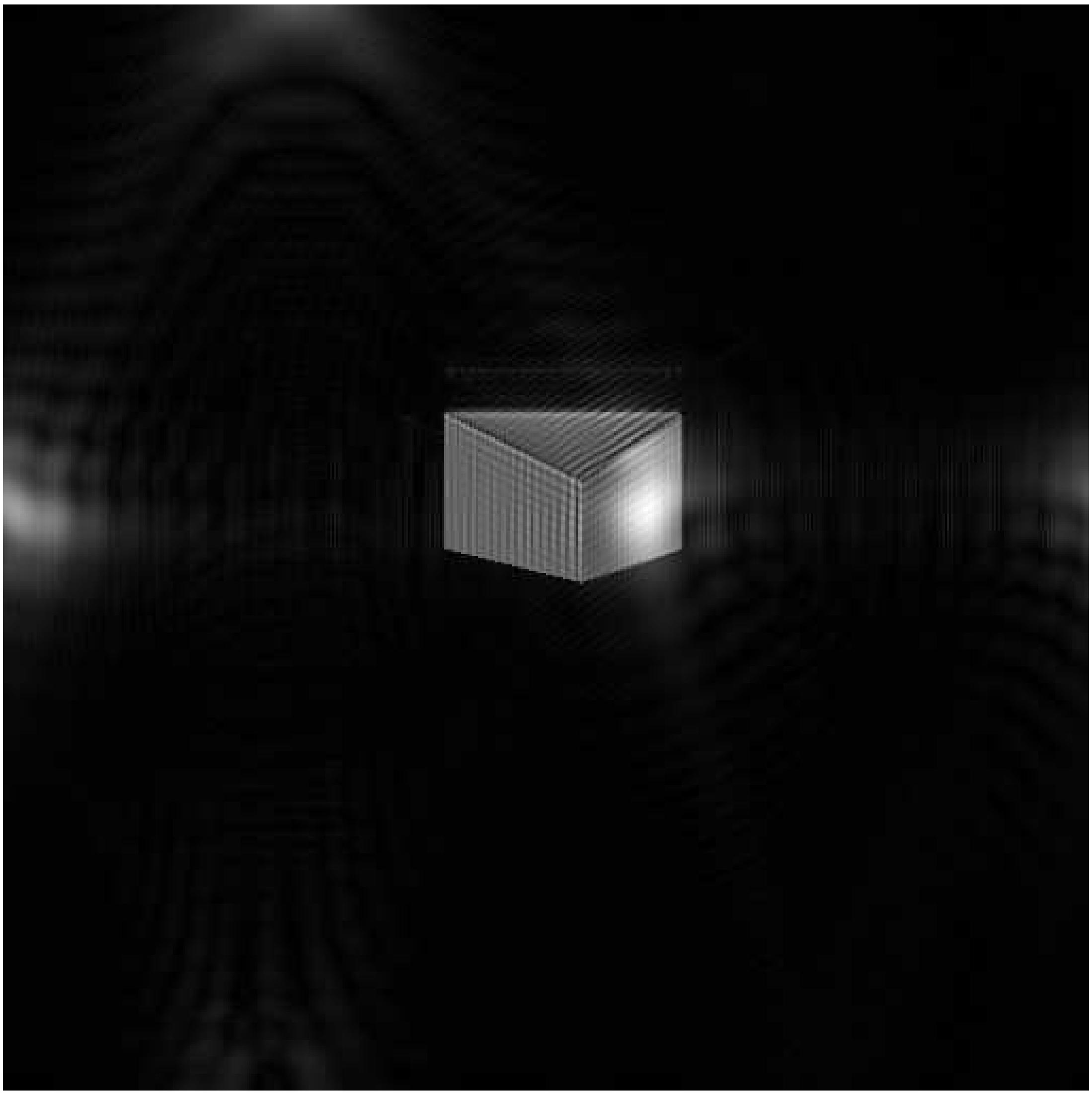

Figure 4.42: Reconstructed object from the Figure 4.41

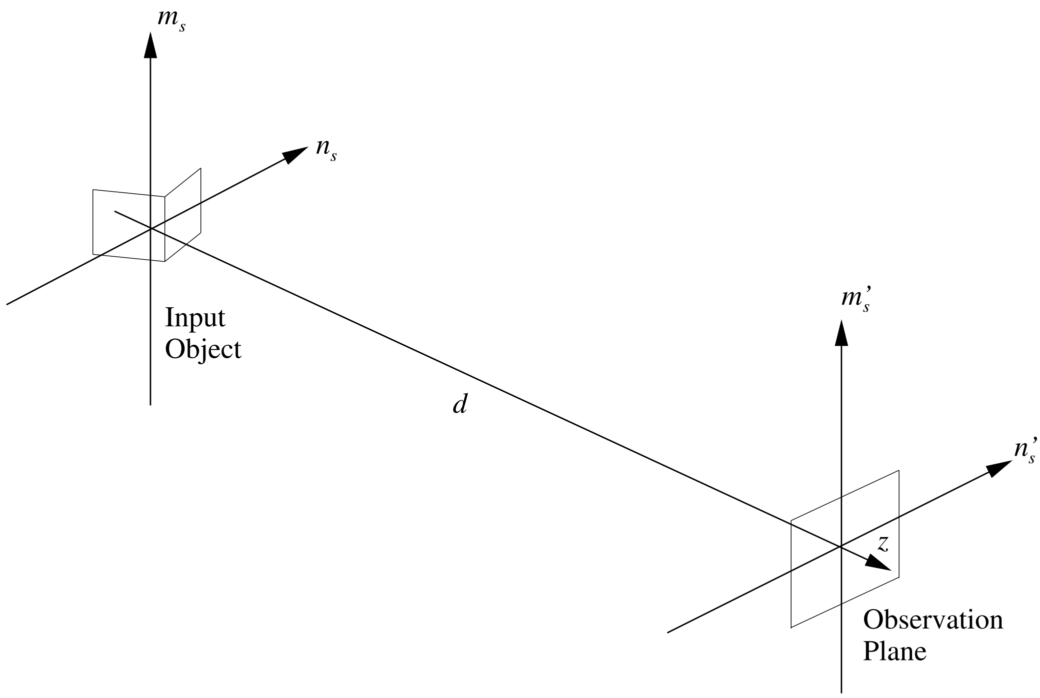

Figure 4.43: Illustration of the fifth scenario

compute the diffraction pattern of an object. Therefore the model does not need Fresnel or Fraunhofer approximations. Also, the model provides fast calculation of the diffraction pattern between the input and observation planes, because of using DFT, IDFT and the Fourier transform of the kernel, we can simulate only the periodic input and diffraction patterns.

In the first simulation, the simple object which is used in the previous chapter is taken as the input pattern. The diameter of the circle is 0.0188 m. Figure 4.6 represents the input field. The observation plane is located 340 m away from the input plane and it is parallel to the input plane, because of having parallel planes the real part of the diffraction pattern given in Figure 4.13 and the magnitude of the diffraction pattern given in Figure 4.15 are symmetric. Moreover, the symmetry can also be seen from Figures 4.14 and 4.16. The obtained results look pretty much the same as the results obtained by using the pointwise simulator.

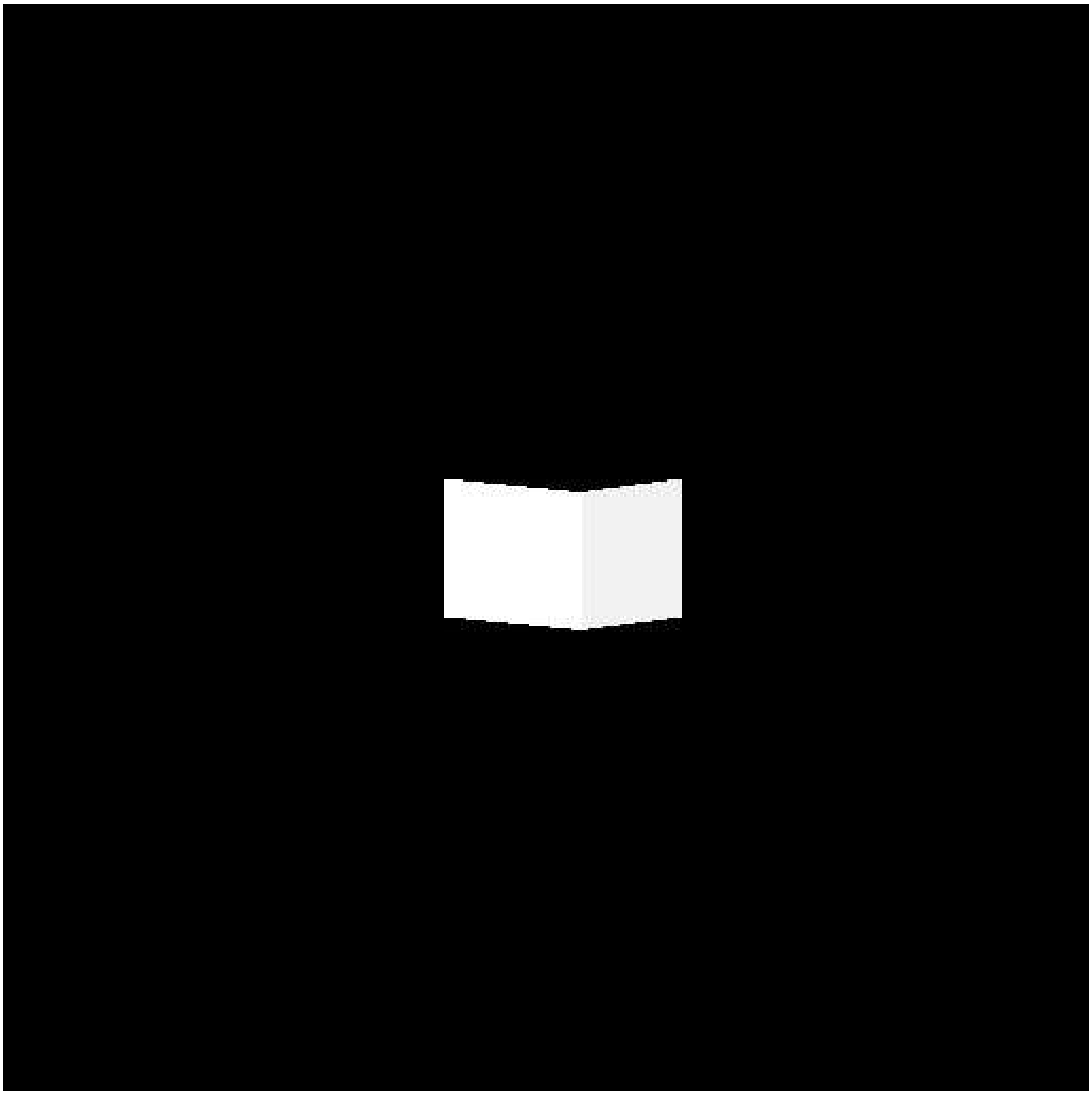

Figure 4.44: An input object

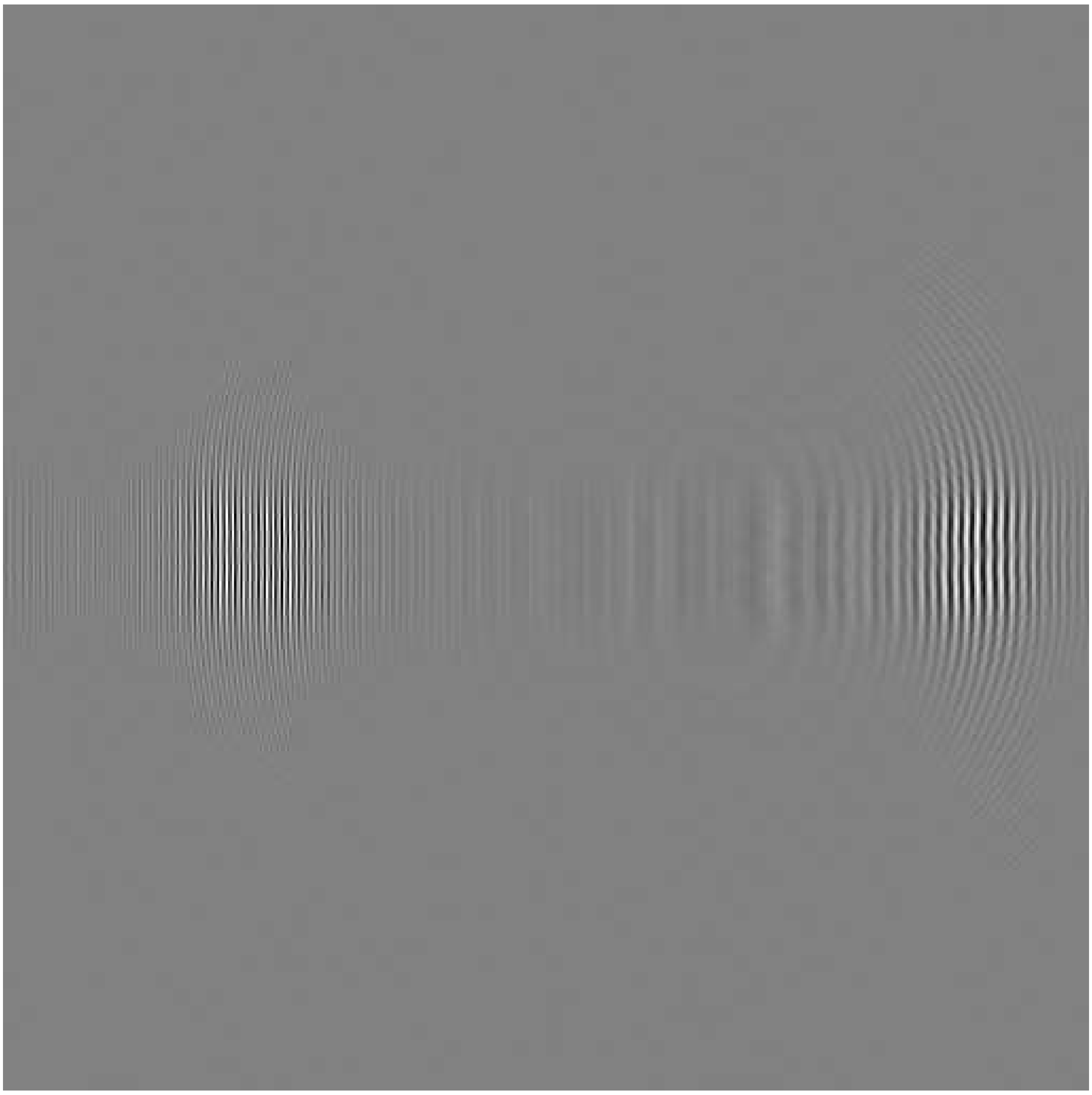

Figure 4.45: Off-axis hologram of the object shown in Figure 4.44

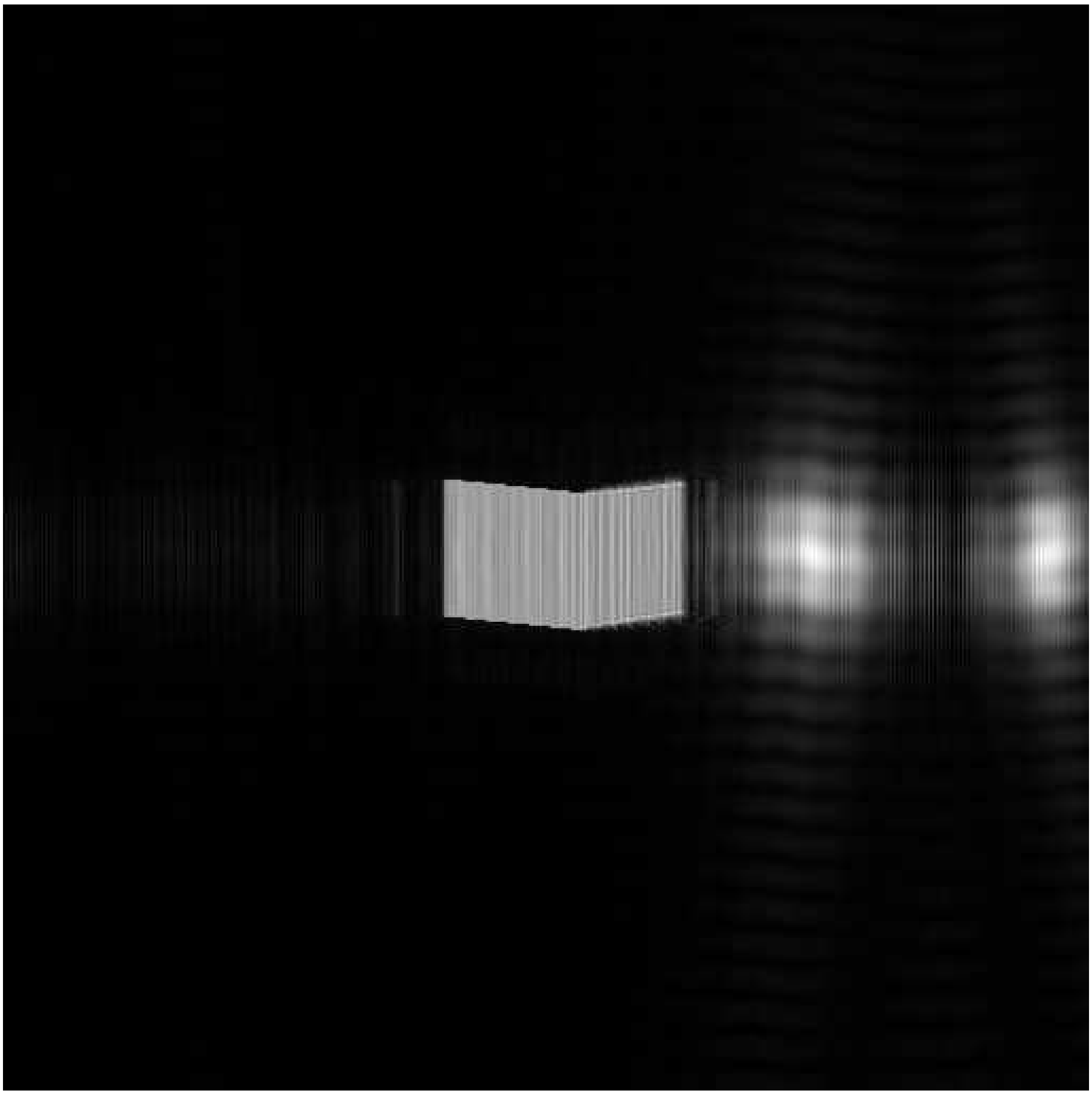

Figure 4.46: Reconstructed left plane of the object which can be seen from the Figure 4.45

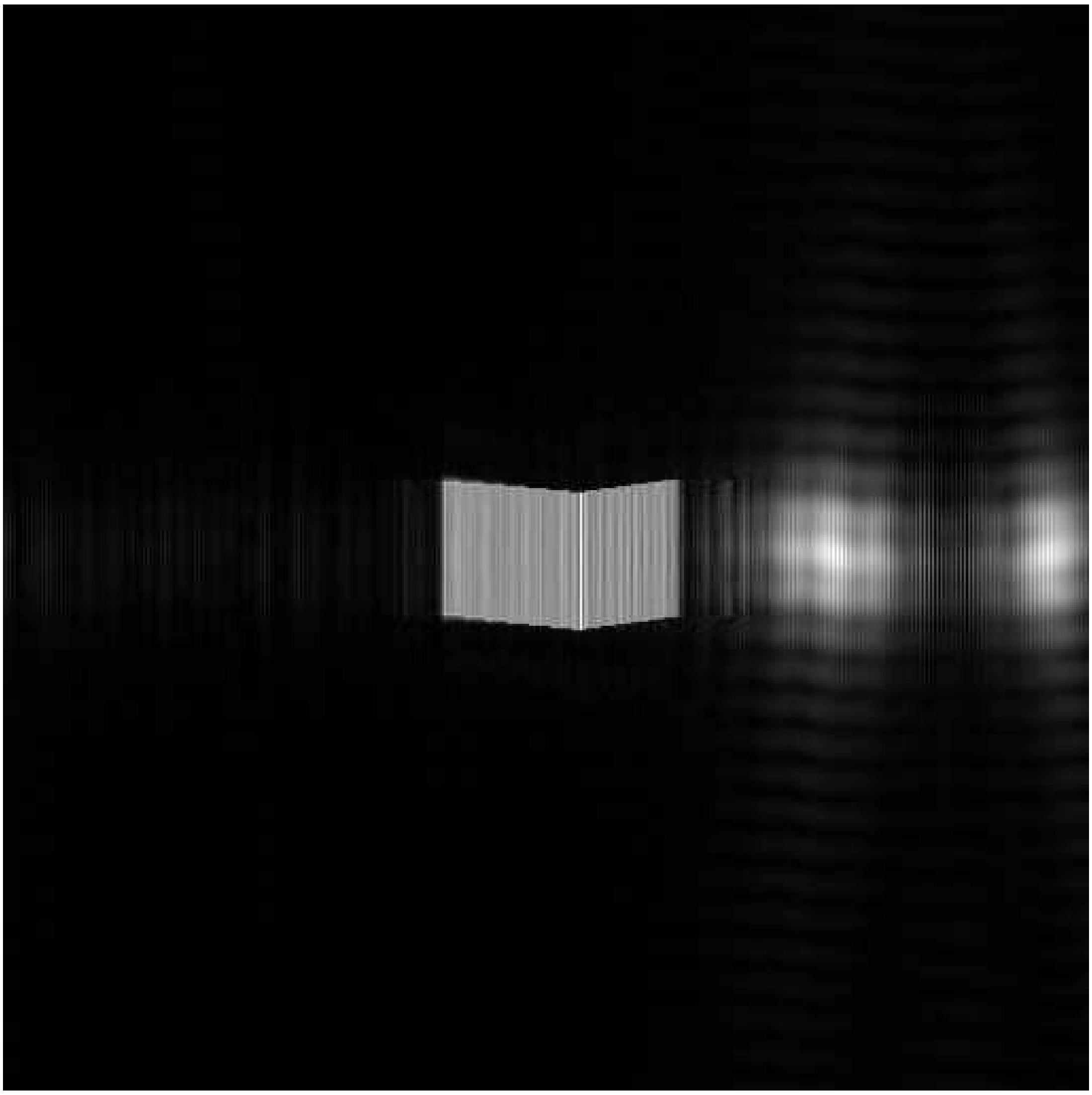

Figure 4.47: Reconstructed right plane of the object which can be seen from the Figure 4.45

In the second, third and fourth simulations, the sampling period is chosen as 1.27 μm, so the diameter of the object is 38 μm. The observation plane is 1.30 mm away from the input plane. We prefer to compute the diffraction pattern close to the input pattern because the effect of having tilt around y-axis can be seen easily in the Figures 4.19, 4.20, 4.25, 4.26, 4.31 and 4.32. The magnitude of the diffraction pattern looks like an ellipse. This is a result of having tilt around y-axis. Also, the fringes at the right side of the diffraction pattern is larger than the fringes at the left side, because the larger fringes provides the further side of the observation plane to input plane and the shorter fringes represents the closer side of the observation plane to input plane. In the second simulation, observation plane has 30° tilt angle around the y-axis. It can be seen from the Figure 4.20 that the diffraction pattern is distorted by the periodic replica of the diffraction pattern. The distortion is effective at the left and right side of the diffraction pattern. The distortion due to the periodic replicas of the diffraction pattern increases if the tilt angle is chosen to be larger and it can be seen in the Figures 4.26, 4.32.

In the fifth simulation, a 3-D object is constructed by using planar faces. We use the scalar optical diffraction model presented in this thesis to obtain the diffraction pattern of the object. The diffraction pattern of the patches can affect each other. Therefore, the light distribution of each patch is distorted. Moreover the twin-image causes some distortion on the light distribution of the patches.

In the sixth simulation, another simple 3-D object is generated by using 2 planes and they have different tilt angles around y-axis. Figures 4.46 and 4.47 represent the reconstructed planes. Because of having different tilt angles, Figures 4.46 and 4.47 provide to see the 3-D object at different viewing angles.

Chapter 5

Comparison of the Two Simulators

In this chapter, the comparison between the results of the two simulators are given under several scenarios. The implemented scenarios include diffraction between tilted input and observation planes.

The pointwise simulator calculates the diffraction pattern of a sampled object. The diffraction pattern of the object is obtained by superposition of the diffraction pattern of the point light sources made up the object. The diffraction patterns of the point light sources are calculated by using the sampled kernel given in Eq. 3.9. There is a low-pass operation on the sampled kernel because it is calculated within a window. On the other hand, the plane wave spectrum simulator deals with the diffraction pattern of an object which is sampled and periodic. The obtained diffraction pattern is also sampled and periodic. The details of the periodicity is given in Appendix C. In this chapter, we show the deviations between the results obtained by using both simulators. We use the pointwise simulator as a reference because it is more close to the most of the physical cases compared to the plane wave simulator.

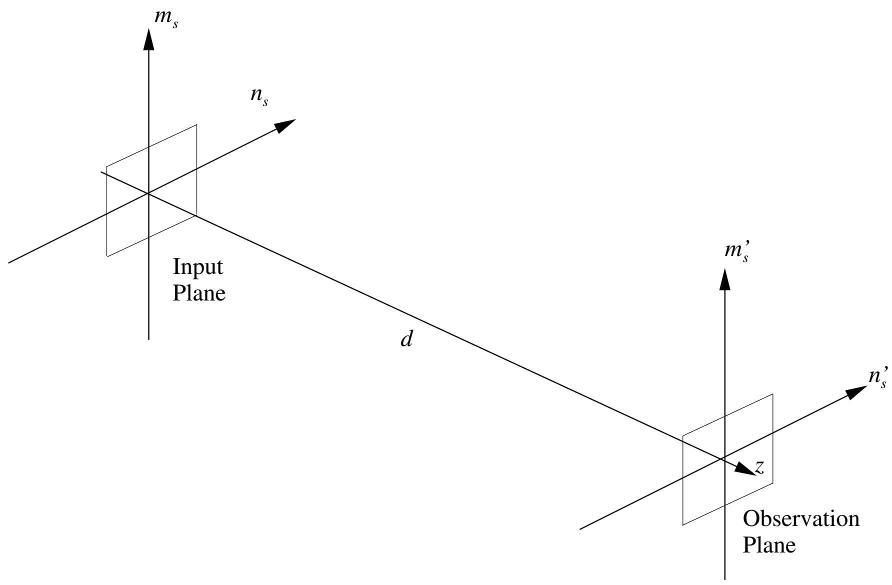

Figure 5.1: Illustration of the first scenario

The first scenario that is implemented, is illustrated in the Figure 5.1. The sampling period is chosen as 2λ and the distance between input and observation plane is 2048λ. The same input pattern is used in both simulators and the obtained real part of the diffraction patterns are given in Figures 5.3 and 5.4. It can be seen from Figures 5.3 and 5.4 that they look pretty much the same. Deviation between Figures 5.3 and 5.4 will be more evident if the size of the object is increased.

In the second scenario the same sampling period and the distance between the input and observation plane are used. The illustration of the scenario is given in Figure 4.2. As it is seen from the Figure 4.2, the observation plane is rotated around the y-axis. The tilt angle equals to $30°$. The real parts of the obtained diffraction patterns are given in Figure 5.5 and 5.6. There is a difference at the left side of Figure 5.6 compared to Figure 5.5. The Figure 5.7 provides the five times amplified difference between the Figures 5.5 and 5.6. At the left side of the Figure 5.7, the fringes are generated by the next replica of the diffraction pattern. The fringes in Figure 5.7 are generated by the further side of the next replica of the diffraction pattern.

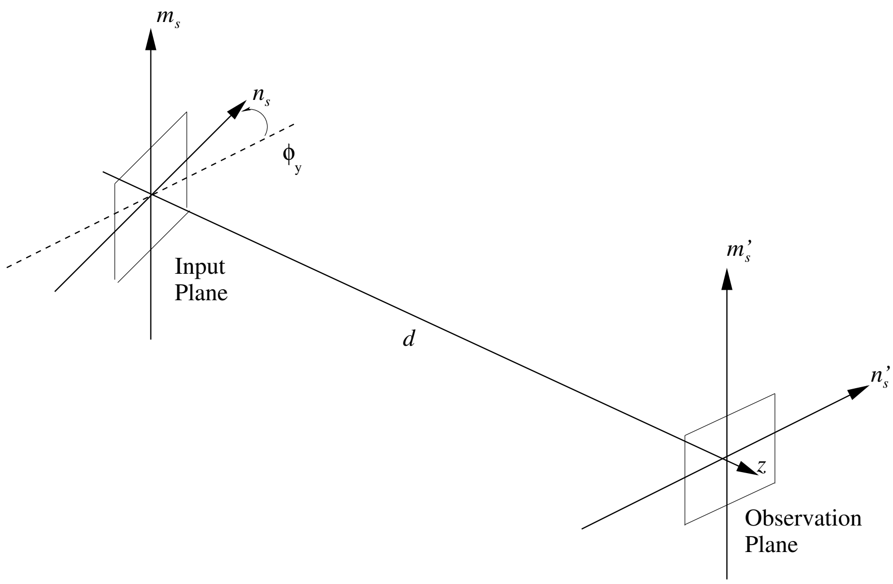

Figure 5.2: Illustration of the second scenario

The third scenario has the same parameters which are used in the second scenario except the tilt angle of the observation plane. In this scenario the tilt angle is 60° and the real part of the diffraction patterns can be seen in Figures 5.8 and 5.9. Five times amplified difference between Figures 5.8 and 5.9 can be seen in Figure 5.10. The reasons of the difference between two figures are the plane wave spectrum simulator gives one period of the periodic diffraction pattern and using bilinear interpolation causes numerical errors. Moreover, the plane wave spectrum simulator provides distorted diffraction patterns if the tilt angle is increased.

In the fourth scenario, the input plane is rotated around the y-axis and the illustration of the scenario is in Figure 5.2. The sampling period and the distance parameters are chosen as 2λ and 2048λ. The tilt angle is taken as 10°. The real part of the diffraction patterns are given in Figures 5.11 and 5.12. Again there is a difference between the two Figures. Five times amplified difference between the Figures 5.11 and 5.12 is given in Figure 5.13. As in the previous scenarios the distortion can be seen in the left side of the Figure 5.13. The effect of the next replica of the diffraction pattern causes the difference.

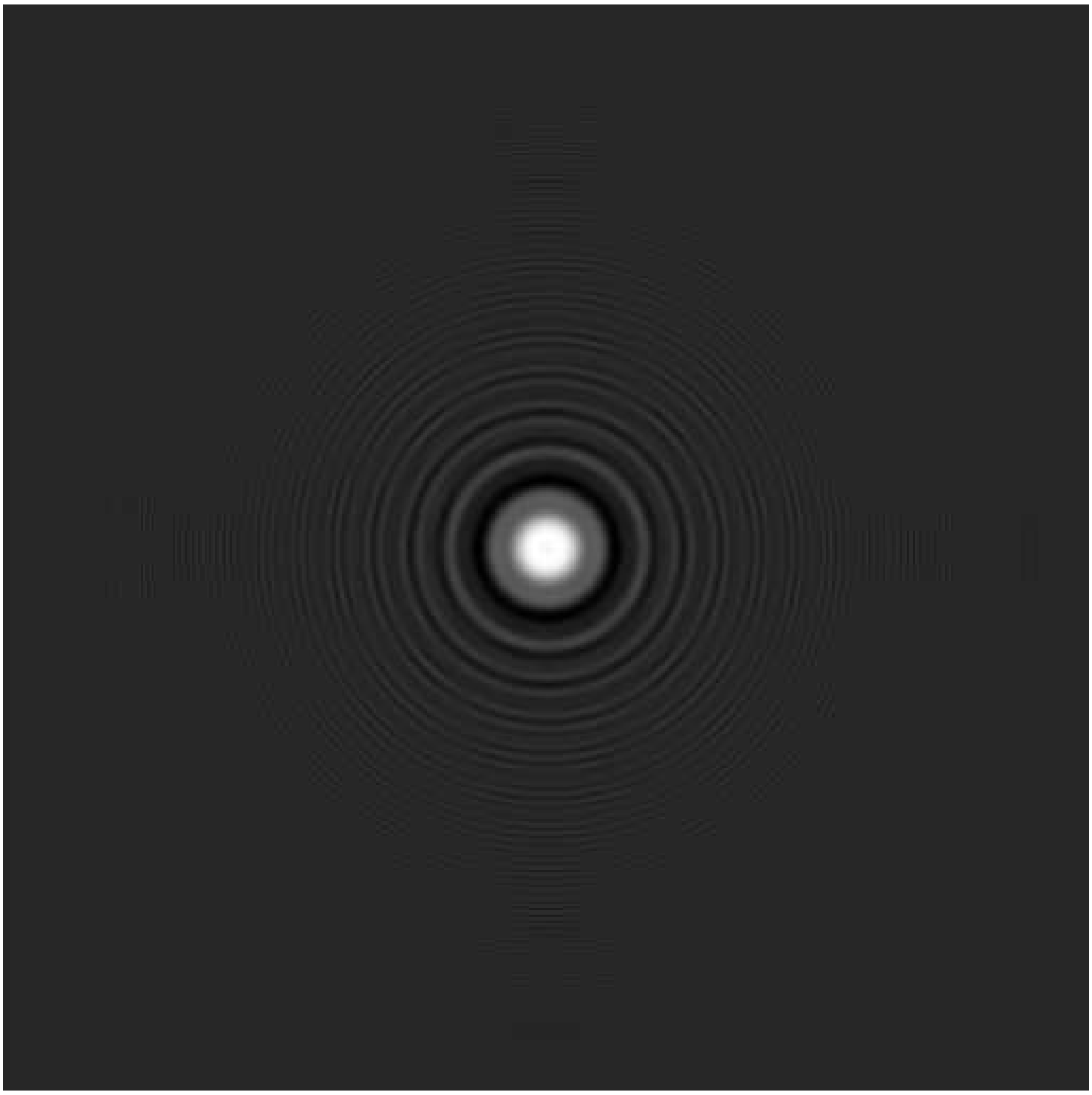

Figure 5.3: Real part of the diffraction pattern obtained by using pointwise simulator

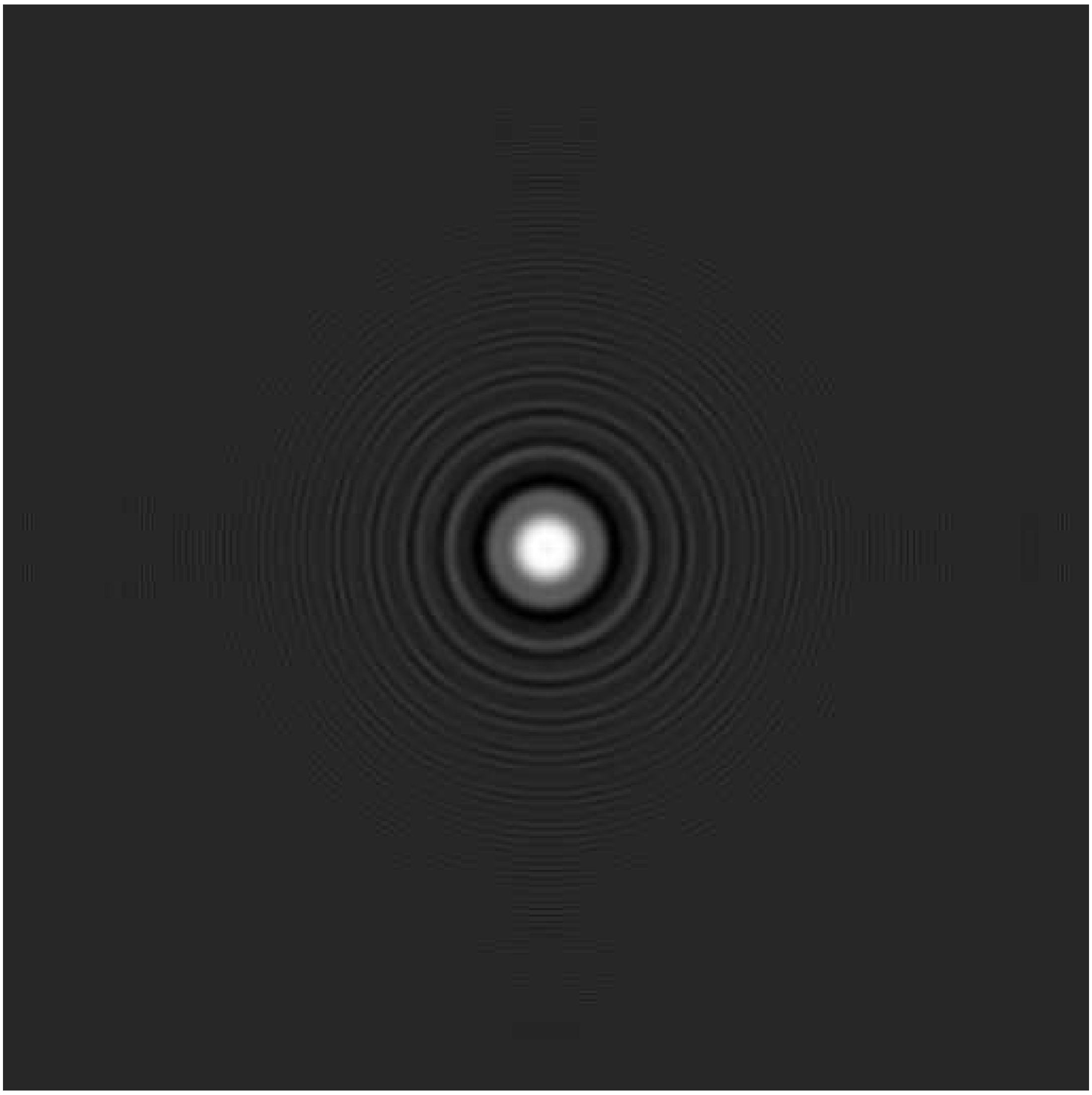

Figure 5.4: Real part of the diffraction pattern obtained by using plane wave spectrum simulator

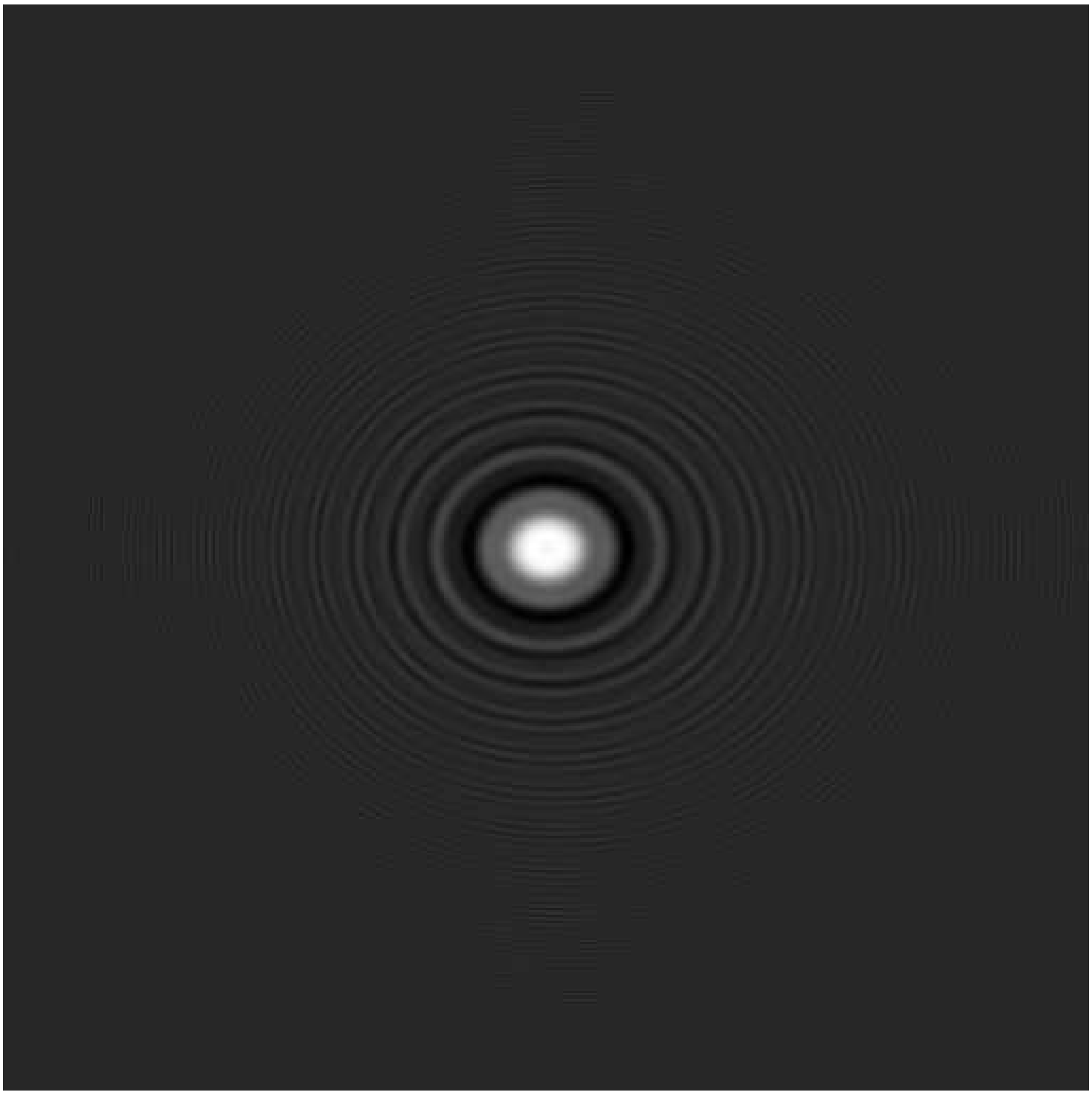

Figure 5.5: Real part of the diffraction pattern obtained by using pointwise simulator

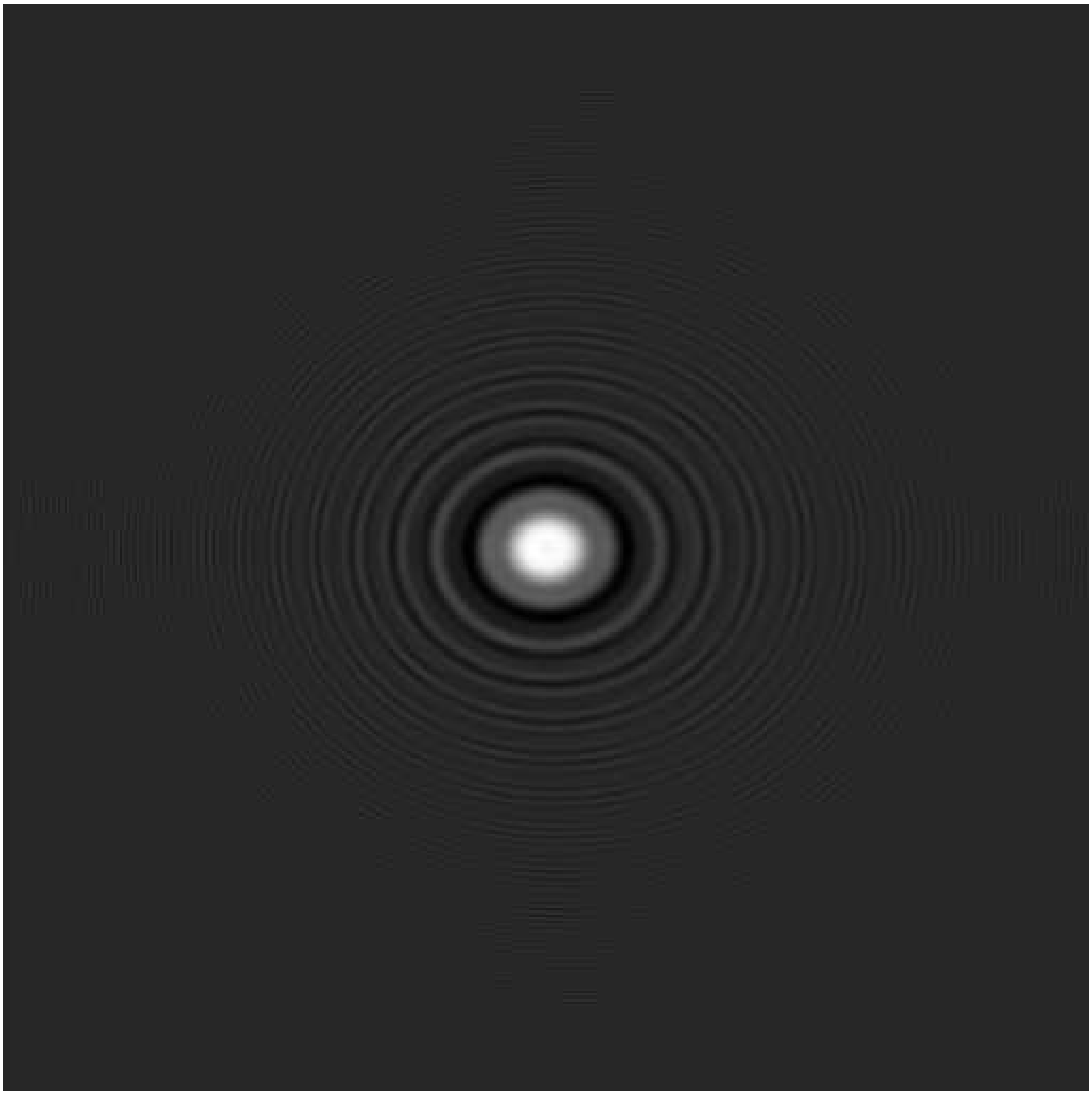

Figure 5.6: Real part of the diffraction pattern obtained by using plane wave spectrum simulator

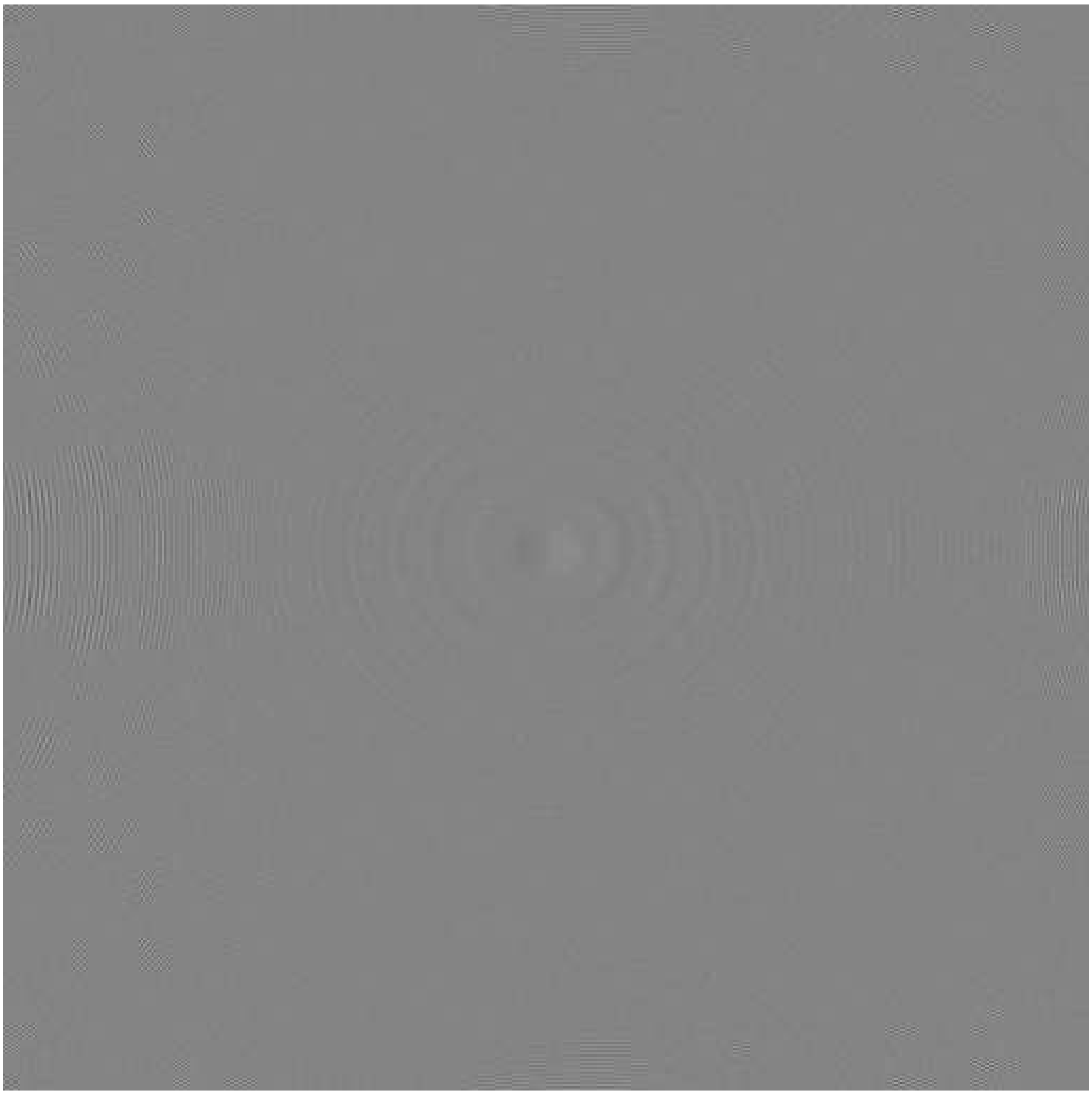

Figure 5.7: Difference between Figure 5.5 and Figure 5.6

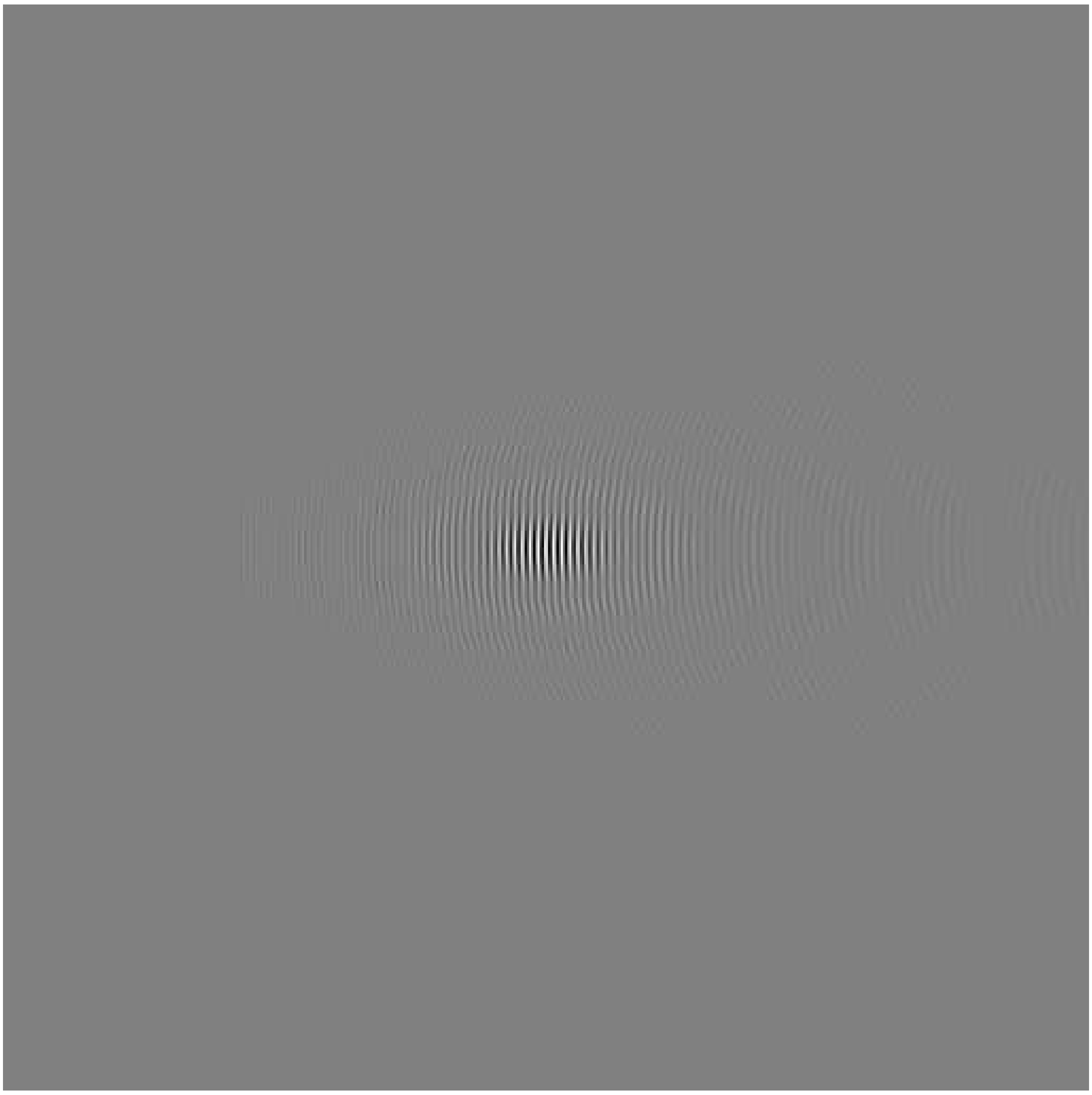

Figure 5.8: Real part of the diffraction pattern obtained by using pointwise simulator

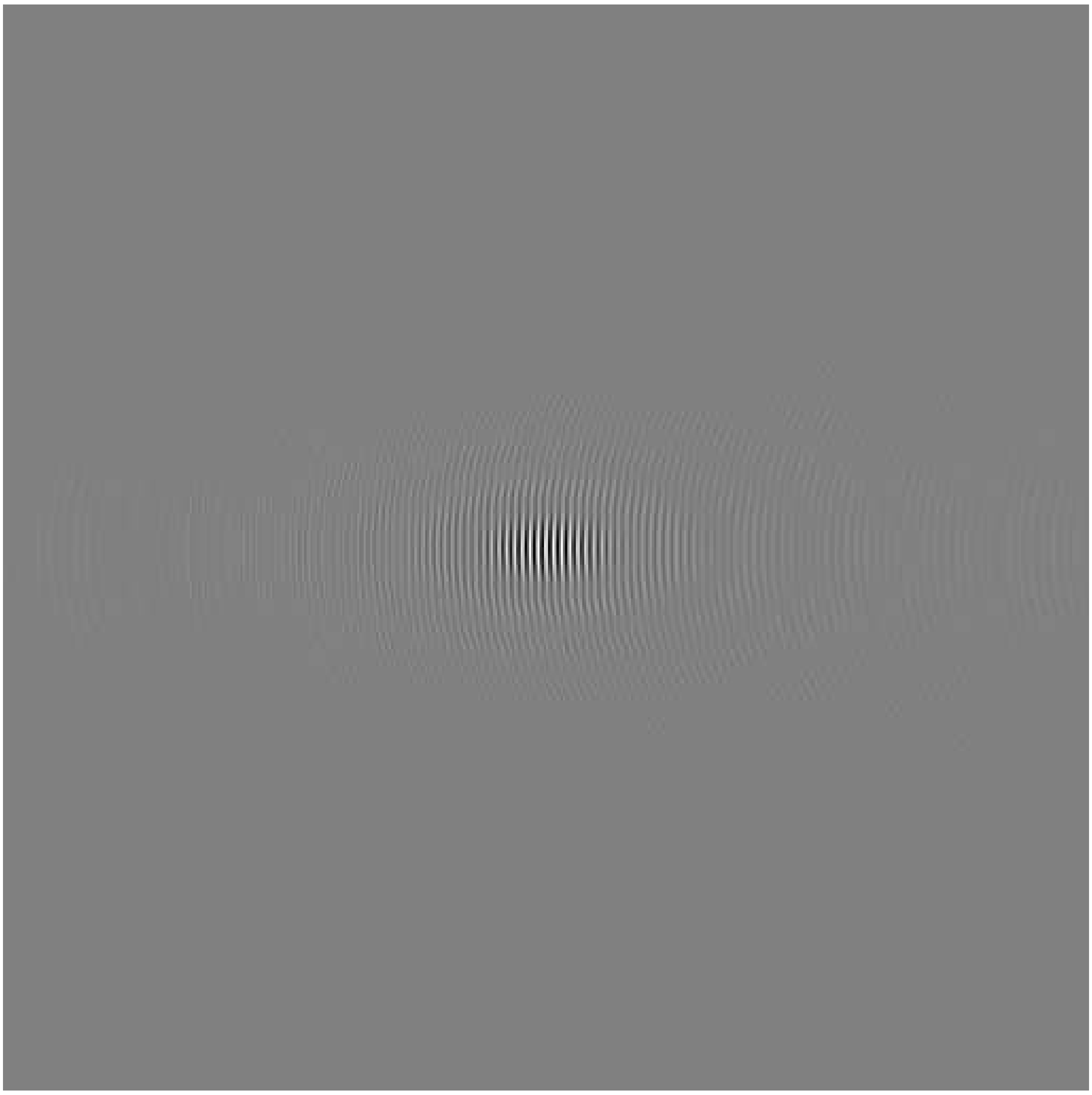

Figure 5.9: Real part of the diffraction pattern obtained by using plane wave spectrum simulator

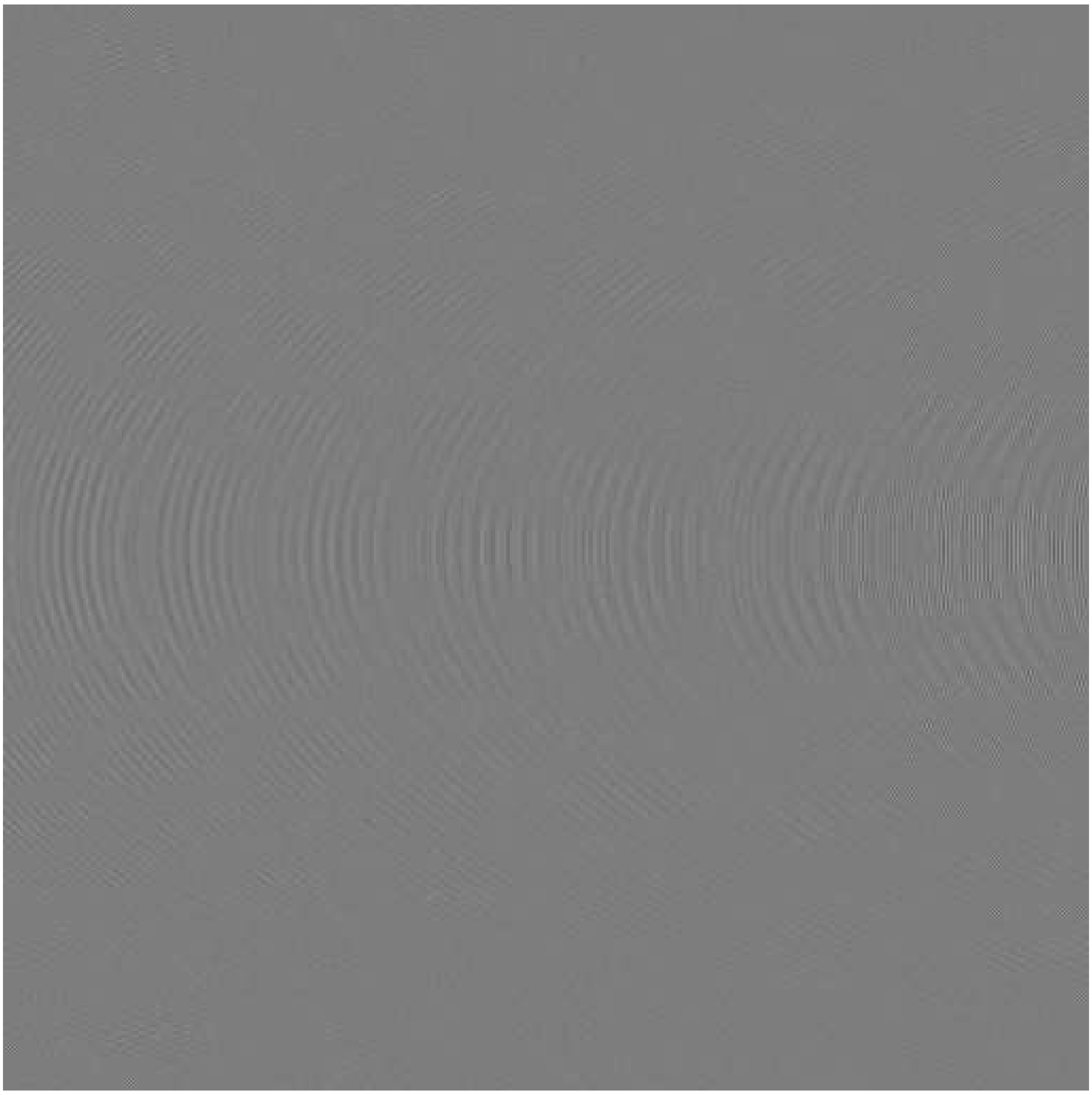

Figure 5.10: Difference between Figure 5.8 and Figure 5.9

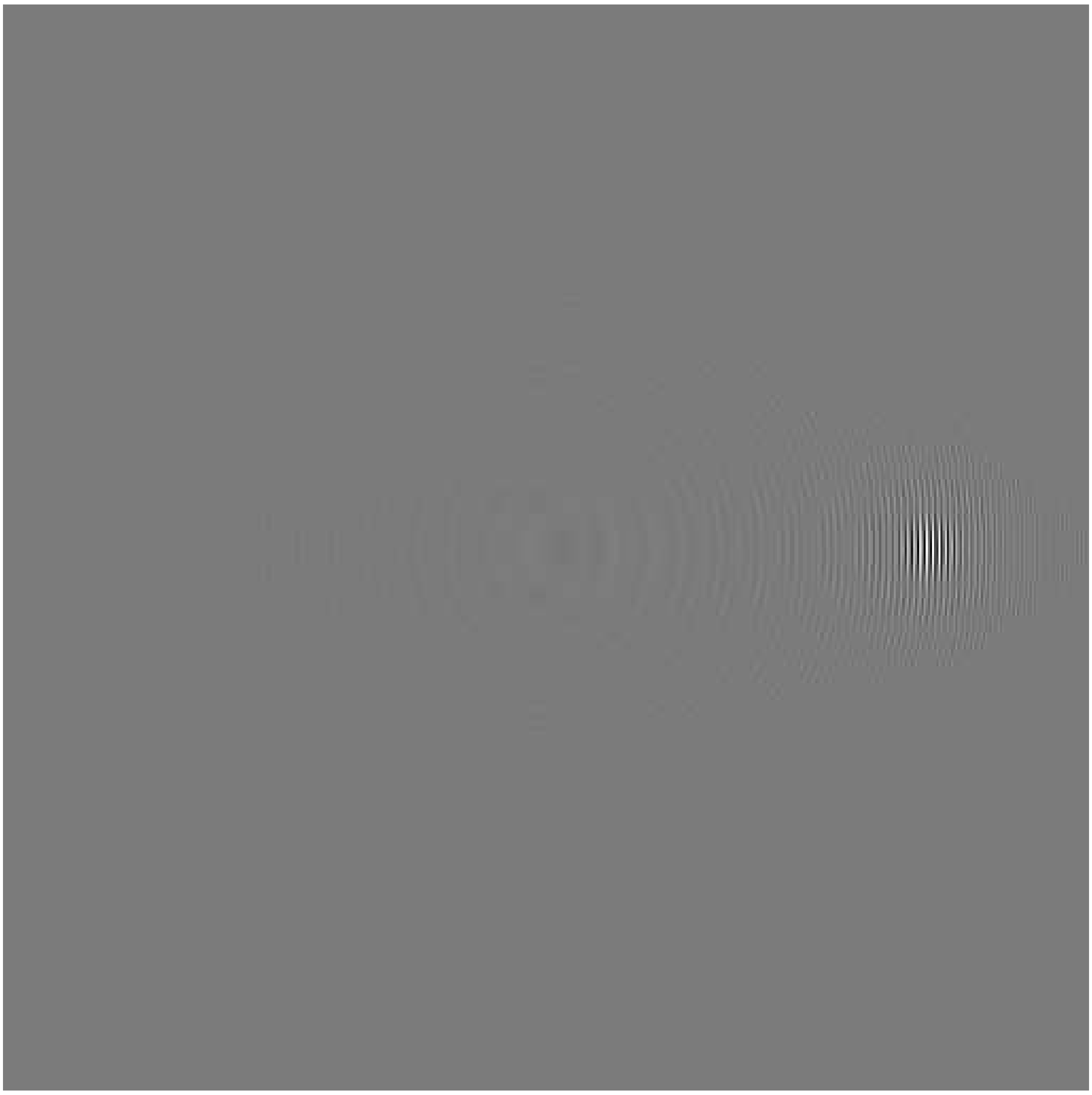

Figure 5.11: Real part of the diffraction pattern obtained by using pointwise simulator

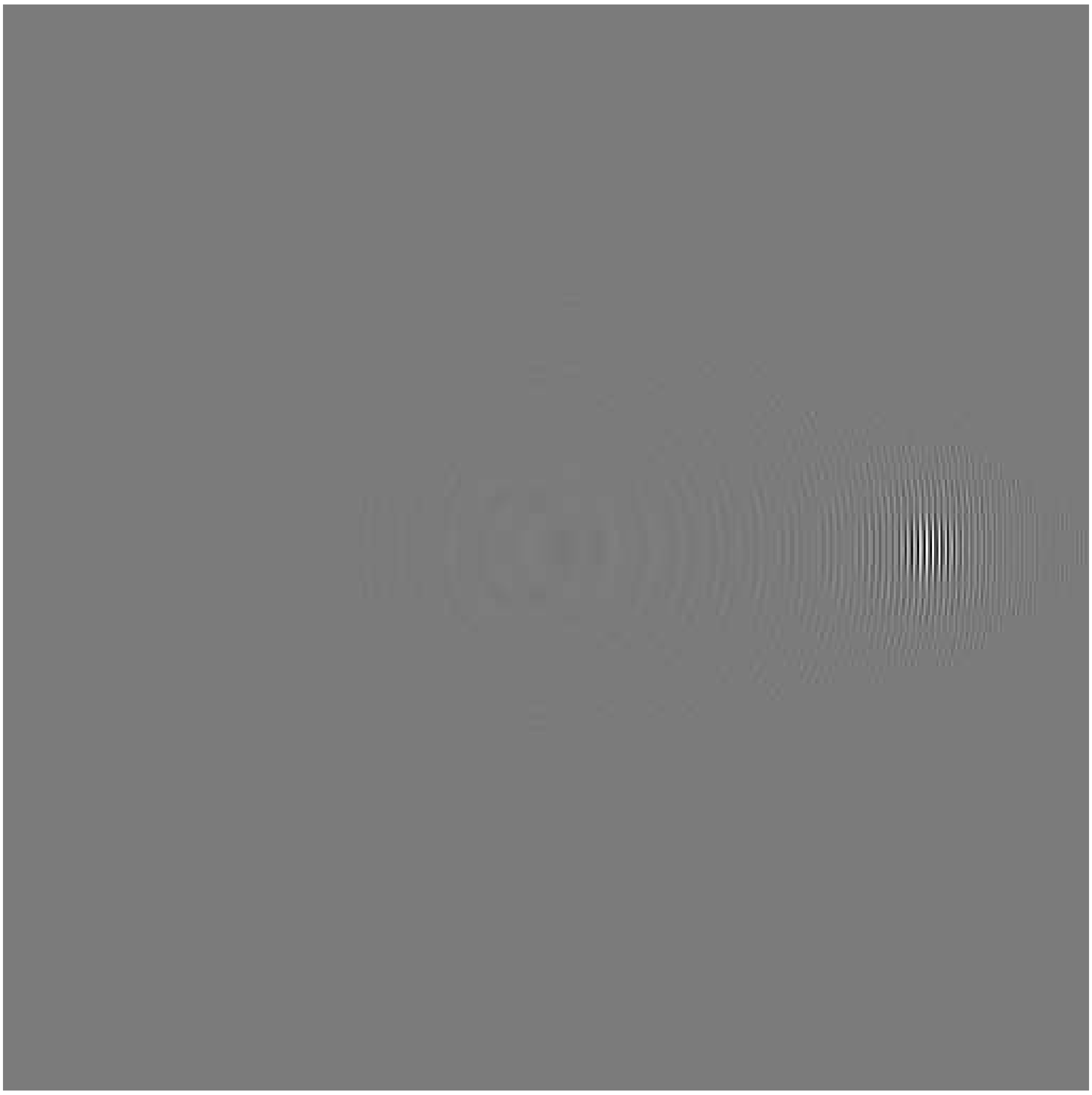

Figure 5.12: Real part of the diffraction pattern obtained by using plane wave spectrum simulator

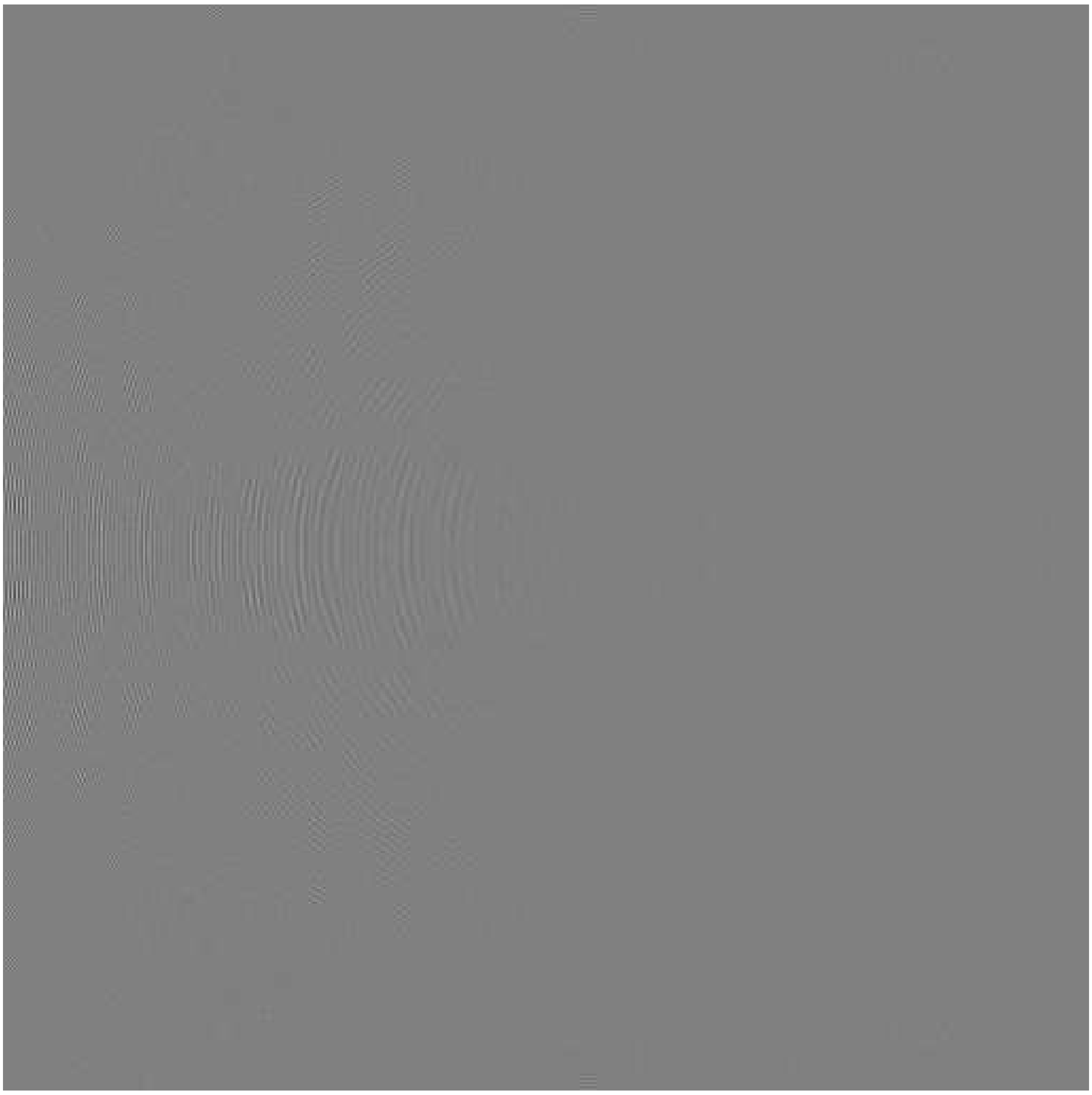

Figure 5.13: Difference between Figure 5.11 and Figure 5.12

Chapter 6

Conclusions

In this dissertation, we presented a technique that can provide fast computation of scalar optical diffraction between tilted input and observation plane. It is known that calculation of diffraction due to a three-dimensional object is time consuming when the diffraction pattern is obtained by superposition of the diffraction pattern of the point light sources. Therefore, we presented the plane wave spectrum technique that provides fast computation of the diffraction pattern due to an object. Also, the results of the presented method are compared with the results of the pointwise simulator. When certain restrictions are imposed on the plane wave spectrum simulator parameters, it is seen that both results are similar. The results are not exactly the same because the plane wave spectrum simulator deals with only periodic input and output patterns. However, the pointwise simulator can deal with non-periodic patterns.

The pointwise simulator based on the Rayleigh-Sommerfeld diffraction integral. The diffraction pattern of the object is obtained from summing up the diffraction field due to point sources which form the object. It is a time consuming method and its algorithmic complexity is $O(N^4)$. Because, the parameters of the discrete kernel can change for each point source. Therefore, the discrete kernel is computed for each point source. Each point source interacts with the light distribution of other point sources. However, in reality diffraction field on an observation plane is obtained from an input field. Therefore the starting point is not the light source but the generated field by the light source. For instance, in the second scenario in Chapter 3 there are two light sources which are located at different z-axis positions. The interaction can be seen from the reconstructed objects which are given in Figures 3.14 and 3.15. Moreover, pointwise simulator is easy to model and also it has less restrictions according to plane wave simulator such as providing non-periodic diffraction pattern and having non-periodic kernel. Therefore, it can be taken as a reference for the plane wave spectrum simulator.

The plane wave spectrum simulator provides the scalar optical diffraction between tilted planes, but in some scenarios the obtained results deviate from the results that are obtained by using pointwise simulator. These deviations caused by having periodic input and output patterns. Moreover, having bilinear interpolation brings some amount of computational errors. In the first scenario in Chapter 5 the results obtained by using pointwise and plane wave spectrum simulators are very similar. If the size of the object is increased in the first scenario in Chapter 5, the deviation will be more evident. In the second scenario the observation plane is rotated around y-axis and the tilt angle is taken as $30°$. It can be seen from Figures 5.4 and 5.5 that there are some deviation at the left side of the Figures. The deviation in the Figure 5.5 is caused by the next replica of the diffraction pattern. Moreover, the effect of the deviation increases when the tilt angle is increased. The third scenario in the chapter four, the tilt angle is assigned to $45°$. The deviation caused by the replica can be easily seen in Figure 4.26. In the third scenario in Chapter 5, the tilt angle is $60°$. The deviation for $60°$ tilt angle is more than the deviation for $45°$, $30°$ and $0°$ tilt angles. The fourth scenario in Chapter 5 provides the diffraction pattern when the input plane is tilted around the y-axis. The deviations caused by having periodic input and diffraction patterns and bilinear interpolation.

The performance of plane wave spectrum simulator is tested in two categories by the results of the pointwise simulator. First category is the deviation of the results. The observation plane should not have more than $60°$ tilt angle when the plane wave spectrum simulator is used. Because, larger tilt angle causes deviations not only at the edges of the diffraction pattern but also in the center of the diffraction pattern. The effect of the deviation can be seen in the Figure 5.9. Moreover, the tilt angle of the input plane should not be assigned more than $10°$ because the periodic input and observation planes cause to implement undesired scenario. The detailed information about the periodicity is given in Appendix C. Second one is the calculation time. The algorithmic complexity of the plane wave spectrum simulator is about $O(N^2 \log^2(N))$. The time consuming processes in the plane wave spectrum simulator are taking DFT and IDFT. Therefore larger N provides time saving according to the pointwise simulator.

In this thesis, the plane wave spectrum simulator and its mathematical model is presented. The simulator is useful to calculate the diffraction pattern of an object. Also, the simulator provides fast computation of the diffraction pattern of the object. Nevertheless, the computation time can be shorter by optimization of the simulator and by using parallel processing.

Appendix A

Object Generation

In three-dimensional space, an object can be modelled by using planar patches (faces). These faces are defined by vertices. An example is given in Figure A.1 In this work each patch contains three vertices. Moreover, Lambertian cosine law [19] is applied to each face, so we can obtain more realistic objects. Rendering operation of a face is obtained from three vertices. Let P_1, P_2 and P_3 the three vertices of a patch. Then $\vec{P_1P_2}$ and $\vec{P_1P_3}$ gives the vectors $\vec{v_1} = (v_{11}, v_{12}, v_{13})$ and $\vec{v_2} = (v_{21}, v_{22}, v_{23})$. An illustration is shown in Figure A.2. Points that construct the face can be found as

$$
\begin{aligned}
x_p &= x_{P_1} + v_{11}ln + v_{21}lm \\
y_p &= y_{P_1} + v_{12}ln + v_{22}lm \\
z_p &= z_{P_1} + v_{13}ln + v_{23}lm
\end{aligned} \tag{A.1}
$$

where l is the sampling period, m and n are integer numbers and also they are in the range of $[0, N)$. Moreover, the variables m and n are related to each other as $m = N - n$. As a result of this operation triangular patch is rendered completely.

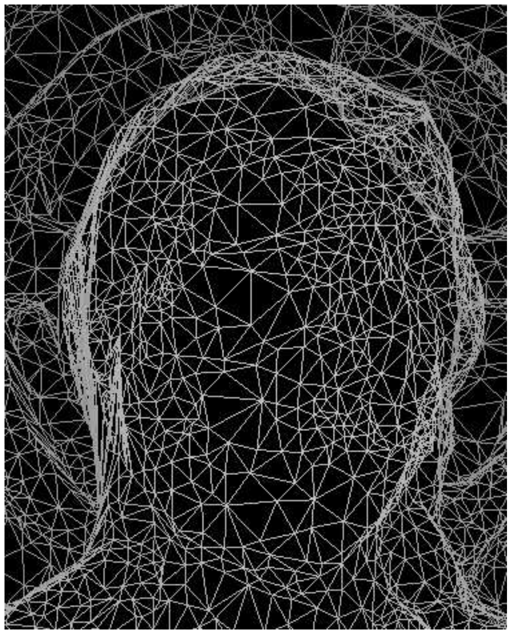

Figure A.1: An object generated by vertices.

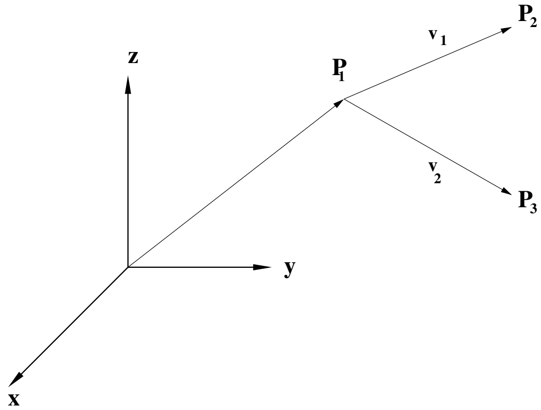

Figure A.2: A patch formed by vertices.

Appendix B

Finding the Jacobian

The Jacobian is calculated as

$$J = \begin{vmatrix} \frac{\partial k_x}{\partial k_{x'}} & \frac{\partial k_x}{\partial k_{y'}} \\ \frac{\partial k_y}{\partial k_{x'}} & \frac{\partial k_y}{\partial k_{y'}} \end{vmatrix} \tag{B.1}$$

$$\frac{\partial k_x}{\partial k'_x} = r_{11} - r_{31}\frac{k'_x}{k'_z} \tag{B.2}$$

$$\frac{\partial k_x}{\partial k'_y} = r_{21} - r_{31}\frac{k'_y}{k'_z} \tag{B.3}$$

$$\frac{\partial k_y}{\partial k'_x} = r_{12} - r_{32}\frac{k'_x}{k'_z} \tag{B.4}$$

$$\frac{\partial k_y}{\partial k'_y} = r_{22} - r_{32}\frac{k'_y}{k'_z} \tag{B.5}$$

where the variables r_{11}, r_{12}, r_{21}, r_{22}, r_{31} and r_{32} are obtained from the rotation matrix $\mathbf{R}$ which is defined in Eq 4.5. As the matrix $\mathbf{R}$ is a rotation matrix, the relations are given below hold:

$$r_{11}r_{22} - r_{21}r_{12} = r_{33}, \quad r_{21}r_{32} - r_{31}r_{22} = r_{13}, \quad r_{12}r_{31} - r_{11}r_{32} = r_{23} \tag{B.6}$$

As a final result, substitution of the above terms in Eq B.1 provides

$$J = (r_{11} - r_{31}\frac{k'_x}{k'_z})(r_{22} - r_{32}\frac{k'_y}{k'_z}) - (r_{21} - r_{31}\frac{k'_y}{k'_z})(r_{12} - r_{32}\frac{k'_x}{k'_z}) \tag{B.7}$$

$$J = r_{11}r_{22} - r_{11}r_{32}\frac{k'_y}{k'_z} - r_{31}r_{22}\frac{k'_x}{k'_z} + r_{31}r_{32}\frac{k'_x k'_y}{{k'_z}^2} - \left\{ r_{21}r_{12} - r_{21}r_{32}\frac{k'_x}{k'_z} - r_{12}r_{31}\frac{k'_y}{k'_z} + r_{31}r_{32}\frac{k'_x k'_y}{{k'_z}^2} \right\} \tag{B.8}$$

$$J = (r_{11}r_{22} - r_{21}r_{12}) + (r_{21}r_{32} - r_{31}r_{22})\frac{k'_x}{k'_z} + (r_{12}r_{31} - r_{11}r_{32})\frac{k'_y}{k'_z} \tag{B.9}$$

$$J = \frac{r_{13}k'_x + r_{23}k'_y + r_{33}k'_z}{k'_z} \tag{B.10}$$

$$J = \frac{k_z}{k'_z} \tag{B.11}$$

Appendix C

Periodicity of Input and Output Patterns

The scalar optical diffraction formulation for monochromatic coherent wave is given in Eq. 4.10. However, the formulation in Eq 4.10 is in continuous domain. All the computations will be done in a digital environment such as a computer. Therefore, the input and the diffraction patterns have to be sampled and DFT and IDFT operations are used instead of FT and IFT operations. The input pattern is represented as

$$f(n_s, m_s) = \sum_{n_f, m_f = 0}^{N-1} A(n_f, m_f) e^{j \frac{2\pi}{N}(n_f n_s + m_f m_s)} \tag{C.1}$$

As it is seen from Eq. C.1, the input pattern $f(n_s, m_s)$ and its Fourier transform $A(n_f, m_f)$ are periodic and they have N^2 different elements. The signal $A(n_f, m_f)$ provides the coefficients of the plane waves that construct the input pattern. These coefficients are used in the plane wave spectrum simulator. Therefore the plane wave spectrum simulator calculates the diffraction pattern on the observation plane that is generated by an input pattern sampled by X and periodic with NX. Rectangular sampling is used to obtain the signal $f(n_s, m_s)$.

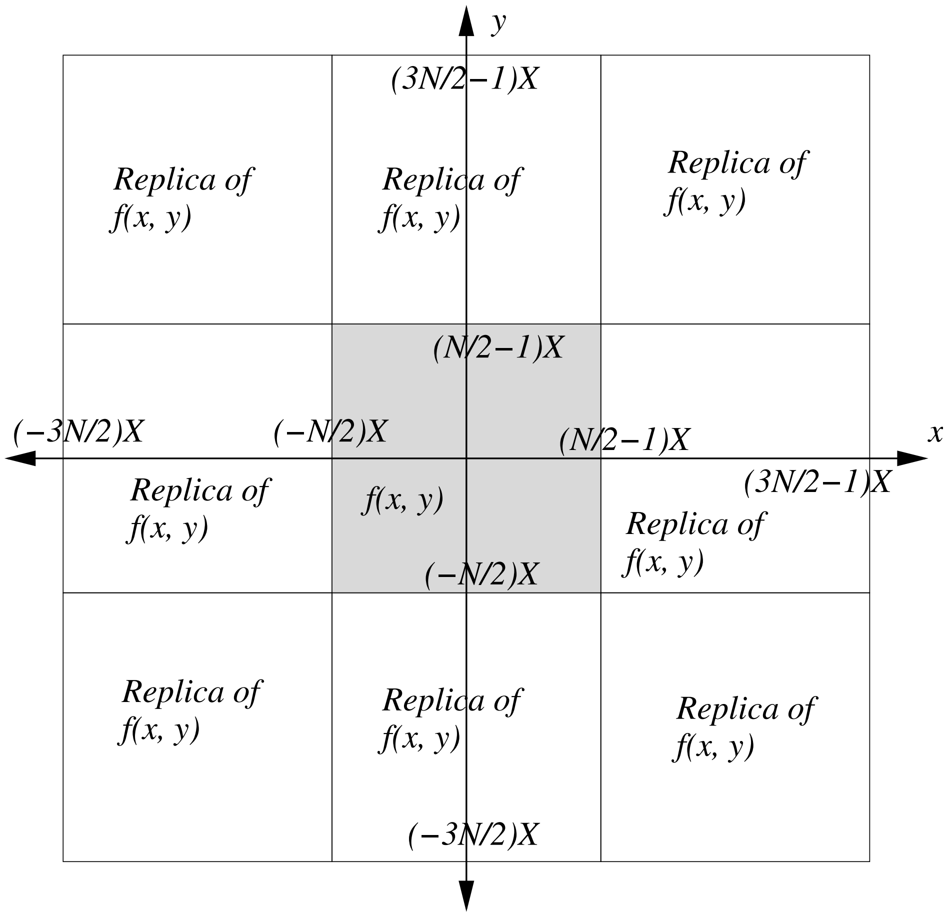

Figure C.1: An illustration of the periodicity of an input pattern $f(x, y)$

.

There is an illustration in Figure C.1 that will be useful to describe the periodicity of the signal $f(x, y)$. Furthermore, the diffraction pattern on the observation plane is also sampled and we use the same sampling period which is used in sampling the input pattern. The relation between input and observation plane is defined as

$$[\ n'_s \quad m'_s \quad l'_s\ ]^T = \mathbf{R}[\ n_s \quad m_s \quad 0\ ]^T + [\ 0 \quad 0 \quad p\ ]^T\ . \tag{C.2}$$

The diffraction pattern on the observation plane is obtained by summing up the incidence plane waves and it is represented as

$$|\ g(n'_s, m'_s)| = |\sum_{n'_f, m'_f = 0}^{N-1} \tilde{A}_{1,D}(n'_f, m'_f) e^{-j\frac{2\pi}{N}(n'_f n'_s + m'_f m'_s)} e^{j\frac{2\pi}{N}\vec{k}_D^T \vec{p}}| \tag{C.3}$$

where the definition of the vector $\vec{k}_D^T$ is given in Chapter 4. The variable $g(n'_s, m'_s)$ is periodic by N. We can show that by substituting $n'_s + N$ instead of n'_s and

$m'_s + N$ instead of m'_s in Eq. C.3 and the obtained result can be represented as

$$\begin{aligned} |\ g(n'_s + N, m'_s + N)| &= |\sum_{n'_f, m'_f = 0}^{N-1} \tilde{A}_{1,D}(n'_f, m'_f) e^{-j\frac{2\pi}{N}(n'_f(n'_s+N)+m'_f(m'_s+N))} e^{j\frac{2\pi}{N}\vec{k}_D^T\vec{p}}| \\ &= |\sum_{n'_f, m'_f = 0}^{N-1} \tilde{A}_{1,D}(n'_f, m'_f) e^{-j\frac{2\pi}{N}(n'_f n'_s + m'_f m'_s)} e^{j\frac{2\pi}{N}\vec{k}_D^T\vec{p}}| \quad . \end{aligned} \tag{C.4}$$

It is shown that the discrete array $|g(n'_s, m'_s)|$ is periodic by N and it represents the samples of the diffraction pattern in continuous domain. The interval between two consecutive samples equals to X. Therefore, in physical environment the diffraction pattern is periodic by NX. In Chapter 4, there is an illustration that gives physical locations of the periodic input and diffraction patterns.

Appendix D

How to Use The Simulator

Three simulation programs are written. All the programs are generated by using the programming language C. First one is the pointwise simulator which is used to obtain the off-axis hologram of an object. Second one is the plane wave spectrum simulator and also we use it to obtain the off-axis hologram of the object. Third one is again a pointwise simulator but it is used to reconstruct the object from the off-axis hologram of it. All the simulators expects proper inputs. For instance, all the files written in binary file format. In other words, all the data converted to binary then written on a file. The program statements used to generate a binary file is given as

$filePointer = fopen("fileName","wb");$

$fwrite(data, sizeof(double)*(N*N), 1, filePointer);$

The variable N is the size of the filter we use in the simulations. The variable $data$ is written on the file which is called $fileName$. The obtained results of the simulators can be displayed by using image files. These three simulators uses raw image format to display the results. Raw image format contains only the data itself so there is no compression in the data. Scan directions of the raw image are left to right and top to bottom. Also, there is no header in the file. Moreover, each pixel of an image is represented by 8 bits.

Run $pointwiseHolo.exe$ to find the off-axis hologram of an object.

$> pointwiseHolo.exe$

Enter input file name (max 20 char) = **objectXY**

The file **objectXY** is in binary file format. It provides the size and the illumination of the object.

Enter the sampling period in terms of lambda (X/lambda) = **2**

Enter variable p = **1024**

The variable p determines the distance between input and observation plane.

Enter **i** to tilt input plane, **o** to tilt observation plane = **o**

Enter phi_x (in degrees) = **20**

The variable phi_x is the tilt angle around x-axis.

Enter phi_y (in degrees) = **15**

The variable phi_y is the tilt angle around y-axis.

Enter R_0 = **200**

The variable R_0 is the magnitude of the reference beam.

Enter Γ = **0.8**

The variable Γ is related to the incidence angle of the reference beam.

Enter output file name (max 20 char) = **pointwiseOutput**

The file **pointwiseOutput** is in binary file format. It contains the size and the off-axis hologram of the object.

Run $offAxisHologram.exe$ to get the off-axis hologram of the object by using plane wave spectrum model.

$> offAxisHologram.exe$

Enter input file name (max 20 char) = **objectXY**

Enter **i** to tilt input plane, **o** to tilt observation plane = **o**

Enter phi_x (in degrees) = **10**

Enter phi_y (in degrees) = **25**

Enter beta = **1024**

The variable beta determines the sampling period.

Enter alpha = **1024**

The variable alpha provides the distance between input and observation plane.

Enter R_0 = **200**

Enter Γ = **0.8**

Enter output file name (max 20 char) = **output1**

Run $reconHolo.exe$ to find the magnitude of the reconstructed object.

$> reconHolo.exe$

Enter input file name (max 20 char) = **output2**

Enter the sampling period in terms of lambda (X/lambda) = **2**

Enter variable p = **1024**

Enter **i** to tilt input plane, **o** to tilt observation plane = **i**

Enter phi_x (in degrees) = **40**

Enter phi_y (in degrees) = **30**

Enter R_0 = **200**

Enter Γ = **0.8**

Enter output file name (max 20 char) = **reconObject**

Bibliography

[1] T. Okoshi, "Three-Dimensional Imaging Techniques", New York Acedemic Press, 1976.

[2] M. Lucente, "Optimization of Hologram Computation for Real-Time Display", in SPIE Proceedings 1667 Practical Holography (SPIE, Bellingham, WA, Feb 1992), S.A. Benton, pp 32-43.

[3] M. McKenna and D. Zeltzer, "Three-Dimensional visual display systems for virtual environments", Presence: Teleoperators and Virtual Environments. vol. 1, pp. 421-458, 1992.

[4] Mark Lucente and Tinsley A. Galyean, " Rendering interactive holographic images", Proc. of SIGGRAPH 95 (LA, CA, Aug. 6-11, 1995). In Computer Graphics Proceedings, ACM SIGGRAPH, pp. 387-394.

[5] R. S. Pappu, "Minimum Information Holograms", M.S. Thesis, Media Arts and Sciences School of Architecture and Planning MIT, July 1995.

[6] O. Nishikawa, T. Okada, H. Yoshikawa, K. Sato, T. Honda, "High-speed holographic-stereogram calculation method using 2D FFT", SPIE Proceedings of Diffractive and Holographic Device Technologies and Applications IV, Vol. 3010, paper 10, Feb.1997

[7] Yoshihiro Kajiki, Hiroshi Yoshikawa and Toshio Honda, "Auto-Stereoscopic 3D Video Display using Multiple Light-Beams with Scanning", IEEE Transactions on Circuits and Systems for Video Technology, Vol.10, No.2, pp.254-260, March 2000.

[8] M. Lucente, "Diffraction-Specific Fringe Computation for Electro-Holography", Doctoral Thesis Dissertation, MIT Dept. of Electrical Engineering and Computer Science, Sept. 1994.

[9] G. Bozdaği, "Simulation of A Holographic 3-D Television Display", M.S. Thesis, Bilkent University Dept. of Electrical and Electronics Engineering, Dec. 1990.

[10] H. C. McKay, "Three-Dimensional Photography, principles of stereoscopy", American Book Stratford Press, 1953.

[11] Dennis Gabor, "Holography, 1948-1971", Proc. IEEE, vol.60, pp.655-668, June 1972

[12] K. Iizuka, "Engineering Optics", Springer-Verlag, Berlin, 1987.

[13] G. C. Sherman, "Application of the Convolution Theorem to Rayleigh's Integral Formulas", J. Opt. Soc. Am., 1967.

[14] L. Onural and P.D. Scott, "Digital Decoding of In-Line Holograms", Optical Engineering, vol.26, no.11, pp.1124-1132, Nov. 1987.

[15] J.E. Kasper and S.A. Feller, "The Complete Book of Holograms", John Wiley & Sons Inc., 1987.

[16] R.J. Collier, C.B. Burckhardt and L.H.Lin, "Optical Holography", Academic Press, Inc. New York, 1971.

[17] Y.I. Ostrovsky, "Holography and Its applications", Academic Press, Inc., 1977

[18] G. Saxsby, "Practical Holography", Printice Hall, 1988.

[19] Hearn and Baker, "Computer Graphics", 2nd Edition (in C), Prentice Hall, 1996.

[20] Mark Lucente, "Interactive three-dimensional holographic displays: seeing the future in depth", Computer Graphics (A publication of ACM SIGGRAPH) Volume 31, Number 2, May 1997.

[21] J. Goodman, "Introduction to Fourier optics", New York, McGraw-Hill 1996

[22] B.E.A. Saleh and M.C. Teich, "Fundamentals of Photonics", John Wiley and Sons Inc. 1991.

[23] L. Onural, "Sampling of the diffraction field", Appl. Opt., vol. 39 no. 32, Nov 2000.

[24] S. Ganci, "Fourier diffraction through a tilted slits", Eur. J. Phys. 2, 158-160, 1981.

[25] K. Patorski, "Fraunhofer diffraction patterns of tilted planar objects", Opt. Acta 30, 673-679, 1983.

[26] H.J. Rabal, N. Bolognini and E. E. Sicre, "Diffraction by a tilted aperture, coherent and partially coherent cases", Opt. Acta 32, 1309-1311, 1985.

[27] D. Leseberg and C. Frére, "Computer generated holograms of 3-D objects composed of tilted planar segments", Appl. Opt. 27, 3020-3024, 1988.

[28] C. Frére and D. Leseberg, "Large objects reconstructed from computer generated holograms", Appl. Opt. 28, 2422-2425, 1989.

[29] T. Tommasi and B. Bianco, "Frequency analysis of light diffraction between rotated planes", Opt. Lett. 17, 556-558, 1992.

[30] T. Tommasi and B. Bianco, "Computer-generated holograms of tilted planes by a spatial frequency approach", J. Opt. Soc. Am. A 10, 299-305, 1993.

[31] B. Bianco and T. Tommasi, "Space-variant optical interconnection through the use of computer-generated holograms", Appl. Opt. 34, 7573-7580, 1995.

[32] N. Delen and B. Hooker, "Free-space beam propagation between arbitrarily oriented planes based on full diffraction theory: a fast Fourier transform approach", J. Opt. Soc. Am. A, vol 15, no 4, April 1998.

[33] K. Matsushima, H. Schimmel and F. Wyrowski, "Fast calculation method for optical diffraction on tilted planes by use of the angular spectrum of plane waves", J. Opt. Soc. Am. A, vol. 20, no 9, September 2003.

[34] L. Onural, "Some mathematical properties of the uniformly sampled quadratic phase function and associated issues in digital Fresnel diffraction simulations", to appear in Optical Engineering, Nov. 2004